12-2022

Experimental Tests and Numerical Study of Trajectories of Different Types of Dropped Objects

Yi Li
University of New Orleans, yli25@uno.edu

Experimental Tests and Numerical Study of Trajectories of Different Types of Dropped Objects

A Dissertation

Submitted to the Graduate Faculty of the
University of New Orleans
in partial fulfillment of the
requirements for the degree of

Doctor of Philosophy
in
Applied Science and Engineering

by

Yi Li

B.S. Qingdao Technological University, 2015
M.S. University of New Orleans, 2020

December, 2022

Two things fill the mind with ever new and increasing admiration and awe, the more often and steadily we reflect upon them: the starry heavens above me and the moral law within me.

Acknowledgments

I would like to express my sincerest appreciation to a number of people without whom this dissertation would not have been possible. Without their guidance and persistent help this dissertation would not have been possible.

To my advisor, Dr. Vincent Xiaochuan Yu, and Co-advisor, Dr. Damon Smith, who are always a source of knowledge and inspiration for me.

To my professors, Dr. Brandon Taravella, Dr. Lothar Birk, Dr. Linxiong Li and Dr. Nikolas Xiros, who also provide me with invaluable and insightful thinking and guidance during my research.

To my friends and colleagues, Haozhan Meng and Hanqi Yu, without whom, my life during my doctorate study at UNO would become much harder.

To my beloved parents, who continuously support and encourage me throughout my study and research.

Contents

List of Tables

List of Figures

List of Abbreviation and Symbols

Nomenclature

OXZ	Global coordinate system
oxz	Local coordinate system fixed on the cylinder
X	X-axis points to the right along the still water surface
Z	Z-axis perpendicular to the still water surface and point upward
U_1	Velocity component for surge
U_3	Velocity component for heave
Ω_2	Velocity component for pitch
β	The instantaneous rotational angle between the *x*-axis and the *X*- axis
m	Mass of the cylinder
M_{55}	Moment of inertia along the pitch direction
m_{33}	Added mass along heave direction from the strip theory
m_{55}	Added mass along pitch direction from the strip theory
m_t	2D added mass along heave direction at the trailing edge
x_t	Longitudinal position of effective trailing edge
g	Acceleration of the gravity
ρ	Density of the water
r	Volume of the cylinder
D	Diameter of the cylinder
v	Kinematic viscosity of the water
L	Length of the cylinder
C_{dx}	Drag coefficient along the x-direction
C_{dz}	Drag coefficient along the z-direction
F_{dx}	Drag force along the direction of surge
F_{dz}	Force component along the direction of heave
M_{dy}	Force component along the direction of pitch
x_k	State at time index k
k	Time index

$\dot{x}_k = f_k(x_k)$	The state space model
$x_{k+1}=f_k^d(x_k)$	The discretized state space model
$x(\bar{x}, P_x)$	Random variable x with mean $\bar{x}$ and covariance P_x
ς	The set of sigma point
n_x	Dimension of random variable x
$\sqrt{\cdot}$	Cholesky decomposition
$(\sqrt{\cdot})_i$	The i-th column of the decomposed matrix
w	Tuning weight
$\mathcal{N}(\bar{x}, \sigma)$	Gaussian distribution with mean $\bar{x}$ and standard deviation
$x \sim \mathcal{N}(\bar{x}, \sigma)$	State x_k under the Gaussian distribution $\mathcal{N}(\bar{x}, \sigma)$
A_{olp}	Overlap area between the predicted drop range, and the one from the experimental envelope
A_{ee}	The area covered by experimental envelope
L_{olp}	Overlap length
L_{ee}	Experimental envelope length at the bottom
R_A	$\frac{A_{olp}}{A_{ee}}$
R_L	$\frac{L_{olp}}{L_{ee}}$

Acronyms

All mathematical symbols used below is valid throughout this dissertation.

ABS	American Bureau of Shipping
BP	British Petroleum Company
DNV	Det Norske Veritas
EOM	Equation of motion
MC	Monte Carlo
2-D	Two-dimensions
3-D	Three-dimensions

Abstract

In marine and offshore engineering, dropped objects, such as drill pipes, anchor chains, containers and some small parts, can accidentally fall into the water from ships or offshore platforms, causing casualties on deck or damage to underwater equipment. Damaged equipment can further harm the environment, such as oil spills from damaged wellheads. Therefore, for safe engineering and environmental protection reasons, we need to develop methods and tools that can predict the trajectory of dropped objects.

In this dissertation, we first study containers dropped from ships. More and more containers are falling into the sea due to bad weather. Containers lost at sea can negatively impact shipping companies, traders and consumers, and the environment. The problem of locating and recycling discarded containers is a challenging engineering problem. We design and implement a series of model tests of small-scale container models to study their falling trajectories for retrieving. We first build a standard 20-foot container model in SOLIDWORKS. Then, export the three-dimensional (3D) geometric model in STL (Standard Tessellation Language) format to the Stratasys F170 Fused Deposition Modeling (FDM) printer. A total of six models, which are made of Acrylonitrile Styrene Acrylate (ASA), are printed for testing purposes. They represent three different loading conditions, different densities, and centers of gravity (COGs). The physical models were dropped into the towing tank of the University of New Orleans (UNO). It was found from the experimental tests that the effect of the initial position after sinking would lead to a certain initial rotational speed, which had a great influence on the lateral displacement, which in turn affected the final landing position. And it can be further observed that these models typically flip for approximately 0-5 cycles during a drop in a water depth of 1.8 meters. This series of model tests not only provided experimental data for the study of the trajectory of box-shaped objects, but also provided valuable references for offshore salvage operations and pipeline layout design.

Another focus of this dissertation is the numerical study of the trajectory of cylindrical objects. We first propose a state-space model of a dropped cylinder based on Aanesland's (1987) 2D equations of motion and Xiang at al. (2016)'s 3D equations of motion. Then we further investigate the heave-pitch coupling term in 3D theory, which was ignored in 2D theory, and find that this term significantly affects the trajectory of dropped cylindrical objects. Then in the state-space model, the original deterministic trajectory is described as a stochastic process by adding small perturbations that satisfy Gaussian distribution to the initial state of the dropped cylinder. Second, three probabilistic methods of state estimation, namely Monte Carlo (MC) method, unscented method, and Cubature method, are used to predict the trajectory envelope of dropped objects and provide reliable results. The MC method is a classical method for solving stochastic problems and has been applied to study the motion of dropped objects. However, it always requires a sufficiently large sample, resulting in a large amount of computation, which is not suitable for practical applications, especially real-time monitoring. The simulation results show that two other advanced statistical methods, unscented method, and Cubature method, give similar results compared to the MC method, but they consume much less computation time. Therefore, the first two methods significantly increase their application possibilities, providing an effective way for envelope prediction of dropped cylindrical objects in marine transportation or marine operations. Furthermore, the Cubature method requires no additional tuning compared to the unscented method, reducing the computation time, making it easier and more suitable for dynamic and real-time risk assessment of dropped objects for maritime transport and installation.

Keywords: Container model, 3D printing, Fused Deposition Modeling (FDM), Trajectory prediction, Dropped cylinders, State-space model, Offshore operations, Monte Carlo method, Unscented Kalman Filter, Cubature Kalman Filter

Chapter 1: Introduction

The dropped object is an object that falls from a vessel to the seafloor, or from the top of an offshore platform to the seabed or the platform itself. With the increasing development of the shipping industry, more and more shipping containers are falling into the sea due to bad weather. Over the past 30 years, containerization has dominated the main market environment where shipping and logistics are operating. It has substantially changed the organizational and institutional relationships of global freight transport. Bernhofen et al. (2015) were the first to propose an identification strategy for estimating the impact of the container revolution on global trade. However, the shipping industry is experiencing the biggest spike in lost containers. More than 3,000 boxes were dropped into the sea last year, and more than 1,000 have fallen overboard so far in 2021 (Koh, 2021). Between October 2020 and February 2021, seven ships on a northern Pacific route from China to the USA loss between 3,000 and 4,000 containers and had a large number of container stacks roll over. (Wasalaski, 2021) There are a host of reasons for the sudden rise in accidents. While unpredictable weather is the main reason, the situation is exacerbated by a surge in e-commerce after consumer demand exploded during the pandemic due to the urgency for shipping lines to deliver products as quickly as possible.

The first part of this dissertation focuses on the trajectory of 3D-printed container models. From the perspective of experimental tests in naval architecture and ocean engineering, carrying out container model tests can provide a reliable theoretical basis for studying the falling trajectory of the containers fallen overboard. However, working with conventional containers made of wood or those manufactured by metal mold is time-consuming, labor-intensive, and costly. Toward this need, additive manufacturing (AM) (also called "3D printing") provides a fast, efficient, and more economical way to make small-scale models for various maritime structures (ABS, 2017; Milewski, 2017). This technology has applications in jewelry, industrial design, architecture, aerospace, dental and medical industries, education, civil engineering, and many other fields (Baumers et al., 2016). It has the advantage of design freedom, mass customization, waste minimization and the ability to manufacture complicated structures, as well as rapid prototyping.

AM started to replace the traditional method of modeling plastic materials in biology, medicine, etc., since it is more economically achievable and environmentally friendly than injection molding and other traditional methods (Baumers et al., 2016; Ford and Despeisse, 2016; Franchetti and Kress, 2016). Ngo et al. (2018) outlined 3D printing, including a survey of its advantages and disadvantages, as a benchmark for future research and development. Arnold et al. (2021) used shrimp shell waste obtained from Louisiana Gulf shrimp as raw material to make the composite filaments and assess its use as a manufacturing material. Arnold et al. (2020) found that the composite filament of polylactic acid and fused filament fabrication can be directly used to make phantoms for education and preoperative planning.

The first objective is to apply the 3D printing technology to fabricate several small-scale container models; the second objective is to experimentally study the trajectories and landing locations of dropped container models in calm water. In addition, it should be addressed that the water-entry itself is not the focus of this dissertation, including the velocity and pressure distribution, etc. In fact, usually when one container drops, it will be flooded with water very quickly, and such process can change the submerged weight. The container may even collapse due to overpressure. There are so many factors to be considered when preparing these experimental tests. To simply our problem, we consider the dropped container model being fully flooded in the water with submerged weight and ignore the possibility of damage. We will focus on the trajectories of dropped container models after sinking.

The models were produced on a Stratasys F170 Fused Deposition Modeling (FDM) printer that uses a filament of plastic material to build 3D objects. The FDM process is the most common 3D printing method to produce parts and models comprised of ABS, PLA, and other common thermoplastics. Due to the similar

density of materials used in the FDM process, we chose to use the method of filling other materials to change the density and the position of the center of gravity of the whole model. Before the FDM printing process begins, the 3D model is sliced into multiple layers based on a layered construction process to produce physical models. Then, the extrusion head, which can move in X and Y directions, locally heats the input material in the form of a plastic filament, causing local melting (Kozior and Kundera, 2017). After depositing a layer of material, the build platform is lowered in the Z direction according to the specified layer thickness and the whole process is repeated until the entire model is completed. The finished products printed by FDM printer are both functional and durable, which makes it a popular process widely used in various industries, including mechanical engineering and parts manufacturers. Figure 1.1 gives a schematic diagram of the FDM printer.

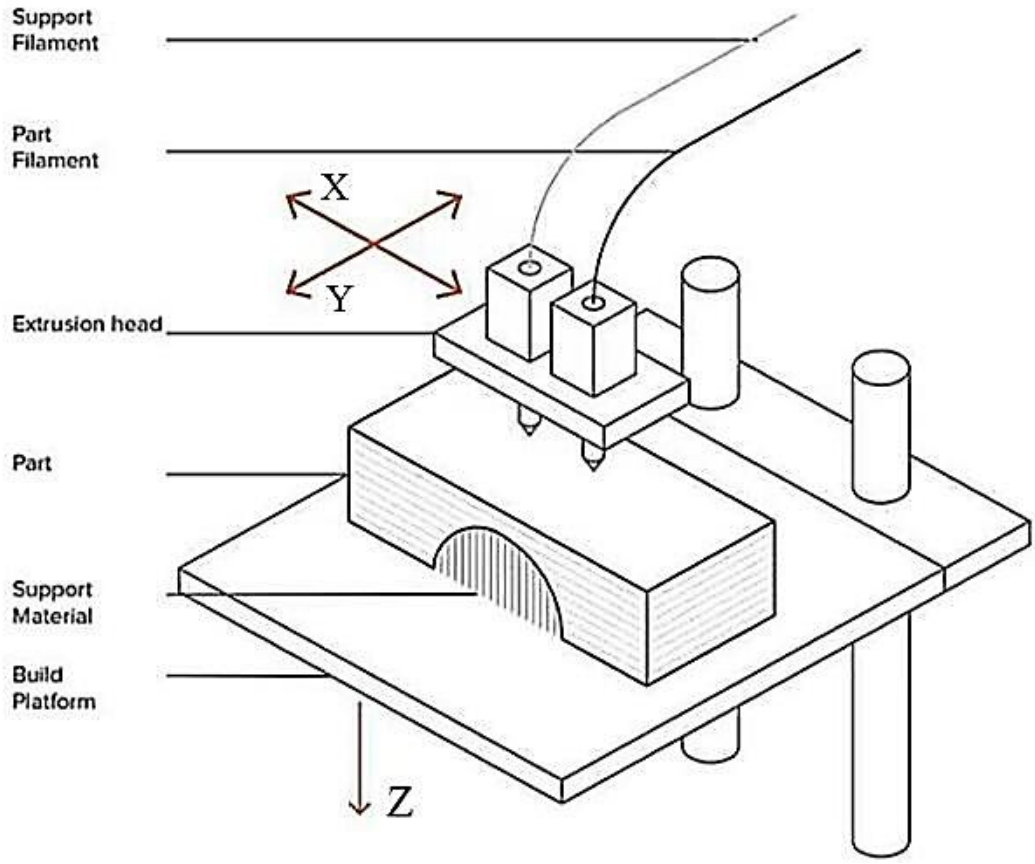

Figure 1.1 Schematic diagram of FDM (Varotsis, 2021)

With the help of support filament and build material, FDM systems are capable of printing models with significant geometric complexity. The support materials will support overhanging structures during printing and help maintain the structural integrity of parts until they are removed by dissolving with an appropriate solvent (Chennakesava and Narayan, 2014).

Like many other 3D technologies, raw FDM parts can display quite visible layer lines on certain objects (3D INSIDER, 2021). Figure 1.2 is the raw surface of our printed container models. The layer lines are noticeable but not rough to the touch. A common way to reduce the surface roughness of FDM parts is by sanding and polishing the model by hand after printing.

Figure 1.2 Raw surface of the container model printed by FDM printer

The Stratasys F170 system provides 5 options to choose from when selecting an infill style, which are sparse, sparse with double dense, hexagram, sparse with high density and solid, as shown in Figure 1.3 from left to right, respectively.

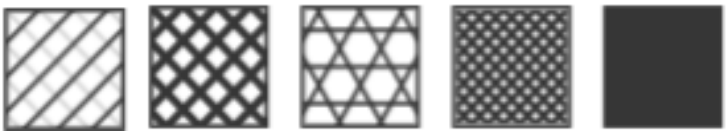

Figure 1.3 Schematic diagram of infill style (Stratasys F170 Protocol, 2020)

In our case, all models use the sparse infill setting with high density. This kind of infill style deposits filament material in a single direction per layer. Compared to fully dense infill settings, it is best to produce parts with high structural integrity with reduced build time and part cost.

Dropped objects cause not only serious economic damage to the shipping industry but also one of the leading causes of death and serious injury in the offshore oil and gas industry. Aanesland (1987) studied the motion state of drill pipe in water through model test and proposed a set of two-dimensional (2D) maneuvering equations to describe drill pipe motion, in which the trailing edge effect of the slender body was considered, and the viscous effect was corrected. He then developed a computer program based on the above numerical analysis to simulate the motion of a free-falling cylinder in water, not only to obtain time series of motion, velocity, and acceleration but also to predict impact loads. A second model test was subsequently performed to validate the program. The model tests revealed that the most important factors include the angle of attack after water entry, the dropped height, etc. A small change in the initial drop angle results in a different drop point. DNV (2010) adopted these findings and incorporated them into the specification, and further presented an overall assessment procedure for analyzing the damage caused by dropped objects, which might have been caused by failure of the supply vessel's lifting operations or storms.

In order to understand the potential damage of dropped objects to underwater facilities during offshore operations, Luo and Davis (1992) proposed a set of differential equations of motion of dropped objects based on the object's own weight, buoyancy, and fluid loading. A computer program, DELTA, was later developed to solve this set of equations. Based on the simulation results, they concluded that the fall angle and height are the key parameters affecting the deflection of the dropped object. Furthermore, the seafloor risk contour is deduced by analyzing multiple simulation results. It provides an effective tool for subsea hazard assessment, risk prevention, and optimization of site layout design. Ingram (1991) video recorded

the paths of tubular with drop angles of 40 and 60 degrees through the laboratory water column and conducted drop experiments in coastal diving areas using tubes over one meter in length and identified tubular through diver surveys position and direction. Colwill and Ahilan (1992) argue that larger objects that occasionally fall from offshore platforms are particularly susceptible to the rotational effects of hydrodynamic loads and may pose a serious threat to the columns and buoys of floating offshore units. However, the design of maximum impact velocity derived from conservative assumptions leads to uneconomical solutions, so the study of the trajectory and maximum velocity of dropped objects helps to design column and pontoon configurations for floating structures. They compared the numerical simulation results of DELTA with the experimental results of Ingram (1991) and Aanesland (1987), respectively, and proved that the prediction of dropped tubular objects has a good correlation with the model experiments. A reasonable derivation is provided for the design impact velocity. Katteland and Øygarden (1995) believe that the oil and gas industry is developing into the field of large water depth, but the industry lacks experience in risk assessment related to dropped objects under large water depth conditions, so it is necessary to develop this technology. Based on the experimental data of Anesland (1987), they used statistical methods to establish a set of distribution equations describing objects dropped from different offshore installations at different water depths. In considering the effects of wind, waves, and currents, they found that the maximum excursion was obtained at a water depth of 180 m.

In recent years, the problem of rigid body motion in the water column has attracted the attention of naval research due to the threat of mines (cylinders) in naval operations. Chu et al. (2005) conducted an experimental study of the hydrodynamic properties of a cylinder falling into the water column. The experiment involved placing three cylinders of painless length into a pool of water and filming the trajectory from two angles. The controlled parameters include the physical parameters of the cylinder (aspect ratio, centroid position) and initial fall conditions (initial velocity and fall angle). Six different trajectory patterns were observed in the experiments, named straight, spiral, flip, flat, seesaw, and combination. Experiments show that the trajectory pattern of a dropped cylinder depends on the initial dropped angle, initial velocity, and the physical parameters of the cylinder, and the position of the centroid has the greatest impact on the trajectory of the cylinder. They concluded a numerical model based on momentum and moment-of-momentum balance based on the experimental results. The model gives good results when simulating the observed motion of a cylinder. Awotahegn (2015) conducted a series of drop tests on 8-inch and 12-inch drill pipes and processed the experimental results using statistical methods. After that, he compared the processed drop distribution probability with the results obtained by the simplified calculation method of DNV and believed that the DNV method would overpredict the probability distribution. Further, he believes that specific hydrodynamic interactions must be considered when numerical simulations of dropped objects.

Xiang at al. (2016, 2017) consider that the industry needs a method to predict where and how dropped objects will go underwater in order to avoid potential hazards to health, safety, and the environment, as well as structural damage. They proposed a new three-dimensional (3D) theory by extending Aanesland's (1987) 2D theory and considering the effect of axial rotation on the falling trajectories of cylindrical objects, and systematically studied various factors that affect the trajectory, such as drop angle, normal drag coefficient, binormal drag coefficient and rolling frequency, the longitudinal center of gravity. The results show that the drop angle and the normal drag coefficient are the most critical factors in determining the trajectory. Then they developed a numerical tool called Dropped Objects Simulator (DROBS) based on this theory. According to the Monte Carlo method, DROBS is used to generate the landing point distribution of a series of dropped cylinders with different dropped angles. The resulting map of landing sites can be used to identify risk-free areas for offshore lifting operations.

Alsosa and Faltinsen (2018) pointed out that DNV (2010) is very conservative, mainly because it simplifies the method of estimating the frequency of objects falling and the probability of impact. Therefore, they propose the 2D+t theory, in which Sarpkaya's work on lateral drag is used to analyze the 3D motion dynamics of an axisymmetric elongated body falling from air into water. And combined with the Slender-body theory for the potential flow of incompressible water to explain viscous cross-flow separation in the

submerged phase. In addition, asymmetric vortex shedding triggering important 3D motions is also considered. The numerical analysis results of this theory are compared with those of Aanesland's drop experiment to verify its accuracy.

In this dissertation, the second part is about statistical analysis of the trajectory envelope of dropped cylinders. Firstly, the 3D theory of Xiang at al. (2017) is used to describe the motion of a cylinder in water. By constructing a state space model, we can easily solve the time histories of various resistance components of the cylinder, and their combination may significantly determine the trajectory of the cylinder. Secondly, we select the initial dropped angle, initial velocity, and the physical parameters of the cylinder as the important parameters of the trajectory of the cylinder. Therefore, when we solve the equations of motion, we add random small noises in the initial state, i.e., the velocities and dropped angles in x-, y-, and z-direction, the trajectory envelope of the cylinders is then obtained by statistically processing a significantly large number of trajectories with noises. It should be addressed that we have chosen three statistical methods, e.g., the Monte Carlo method, the unscented method, and the Cubature method. As the most common random sampling method, the MC method is often applied to solve the same kind of problems (Xiang at al., 2016). Meanwhile, the unscented method and the Cubature method, which are the well-known trajectory tracking algorithms in electronic engineering, are also adopted. The trajectory envelopes computed by these three methods are compared with the 2D experimental envelopes published in (DNV, 2010) to verify their accuracy.

Specifically, our study of dropped objects is divided into two parts: the container model and the cylinder model. Chapter 1 explains the motivation for this research and how this research can help address the practical problem of dropped objects in the offshore industry. Chapter 2 describes the setup and detailed steps for the container model experiment. The third chapter introduces the specific parameters of the 3D printing model in detail, and organizes the data collected by the model experiment through statistical methods to obtain a series of charts. Chapter 4 presents state-space models derived from 2D and 3D theory and provides an in-depth look at three statistical methods for obtaining trajectory envelopes. Chapter 5 presents 2D and 3D trajectory envelopes based on state-space models and compares them with the experimental envelopes of Aanesland (1987). Chapter 6 states the conclusions drawn from all the facts gathered throughout the study. These conclusions allow the related research to be applied in practical engineering.

Chapter 2: Experimental setup for container models

The University of New Orleans Towing Tank is filled with fresh water up to 173 cm deep. The towing tank is 30.6 m long and 4.6 m wide as shown in Figure 2.1. A carriage was moved to the center to perform the experimental drops. There are various windows of different sizes on the wall of the towing tank to observe and record the experimental process. A carriage across the water surface, which can be slided along the rails on both sides. The plate on the carriage is the working position of this drop test, which is about 35 cm away from the water surface. In Figure 2.2, two iron grids used to measure the trajectory and drop point of the dropped objects are fixed on the wall and bottom of the towing tank, respectively. The size of the grid is about 211cm*211cm, and the size of each small square inside is 15cm*15cm. There is a camera outside the observation window and above the carriage to record the experimental process.

Figure 2.1 The towing tank at the University of New Orleans

Figure 2.2 The experimental setting

Figure 2.3 Overview of grid mat laid on the bottom of towing tank

Figure 2.4 The observing system

A series of drop tests have been performed in the towing tank at the University of New Orleans (UNO). Figure 2.3 is an overview of horizontal grid mat laid on the bottom of towing tank, which can be used to measure the final landing locations of container models. Figure 2.4 shows a vertically installed grid, which can be used to roughly track and record the position of the container model at each moment. In addition, Figure 2.4 also shows a small white device used to adjust the drop angle, so that we can easily implement the three drop angles in this study.

Figure 2.5 shows a flowchart about the major five steps to be implemented in this study. First, we use commercial software, SolidWorks, to construct 3D geometrical models. In this design stage, we insert a hole in different positions to adjust the average density and center of gravity (COG) by filling different high-density heavy metals to represent different loading conditions of containers. Next, these geometric models are then exported to a Stratasys F170 Fused Deposition Modeling (FDM) printer. In total, six models were made of acrylonitrile styrene acrylate (ASA) and printed for the purpose of testing. They represent three different loading conditions with different densities and COG, and there are two samples for each condition. The third step is to measure the geometric dimensions of the 3D-printed models and measure and estimate their COG to see if they meet our design requirements and other specifications, such as ABS (2018). This step is also important for 3D printing quality control.

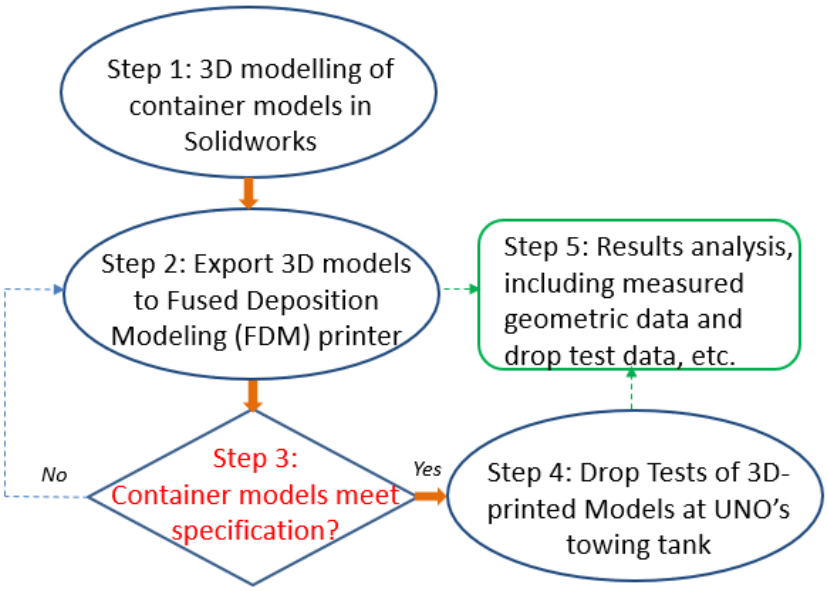

Figure 2.5 Flowchart for major steps

After measuring and determining the basic parameters of these six models, we dropped four models with a density greater than water into UNO's towing tank and performed a series of drop tests to obtain data on the fall and the trajectory of these physical models after entering the water. Figure 2.6 shows a schematic view of the drop test plan. Finally, all the collected data, including the 3D printing data, the measurement data of 3D printed models, and the data from drop tests, will be finally analyzed.

It should be addressed in advance is that in the experimental tests, the time interval between each drop is long enough, so ideally the influence of water waves can be ignored.

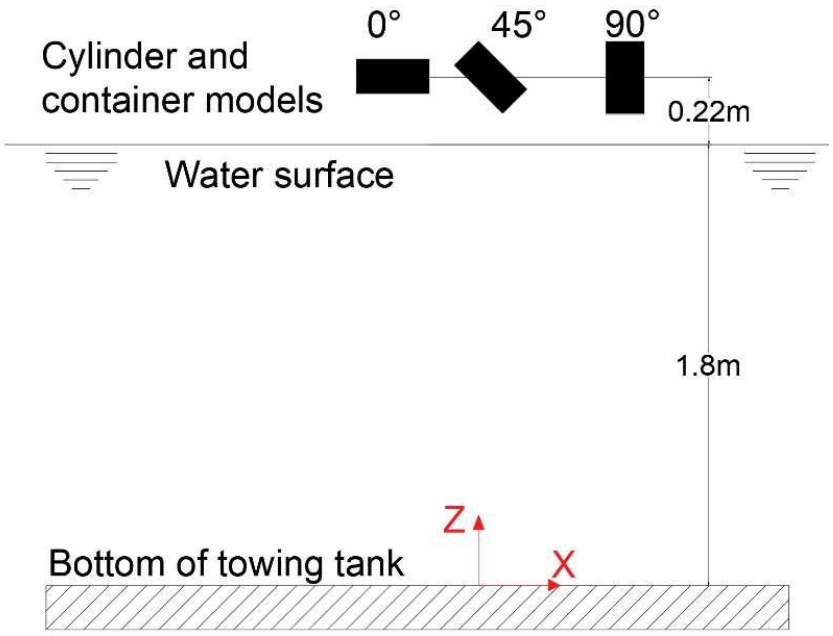

Figure 2.6 A schematic view of drop test plan (container + cylinder)

Chapter 3: Case Study I - 3D-printed Containers

Generally, there are 14 different most common types of containers, including dry containers, side open storage containers, half-height containers, drums, etc. (Chawa and Mukkamala, 2018). In this dissertation, the standard 20 ft dry container is selected to be scaled with ratio 35.69:1. This design was finalized after some consideration, including the maximum allowable dimensions of the FDM printer. As a result, the finalized size of the container model is $169 \times 68 \times 72$ mm (Length × Width × Height). Table 3.1 gives the dimension of the original and the scaled container.

Table 3.1 Original Container vs. Container Model

	Length (mm)	Width (mm)	Height (mm)
Standard 20ft container	6058	2438	2591
Scaled container model	169	68	72

To construct the container models with different weights and centers of gravity, we design containers with a hole of 25 mm in diameter and 50 mm in depth placed in the middle and upper of models, respectively. In doing so, we can fill the holes with different materials to change the weight and COG with centric hole (Figure 3.2), type II - scaled model with eccentric hole (Figure 3.3) and type III - scaled model without hole (Figure 3.4). These three model types will share the same front design, as shown in Figure 3.1.

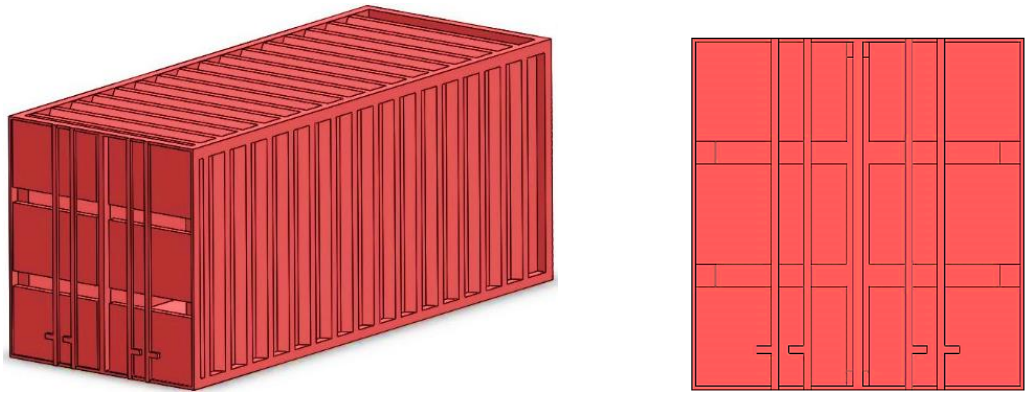

Figure 3.1 The same front view for all the three types of container model- Model Type I, Model type II and Model Type III.

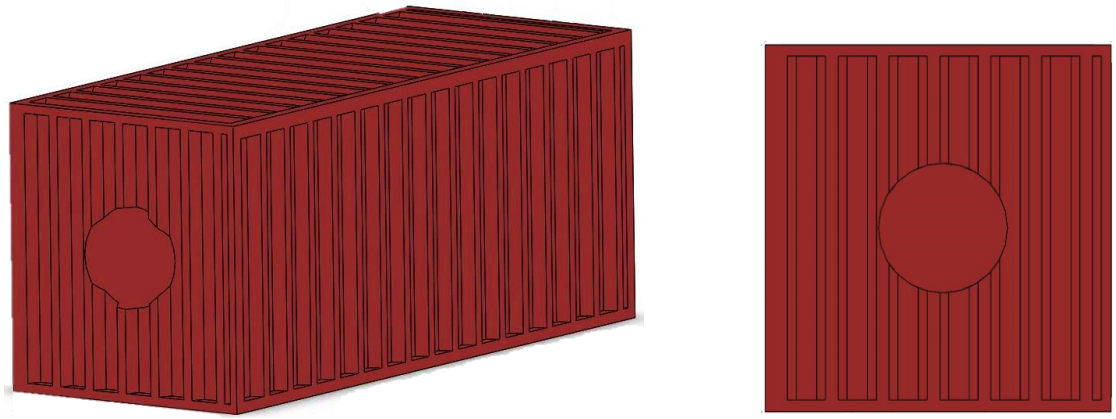

Figure 3.2 Back view of Model type I –with a centric hole

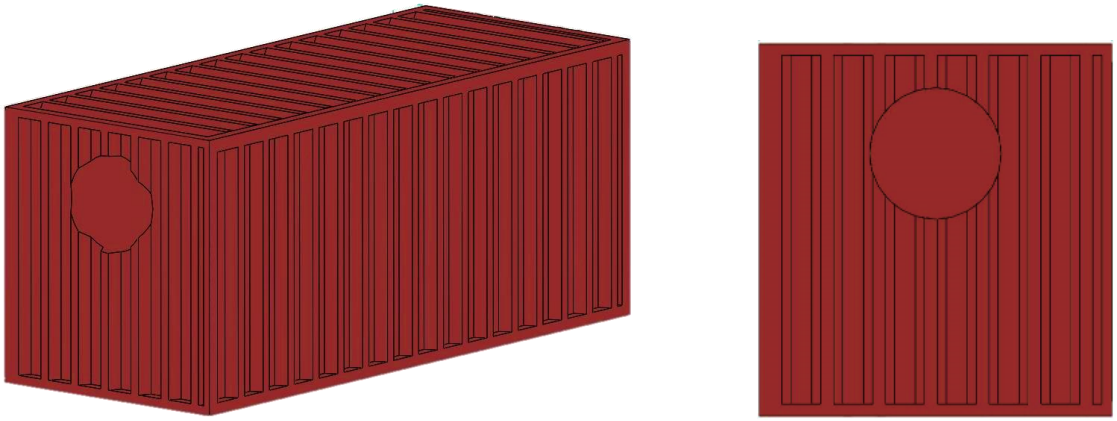

Figure 3.3 Back view of Model type II - with an eccentric hole

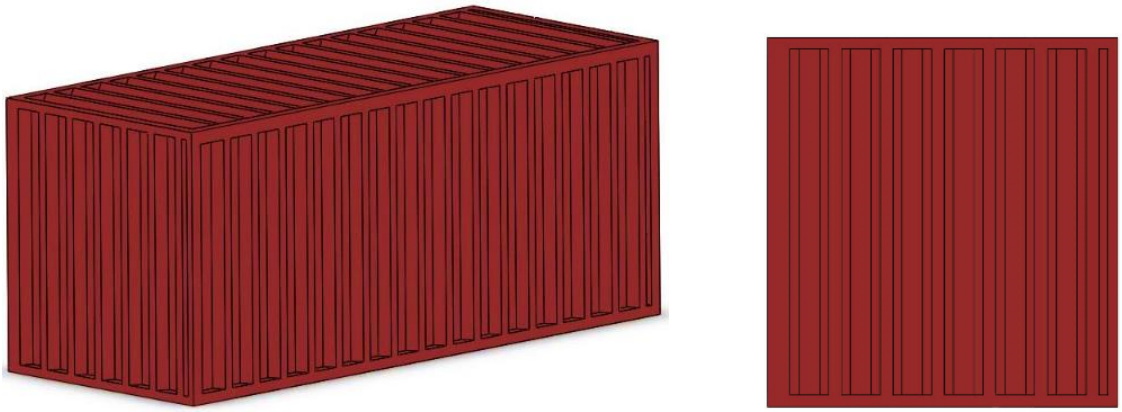

Figure 3.4 Back view of Model type III – with no hole

In order to import the SolidWorks model into the 3D printer, we only need to save the original file as an STL file. This ASCII or binary format file can describe the surface geometry of 3D objects as primitive, unstructured triangular surfaces.

3.1 Properties of dropped containers

A total of 6 models are printed, 4 with holes and 2 solid models, as shown in Figure 3.5.

Figure 3.5 Six 3D-printed models

We use a Vernier caliper to measure the basic dimensions of the 3D printed container models for multiple times. The averaged measured value will be compared with the targeted dimensions defined in SolidWorks.

In addition, the drainage method is used to measure the displaced volume of the model to estimate the density. Figure 3.6 shows how to find the COG of these container models, and each model is measured multiple times to reduce the measurement error as shown in Figure 3.7.

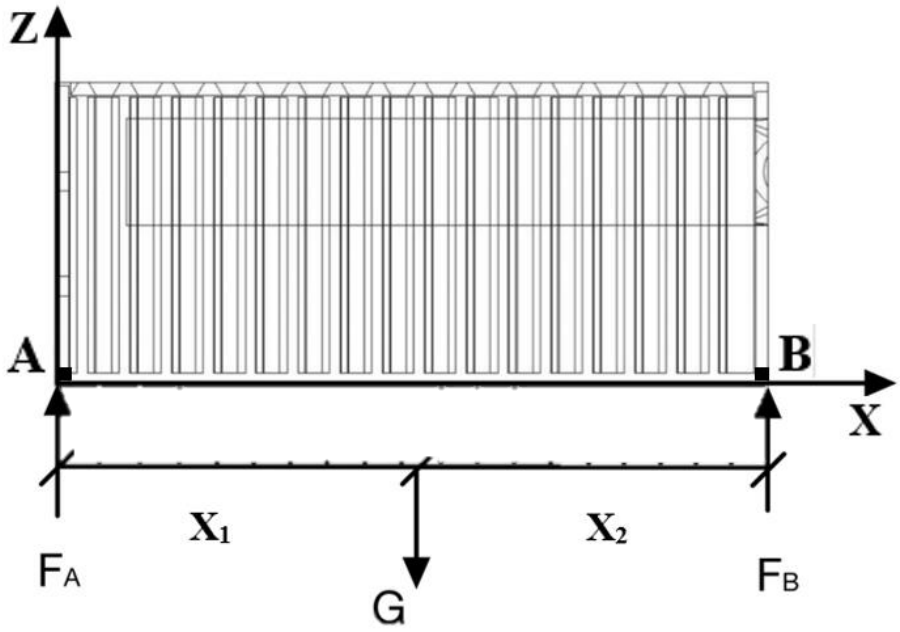

Figure 3.6 Schematic diagram of moment balance

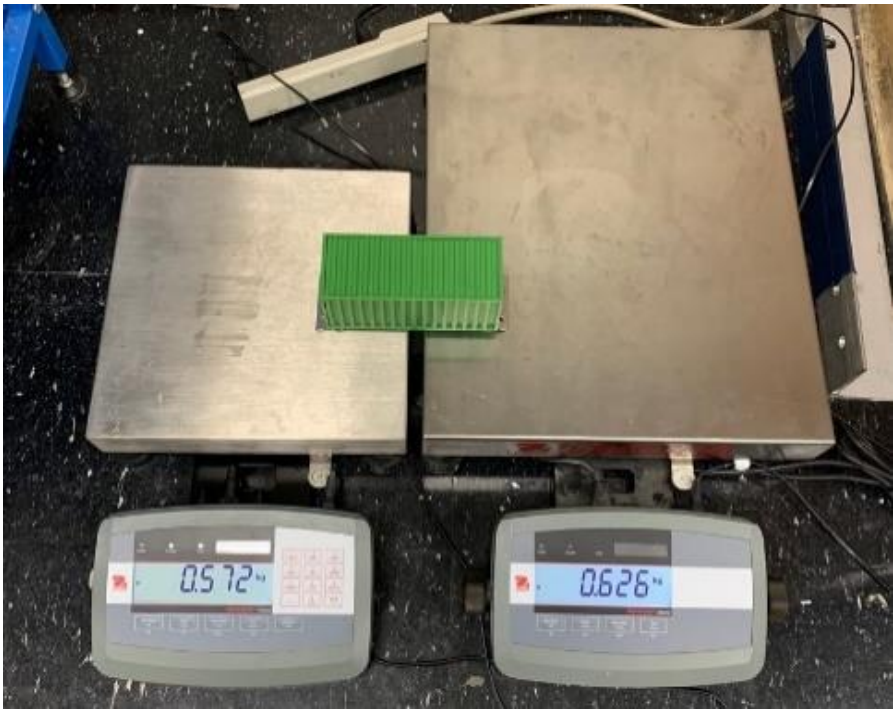

Figure 3.7 Equipment used for actual measurement

All models are made of acrylonitrile styrene acrylate (ASA) material, which is a thermoplastic elastomer. According to Odian (2004), elastomers are the group of polymers that are prone to very large reversible elongation under relatively low stress. This requires the polymer to be completely (or almost completely) amorphous with a low glass transition temperature and low secondary forces to obtain high polymer chain mobility. Meanwhile, thermoplastic is defined as a polymer that can be melted and recast almost indefinitely. These characteristics make ASA suitable to be melted and printed as a 3D printing material.

Figure 3.8 presents the Stress-Strain plots for a typical elastomer, a flexible plastic, a rigid plastic, and a fiber, where the modulus of a polymer is the initial slope of each curve; the tensile strength and ultimate elongation are the highest stress and elongation values, respectively (Odian, 2004). Elastomer has a smooth Stress-Strain curve, which almost obeys the general Hooke's law with no strain hardening region or necking region being observed. This can ensure that the model is not easily damaged during the drop test.

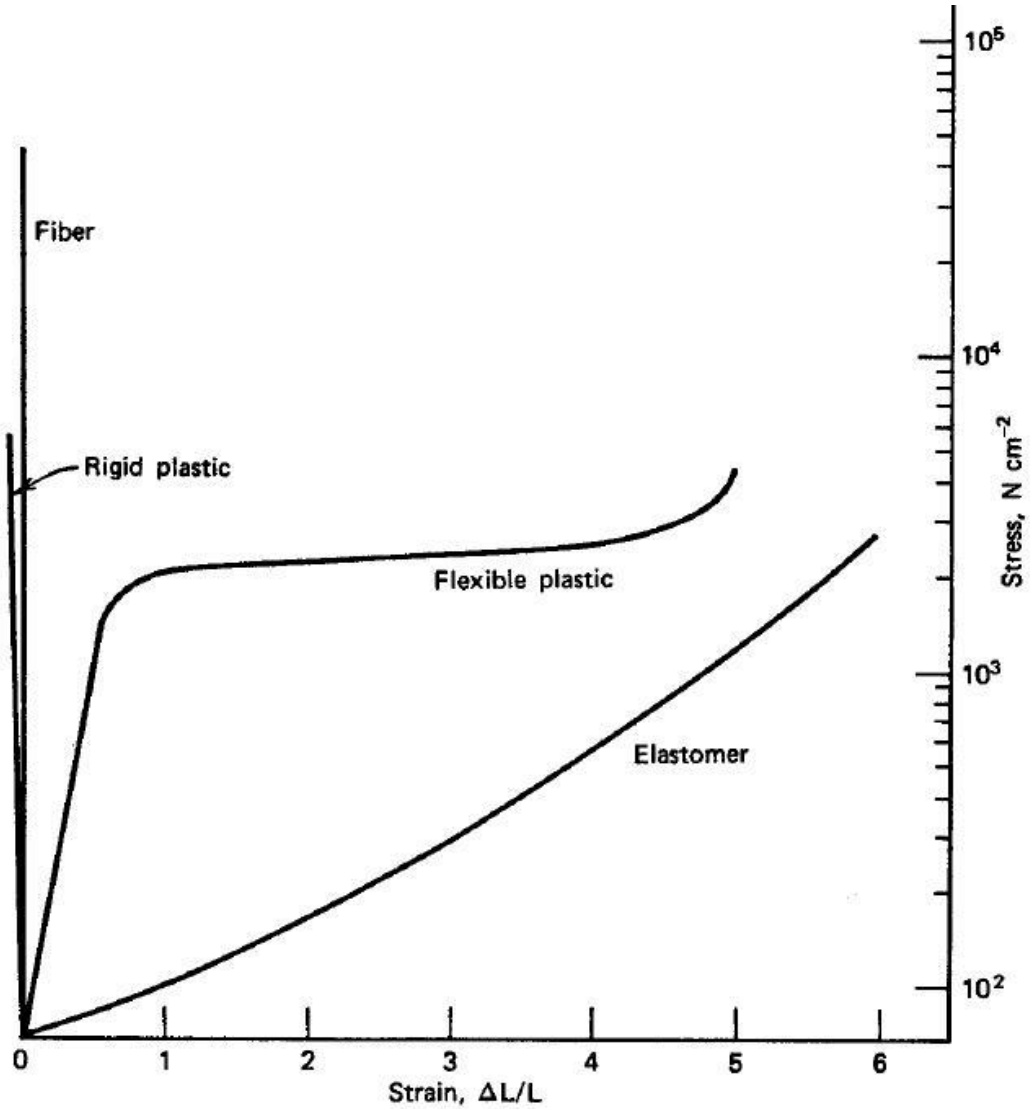

Figure 3.8 Stress-Strain plots (Odian, 2004)

Also, ASA is amorphous and has mechanical properties similar to ABS plastics. However, its characteristics are much less affected by outdoor weathering. ASA parts have good chemical and heat resistance, as well as high impact strength and color fade/aging/yellowing resistance, even at low temperatures. Table 3.2 gives some basic properties of ASA.

Table 3.2 Basic properties of ASA

Density	1.00 - 1.24 g/cm^3
Hardness	75 - 119
Modulus of Elasticity	1.45 - 2.80 GPa
Strength at break	47 – 56 MPa
Melt Temperature	170 - 280 °C
Drying Temperature	70 - 100 °C

Two materials, aluminum, and steel are used to fill the model. After calculations, it was found that when aluminum is filled into the model, the density of the whole model is slightly larger than that of water. This is very helpful for observing the trajectory of the container model in the hydrostatic test. As a result, aluminum is selected. Meanwhile, to highlight the comparison between experimental models, steel is chosen as another filling material because of its high availability and larger density. Table 5.3 gives the basic properties of these two fillers.

Table 3.3 Properties of fillers

Filler	Density (kg/m^3)	Mass (kg)
Aluminum	2317.99	0.18
Steel	7756.83	0.59

Table 3.4 shows the data obtained via the Vernier caliper. The relevant definitions of dimensions are illustrated in Figure 3.9. The difference between each model is quite small.

Table 3.4 Dimensions of container models

Model No.	Position of the hole	Filler	a (mm)	b (mm)	c (mm)	d (mm)	e (mm)	f (mm)	g (mm)	h (mm)
1	Centric	Aluminum	68.30	72.20	169.50	22.80	26.40	20.90	24.10	23.10
2		Steel	68.00	72.10	169.50	22.10	26.10	19.80	23.50	23.40
3	Eccentric	Aluminum	68.00	72.10	169.60	23.00	25.00	20.00	38.30	8.90
4		Steel	68.00	72.10	169.70	22.70	25.40	19.90	38.10	8.80
5	No Hole		68.20	72.20	169.30					
6			67.90	72.00	170.90					

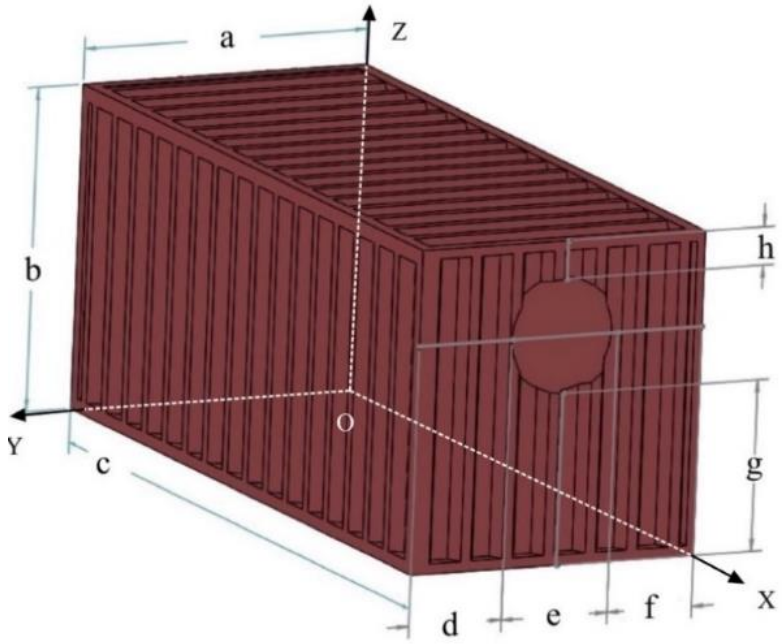

Figure 3.9 Dimension definition of container model

Since the size of the original model is $a \times b \times c = 68 \times 72 \times 169$ mm, it is important to confirm that the 3D printed model has sufficient accuracy, or that the deviation is small enough. As a result, we calculate the deviation percentage of the model size, as shown in Table 3.5. We use d_a to d_h to represent the deviation percentage of a to h, respectively. It can be said that, considering manual errors and mechanical errors, the actual parameters of printed models are very close to the designed parameters and meet our requirements.

Table 3.5 Difference percentage of the model size

Model No.	Position of the hole	Filler	Difference percentage							
			d_a (%)	d_b (%)	d_c (%)	d_d (%)	d_e (%)	d_f (%)	d_g (%)	d_h (%)
1	Centric	Aluminum	0.44	0.28	0.30	2.47	3.94	2.70	3.17	0.60
2		Steel	0.00	0.14	0.30	0.67	2.76	2.70	0.60	0.69
3	Eccentric	Aluminum	0.00	0.14	0.36	3.37	1.57	1.72	0.52	4.71
4		Steel	0.00	0.14	0.41	2.02	0.00	2.21	0.00	3.53
5	No Hole		0.29	0.28	0.18					
6			0.15	0.00	1.12					

Based on the information of geometry and mass density, we can calculate the COG after container models are filled, as shown in Table 3.6. Here, we only measure Model No. 1 to Model No. 4, which are filled with aluminum and steel. This is because that Model No. 5 and Model No. 6 are so light that they can float on the water, so they are not used in the drop test.

Table 3.6 Estimated COG after filling

Model No.	Position of the hole	Filler	Center of gravity (mm)		
			X_g	Y_g	Z_g
1	Centric	Aluminum	85.32	34.09	35.69
2		Steel	88.53	33.50	35.80
3	Eccentric	Aluminum	85.97	34.49	37.84
4		Steel	88.53	33.68	42.53

Also, we have calculated the eccentricity of these container models after filling and organized the data in Table 3.7.

Table 3.7 Eccentricity after filling

Model No.	Position of the hole	Filler	Eccentricity (mm)		
			X_e	Y_e	Z_e
1	Centric	Aluminum	0.57	0.06	0.40
2		Steel	3.78	0.50	0.25
3	Eccentric	Aluminum	1.04	0.34	1.74
4		Steel	3.68	0.32	6.48

Table 3.8 shows the densities and mass of Models No. 1 - No. 4 before and after filling. It shows that the density is increased by 27% if the filling material is aluminum, and 100% for steel. Thus, the four models can be used to represent four significantly different loading conditions.

Table 3.8 Total mass/density before and after filling

Model No.	Position of the hole	Filler	Total mass before fill (kg)	Total mass after fill (kg)	Density before fill (kg/m^3)	Density after fill (kg/m^3)	Increased ratio
1	Centric	Aluminum	0.65	0.83	826.14	1053.30	27.50%
2		Steel	0.60	1.20	758.88	1519.04	100.17%
3	Eccentric	Aluminum	0.65	0.83	826.14	1053.30	27.50%
4		Steel	0.59	1.19	752.54	1506.35	100.17%

3.2 Results and discussions

Now that we have the experimental data of where the object falls, we prepare to sort out the specific falling point and calculate the angular deviation, α, as well as lateral deviation, δ, so as to compare with the data given in the Det Norske Veritas (DNV) rule (2010).

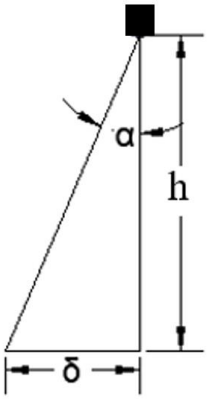

Figure 3.10 Schematic diagram of angular deviation and lateral deviation

Referring to Figure 3.10,

$$\delta = h \cdot \tan \alpha \tag{5.1}$$

The angular deviation is:

$$\alpha = \arctan\left(\frac{\delta}{h}\right) \tag{5.2}$$

With the experimental data, we could also obtain the distribution of falling container models in a different area, from which we could calculate the hit probability. Assuming landin locations on the horizontal position of the bottom to be normally distributed, we could have:

$$p(x) = \frac{1}{\sqrt{2\pi}\delta} e^{-\frac{1}{2}\left(\frac{X}{\delta}\right)^2} \tag{5.3}$$

Similar to DNV rule (2010), the probability P_r within a ring area with an inner radius r_i and an outer radius r_o can be found by:

$$P_r = P(r_i < r \leq r_o) = P(r \leq r_o) - P(r \leq r_i) \tag{5.4}$$

The ring area A_r can be easily calculated as:

$$A_r = \pi\left(r_o^2 - r_i^2\right) \tag{5.5}$$

The probability per area, P_{A_r}, is defined by dividing the hit probability P_r by the area of circle with radius r:

$$P_{A_r} = \frac{P_r}{A_r} \tag{5.6}$$

Figure 3.11 – 3.14 show the landing locations of Model No. 1 to No. 4, respectively. The four models have been dropped at UNO's towing tank at three different drop angles - $0^o, 45^o \; and \; 90^o$, with 20 times for each angle, so the total number of drops is 240. It should be addressed that the time interval between each test usually depends on whether the waves originated from the water-entry of previous tests have decayed or not. In other words, we try to ensure that we perform the drop tests in calm water. However, due to the large number of tests, it is difficult to remove various types of external noise, including small waves from previous tests, and the waves reflected by tank's wall, etc. Therefore, considering that these random noises are inevitable, we repeat five times for each model at each drop angle.

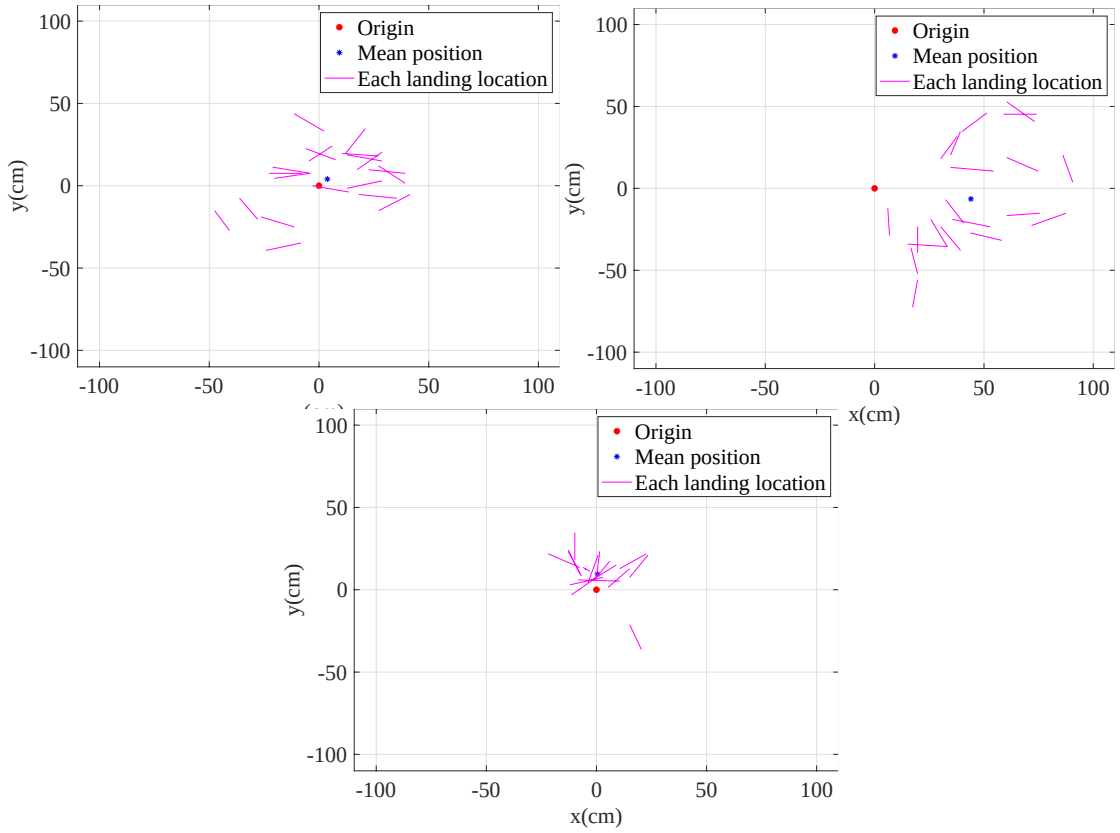

Figure 3.11 Landing location distribution of Model No. 1 at 0° (top left – 'a'), 45° (top right – 'b') and 90°(bottom – 'c')

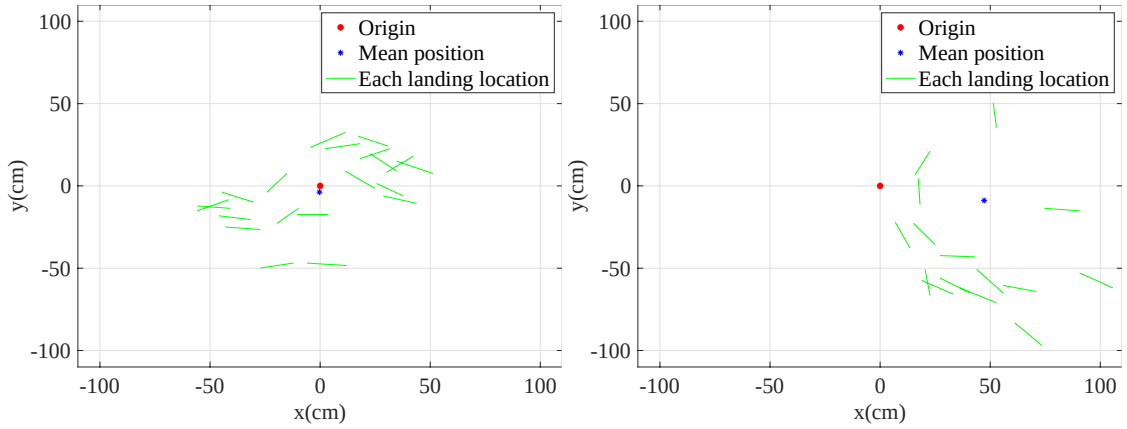

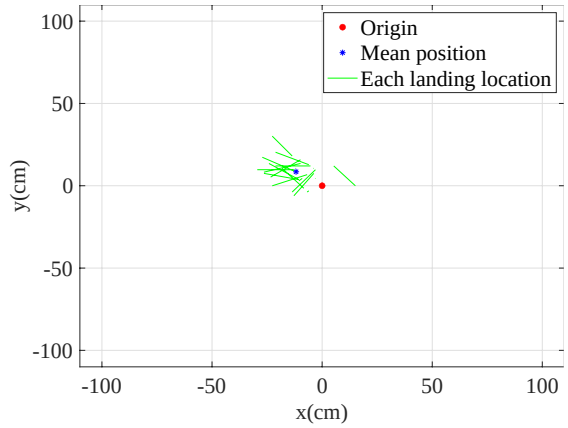

Figure 3.12 Landing location distribution of Model No. 2 at 0° (top left – 'a'), 45° (top right – 'b') and 90°(bottom – 'c')

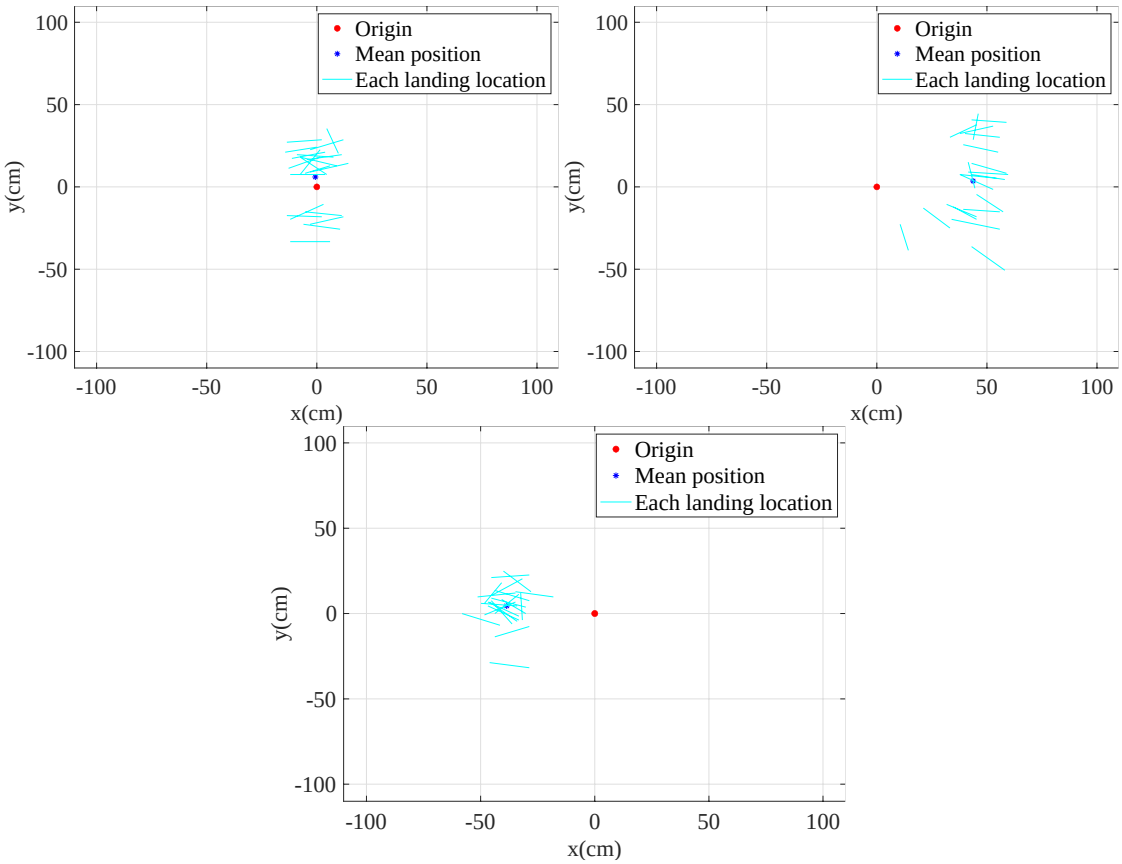

Figure 3.13 Landing location distribution of Model No. 3 at 0° (top left – 'a'), 45° (top right – 'b') and 90°(bottom – 'c')

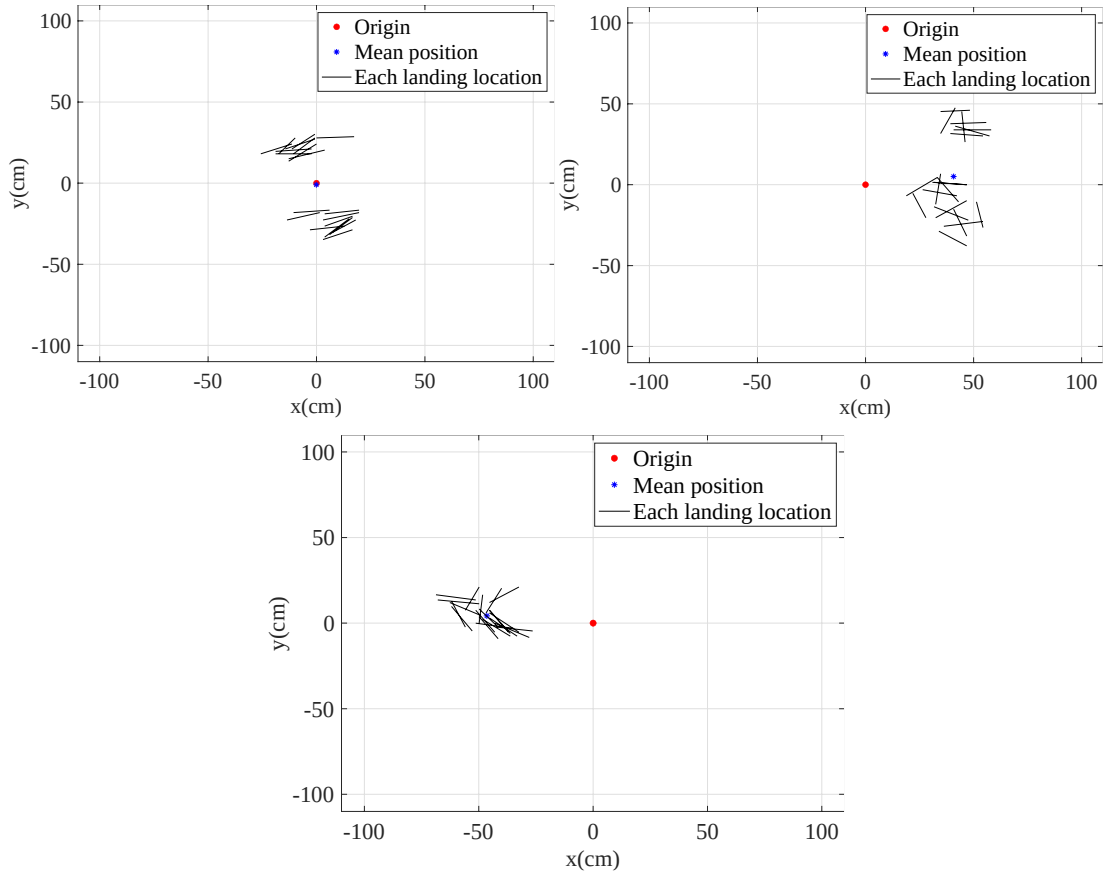

Figure 3.14 Landing location distribution of Model No. 3 at 0° (top left – 'a'), 45° (top right – 'b') and 90°(bottom – 'c')

The drop angle is a very important factor since it affects the degree of dispersion of those landing locations. A 90-degree drop angle usually corresponds to a more concentrated landing location distribution, as can be observed from Figure 3.11(c), Figure 3.12(c), Figure 3.13(c), and Figure 3.14(c). Accordingly, the relatively smaller standard deviation (STD) of radius can also be found in Table 5.9; that is, 8.0cm, 6.5cm, 4.9cm, and 8.4cm, respectively. It may be because the 90-degree drop angle means the smallest water-entry area when compared with all the other drop angles. The larger the contact area between the model and the calm water surface, the greater is the interference caused by the entry of water, indicating that it is more likely to cause the surge velocity along the length direction and rolling rate in the water, thereby causing more significant drift.

In addition, Models No. 3 and No. 4 have an eccentric COG in Z direction, if compared with Models No. 1 and No. 2, which have a centric COG in Z direction. Such an eccentricity can cause a greater drift but more concentrated distribution, as shown in Figs. 18 and 19, if compared with Figs. 16 and 17, especially for 90-degree case. This could be further validated by a greater mean value of the radius, but smaller STD, as shown in the last two columns of Table 3.9.

It should be also addressed that the density of Model No. 2 is about 1519.04 kg/m^3, greater than Model No. 1 with 1053.30 kg/m^3, as shown in Table 3.8. Similarly, the density of Model 4 is about 1506.35 kg/m^3, heavier than Model No. 3 with 1053.30 kg/m^3, too. The effect of density on the landing locations seems not obvious in these tests. However, the density does strongly affect the landing time. As

clearly summarized in Table 3.10, Model No. 2 needs much less time to touch the tank bottom if compared with Model 1 for all the three drop angles, and similar findings can be also applied to Model No. 4 and Model No. 3.

Table 3.9 Statistical value of landing locations for each model

Model No.	Drop angle	Mean (cm)		Max (cm)		Min (cm)		STD (cm)		Mean (cm)	STD (cm)
		x	y	x	y	x	y	x	y	r	r
1	0º	3.8	4.1	34.4	38.5	-44.2	-37.0	22.8	18.4	27.3	10.4
	45º	44.0	-6.5	88.3	46.8	6.4	-64.2	22.6	31.9	55.8	18.4
	90º	0.5	9.5	19.3	26.4	-14.7	-28.7	9.9	10.9	15.3	8.0
2	0º	-0.3	-3.8	43.0	27.9	-48.7	-48.4	30.6	22.3	35.5	10.9
	45º	47.2	-8.9	98.2	87.5	10.2	-89.9	25.0	60.7	74.5	30.1
	90º	-11.8	8.5	10.2	24.1	-21.1	-3.4	7.4	6.2	16.2	6.5
3	0º	-0.7	6.0	7.2	27.9	-7.2	-33.3	4.4	19.3	19.2	6.5
	45º	43.7	3.6	51.3	40.0	12.5	-43.5	9.4	24.4	50.0	8.8
	90º	-38.6	4.5	-26.4	21.8	-49.8	-30.3	4.9	11.1	40.3	4.9
4	0º	-0.1	-1.0	12.8	28.3	-18.5	-31.8	10.1	23.9	25.0	4.3
	45º	40.8	5.1	52.9	45.6	24.9	-33.3	7.3	25.6	47.3	11.5
	90º	-46.5	4.3	-34.4	16.6	-60.0	-4.2	8.2	6.9	47.1	8.4

Note: $r = \sqrt{x^2 + y^2}$, and it represents the radius of landing location.

Table 3.10 Average Falling Time

	Elapsed time (s)		
Model No.	0º	45º	90º
1	3.71	3.21	1.94
2	1.8	2.04	0.92
3	3.77	3.53	2.07
4	1.99	1.93	1.25

Figure 3.15 shows a sample scenario of landing location of four container models, and Figure 3.16 is postprocessed in MATLAB by putting all the 240 landing locations in one figure.

Further, these 240 landing locations are classified according to a certain interval. The radius of the interval δ, which is defined in Equation (3.1) according to DNV (2010), corresponds to a certain drop angle α. Table 3.11 shows the angular deviation and its corresponding lateral deviation.

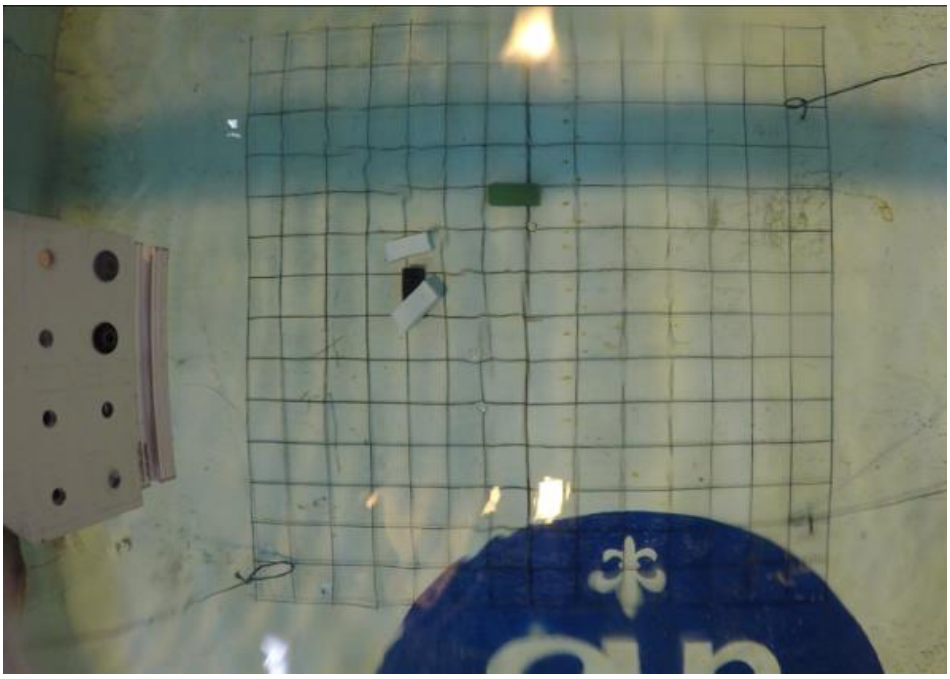

Figure 3.15 A scenario of landing location of four container models

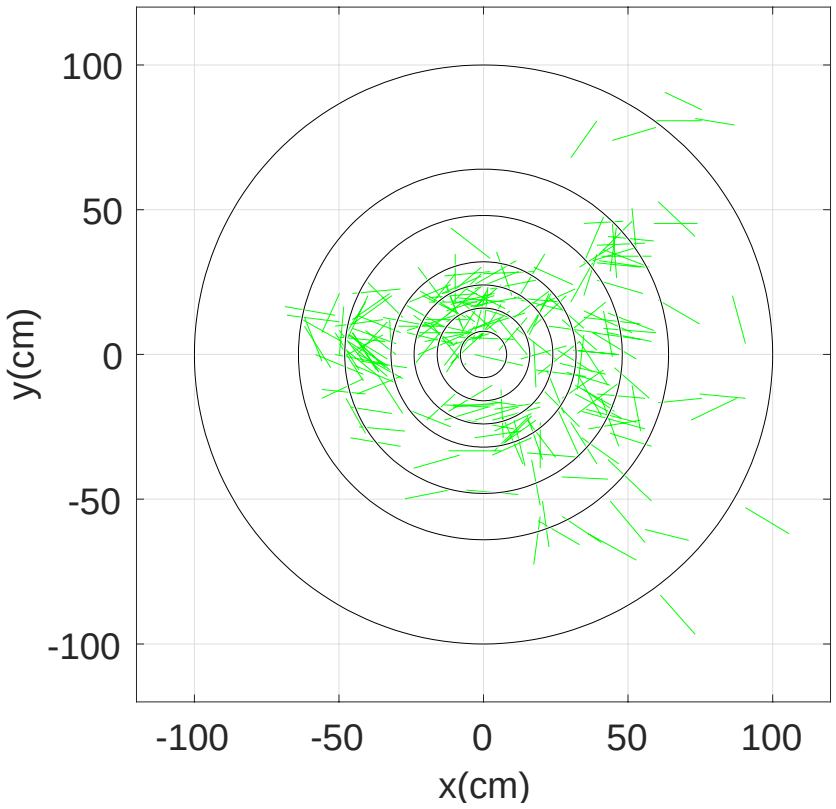

Figure 3.16 Landing location distribution postprocessed in MATLAB

Table 3.11 Angular deviation and its corresponding lateral deviation

α (°)	0	2.54	5.08	7.59	10.08	14.93	19.57	29.05
δ (cm)	0	8	16	24	32	48	64	100

Therefore, the probability of falling into a certain interval can be calculated by dividing the number of times falling in each interval by 240. The best fitting Rayleigh distribution under maximum likelihood estimation flamework is shown in Figure 3.17. This probability density function can be further integrated to get the cumulative distribution function (CDF) as shown in Figure 3.18.

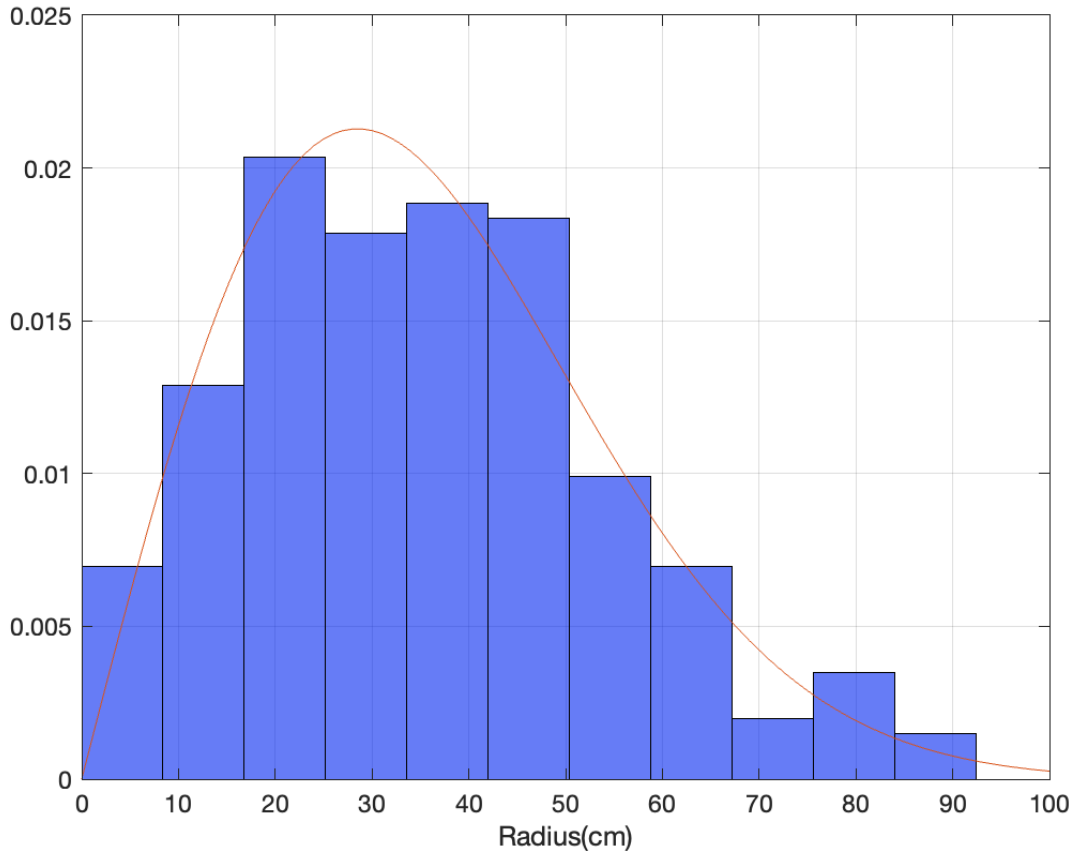

Figure 3.17 Probability histogram of dropped container models with a fitting Rayleigh distribution

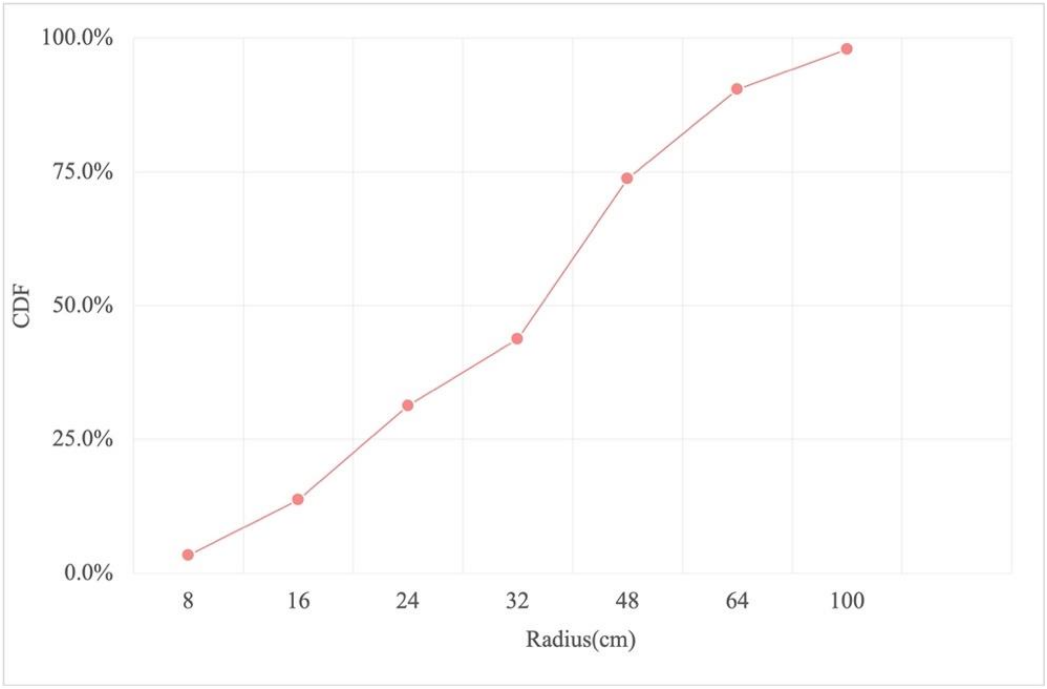

Figure 3.18 Cumulative distribution function of dropped container models

If further referring to the definition of these two parameters- the angular deviation and lateral deviation in the DNV rule (2010) specification and the calculated results listed in Table 3.11, these experimental data indicate that for relatively light square objects, there is a high probability that these objects will enter the water surface with a drop angle of 15^o even 30^o. It should be noted that all the small-scaled models are less than 2 kg, much ligher than the actual full scale offshore structues categorized in DNV rule (2010). In the guidance (DNV, 2010), the angular deviation is 2^o for weight much greater than 8 tonnes, 3^o for weight about 8 tonnes and 5^o for weight between 2 tonnes and 8 tonnes. All these indicate that the angular deviation of light objects is often smaller, and it could be larger for heavy objects. This is completely consistent with our intuition.

These experimental data have strong practical value. With reference to DNV rule (2010) and Yasseri (2014), we can obtain the plot of probability per area, P_{A_r} as shown in Figure 3.19. These results can be used in further risk analysis, including pipeline protection design, and so on.

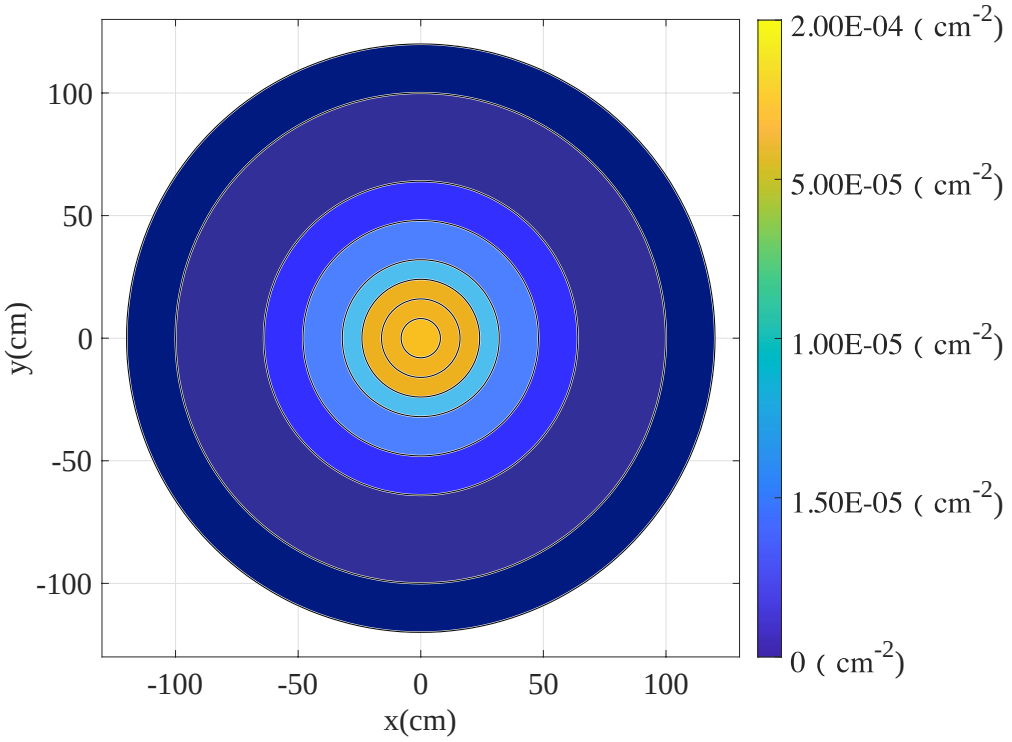

Figure 3.19 Probability per area, P_{A_r}, based on the experiemtal data

In the experimental tests, it is also found that rolling has an important influence on the lateral displacement y. The initial rolling rate depends on the water-entry condition, including the container's vertical speed and angle of entry. This finding is consistent with other findings for cylindrical objects (Aanesland, 1987; Yu, 2020b). Inspired by the work of cylindrical objects, the experimental test of this research aims to study the falling mechanism of box-shaped objects. This experiment may be the earliest experiment to test the trajectory of box-shape objects. Considering that the 3D-printed container models used are highly like the real container, the experimental data from these tests can be applied to real maritime salvage operations.

Finally, the falling pattern of container models can be vividly displayed in Figure 3.20. Through this experiment, it can be observed that the sunken container model will fall along a curve, similar to an inverted quadratic or even higher-order parabola. Meanwhile, the lateral displacement of those models is also observed. This value mainly depends on the rolling rate, which largely depends on the interaction when entering the water. It can be further observed that these models usually have to flip 0-5 cycles, with the water depth 1.8 meter.

In addition, it should be pointed out that the aspect ratio is about 2.48 (= 6058 / 2438), much smaller than 5.0 which is the minimal ratio for the slender-body cylindrical objects in offshore engineering. Obviously, this falling-pattern of container models is much simpler than the proposed six patterns for cylindrical objects in Aanesland (1987).

This plot in Figure 3.20 can be combined with the drop time summarized in Table 3.10, to understand the fundamental pattern of box-shape objects at different drop angles.

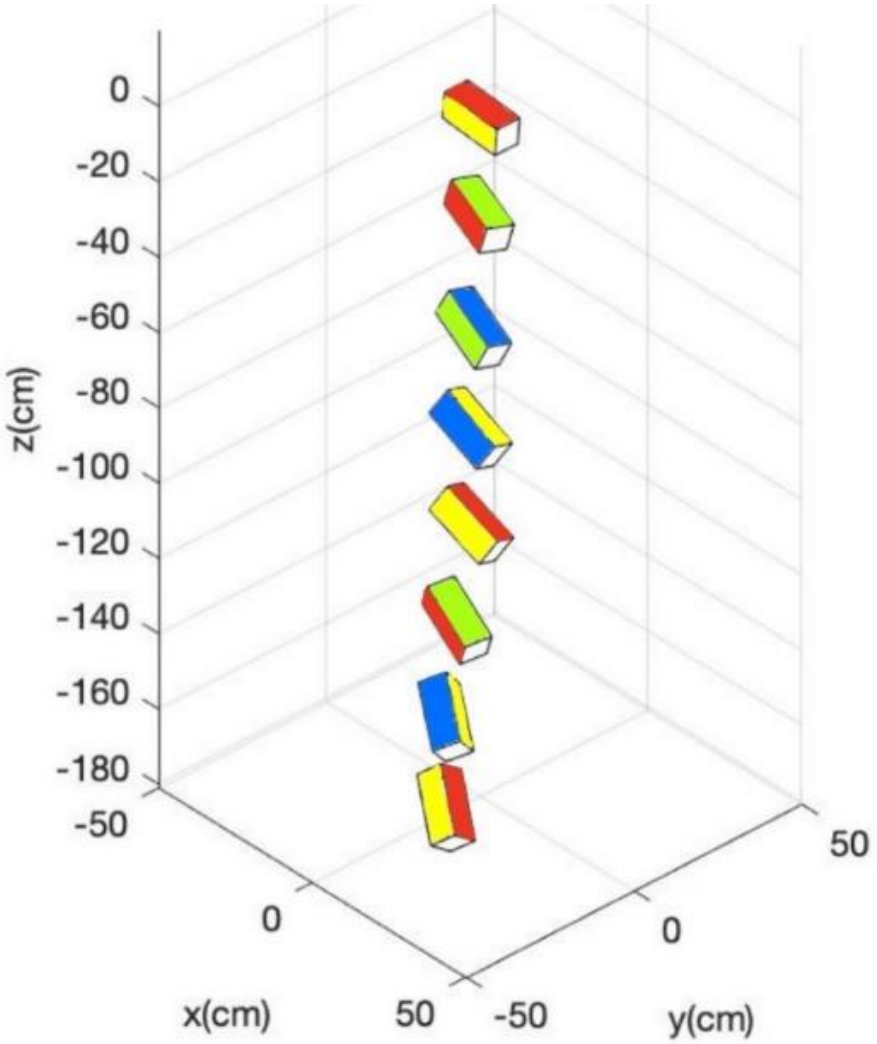

Figure 3.20 Schematic diagram of the falling pattern of dropped container model

Chapter 4: Theories and formulas for cylinders

In this chapter, we derive the 2D and 3D state-space models based on the 2D theory of Aanesland (1987) and the 3D theory of Xiang at al. (2016), respectively, and apply three different statistical methods to obtain the trajectory envelopes.

4.1 Equations of motion (EOM) for dropped cylinders in two-dimensions (2D)

Aanesland (1987) summarized the equations of 2D motion (4.1) – (4.3) suitable for freely falling cylinders in calm water from the model test of dropped drill pipe. This theory simplifies the motion to a two-dimensional one, which involves two coordinate systems. As shown in Figure 4.1, OXZ is a global coordinate system in which the X-axis is fixed on the water surface and points to the right, and the Z-axis is vertically upward. Another coordinate system oxz is the local coordinate system. The origin is fixed at the geometric center of the cylinder, the x-axis is parallel to the length of the cylinder, and the z-axis is perpendicular to the x-axis. β is the angle between two coordinate systems and the angle changes with the position of the cylinder. When the cylinder is placed horizontally on the water surface, $\beta = 0$, $x = z = 0$, and the two coordinate systems coincide. The velocity components of the equations of motion are U_1 (surge), U_3 (heave) and Ω_2 (pitch).

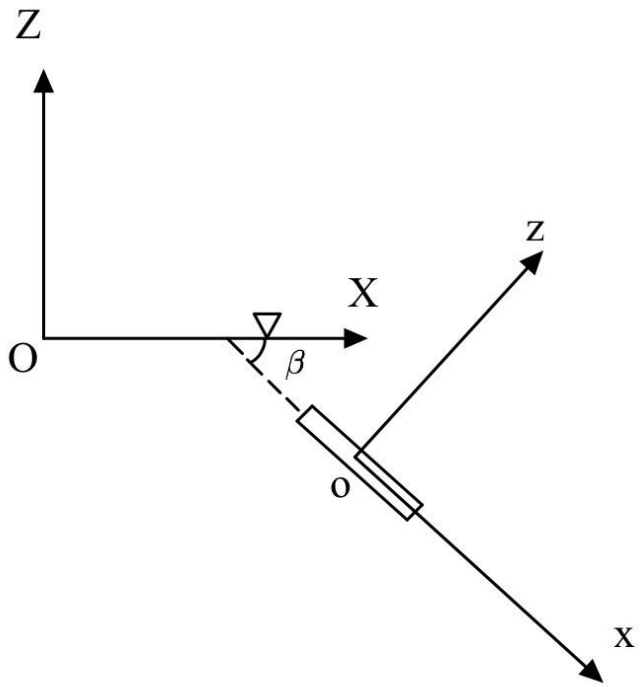

Figure 4.1 The 2D coordinate system

$$(m - \rho\nabla)gsin(\beta) + F_{dx} = m\dot{U}_1 \tag{4.1}$$

$$-(m - \rho\nabla)cos(\beta) + F_{dz} = \{U_1 m_1 U_3 - U_1(x_t m_t)\Omega_2 + m_{33}\dot{U}_3\} + m(\dot{U}_3 - U_1\Omega_2) \tag{4.2}$$

$$M_{dy} = \{-U_1(m_{33} + x_t m_t)U_3 + U_1 {x_t}^2 m_t \Omega_2 + m_{55}\dot{\Omega}_2\} + M_{55}\dot{\Omega}_2 \tag{4.3}$$

In Equations (4.1) – (4.3), the cylinder is assumed to be a slender body with uniform mass distribution, and its center of gravity and geometric center coincide. However, since the slender body theory requires a smooth change of geometry, the effective trailing edge x_t is introduced to explain the abrupt change at the

end of the cylinder. And according to (Newman, 1977), additional force components are considered in the calculation.

The first term in Equation (4.4) represents frictional resistance, which is obtained from the boundary layer theory of turbulence (Schlichting, 1979), and the second term, formal resistance, is estimated by the drag coefficient from (Hoerner, 1965). Equations (4.5) and (4.6) are originally from Morison equation and applied to obtain the force component of the cylinder in the direction of the heave and pitch. And the relative flow viscosity in the z-axis direction, $U_z(x)$, is defined as

$$F_{dx} = -0.664\pi\sqrt{\upsilon\rho^2 L}U_1\sqrt{|U_1|} - \frac{1}{8}\rho\pi C_{dz}D^2U_1|U_1| \tag{4.4}$$

$$F_{dz} = 0.5\int_{-0.5L}^{0.5L}\rho C_{dz}DU_z(x)|U_z(x)|dx \tag{4.5}$$

$$M_{dy} = -0.5\int_{-0.5L}^{0.5L}\rho C_{dz}DxU_z(x)|U_z(x)|dx \tag{4.6}$$

$$U_z(x) = -(U_3 - \Omega_2 x), -0.5L < x < 0.5L \tag{4.7}$$

Substitute (4.7) into (4.5)– (4.6), we obtain

$$F_{dz} = -0.5\rho C_{dz}D\int_{-0.5L}^{0.5L}(U_3 - \Omega_2 x)|U_3 - \Omega_2 x|dx \tag{4.8}$$

$$M_{dy} = 0.5\rho C_{dz}D\int_{-0.5L}^{0.5L}x(U_3 - \Omega_2 x)|U_3 - \Omega_2 x|dx \tag{4.9}$$

where D = diameter of the cylinder; ν = kinematic viscosity of the water; L = length of the cylinder; C_{dx} = drag coefficient along the x-direction; C_{dz} = drag coefficient along the z-direction.

In the numerical simulation, the following relations are used to transform motion in the local coordinate system into motion in the global system:

$$\dot{X} = U_1 cos\beta - U_3 sin\beta \tag{4.10}$$

$$\dot{Y} = U_1 sin\beta - U_3 cos\beta \tag{4.11}$$

where the initial value $[\mathrm{X}_0, \mathrm{Y}_0] = [0, 0]$, $\dot{\beta}$=Ω_2.

Based on Equations (4.1) - (4.9), we derive the 2D state-space model for a freely falling cylinder as follows

$$\dot{x}_k = f_k(x_k) =$$

$$\begin{bmatrix} \frac{1}{m}(m - \rho\nabla)g\sin x_{4,k} - \frac{0.664}{m}\pi\sqrt{\upsilon\rho^2 L}x_{1,k}\sqrt{|x_{1,k}|} - \frac{1}{8m}\rho\pi C_{dx}D^2x_{1,k}|x_{1,k}| \\ \frac{1}{m_{33}+m}\left[-(m - \rho\nabla)g\cos x_{4,k} + F_{dz} - m_t x_{1,k}x_{2,k} + x_t m_t x_{1,k}x_{3,k} + mx_{1,k}x_{3,k}\right] \\ \frac{1}{m_{55}+M_{55}}\left[M_{dy} + (m_{33} + x_t m_t)x_{1,k}x_{2,k} - {x_t}^2 m_t x_{1,k}x_{3,k}\right] \\ \dot{x}_{3,k} \end{bmatrix}$$

$$F_{dz,k}=\begin{cases}\frac{1}{24}\rho C_{dz}DL^3{x_{3,k}}^2+\frac{1}{2}\rho C_{dz}DL{x_{2,k}}^2 & x_{3,k}<0,\frac{x_{2,k}}{x_{3,k}}\geq\frac{L}{2}\\ -\frac{1}{2}\rho C_{dz}D\left(\frac{1}{12}{\mathrm{L}_{3,k}}^2+L{x_{2,k}}^2\right) & x_{3,k}<0,\frac{x_{2,k}}{x_{3,k}}\leq\frac{L}{2}\\ \frac{1}{2}\rho C_{dz}D\left(\frac{1}{12}\frac{{x_{2,k}}^2}{x_{3,k}}+\frac{1}{2}L^2x_{2,k}x_{3,k}\right) & x_{3,k}<0,\frac{x_{2,k}}{x_{3,k}}\in\left(-\frac{L}{2},\frac{L}{2}\right)\\ -\frac{1}{2}\rho C_{dz}D\left(\frac{1}{12}{\mathrm{L}_{3,k}}^2+L{x_{2,k}}^2\right) & x_{3,k}>0,\frac{x_{2,k}}{x_{3,k}}\geq\frac{L}{2}\\ \frac{1}{24}\rho C_{dz}DL^3{x_{3,k}}^2+\frac{1}{2}\rho C_{dz}DL{x_{2,k}}^2 & x_{3,k}>0,\frac{x_{2,k}}{x_{3,k}}\leq\frac{L}{2}\\ -\frac{1}{2}\rho C_{dz}D\left(\frac{2}{3}\frac{{x_{2,k}}^2}{x_{3,k}}+\frac{1}{2}L^2x_{2,k}x_{3,k}\right) & x_{3,k}<0,\frac{x_{2,k}}{x_{3,k}}\in\left(-\frac{L}{2},\frac{L}{2}\right)\\ -\frac{1}{2}\rho C_{dz}DL|x_{2,k}|x_{2,k} & x_{3,k}=0\end{cases}$$

And

$$M_{dy,k}=\begin{cases}\frac{1}{12}\rho C_{dz}DL^3x_{2,k}x_{3,k} & x_{3,k}<0,\frac{x_{2,k}}{x_{3,k}}\geq\frac{L}{2}\\ -\frac{1}{12}\rho C_{dz}DL^3x_{2,k}x_{3,k} & x_{3,k}<0,\frac{x_{2,k}}{x_{3,k}}\leq\frac{L}{2}\\ \frac{1}{2}\rho C_{dz}D\left(\frac{1}{32}L^4{x_{3,k}}^2+\frac{1}{4}L^2{x_{2,k}}^2-\frac{2}{3}\frac{{x_{3,k}}^4}{{x_{2,k}}^2}\right) & x_{3,k}<0,\frac{x_{2,k}}{x_{3,k}}\in\left(-\frac{L}{2},\frac{L}{2}\right)\\ -\frac{1}{12}\rho C_{dz}DL^3x_{2,k}x_{3,k} & x_{3,k}>0,\frac{x_{2,k}}{x_{3,k}}\geq\frac{L}{2}\\ \frac{1}{12}\rho C_{dz}DL^3x_{2,k}x_{3,k} & x_{3,k}>0,\frac{x_{2,k}}{x_{3,k}}\leq\frac{L}{2}\\ -\frac{1}{2}\rho C_{dz}D\left(\frac{1}{32}L^4{x_{3,k}}^2+\frac{1}{4}L^2{x_{2,k}}^2-\frac{2}{3}\frac{{x_{3,k}}^4}{{x_{2,k}}^2}\right) & x_{3,k}>0,\frac{x_{2,k}}{x_{3,k}}\in\left(-\frac{L}{2},\frac{L}{2}\right)\\ 0 & x_{3,k}=0\end{cases}\tag{4.12}$$

where $x_k=\left[x_{1,k},x_{2,k},x_{3,k},x_{4,k}\right]'=\left[U_{1,k},U_{3,k},\Omega_{2,k},\beta_k\right]'$.

In this model, $x_k=[U_{1,k},U_{3,k},\Omega_{2,k},\beta_k]$ represents the state at the k-th time index, and the respective components herein denote the velocity along the x-axis, the velocity along the z-axis, the pitch moment, and the angle between the two coordinate systems.

4.2 Equations of motion (EOM) for dropped cylinders in three-dimensions (3D)

OXYZ in Figure 4.2 is the global coordinate system, where the X-Y plane represents the still-water surface and the Z-axis points vertically upwards. The other coordinate system, *oxyz*, is a cylinder-fixed local coordinate system. Its x-axis is perpendicular to the cylinder axis. The y-axis is oriented binomially, while the z-axis is oriented normally. The origin *o* is in the center of the mass. If the cylinder is placed horizontally on the water's surface at the beginning, the *OXYZ* and *oxyz* coordinate systems coincide. The cylinder is assumed to have a constant rolling frequency during falling.

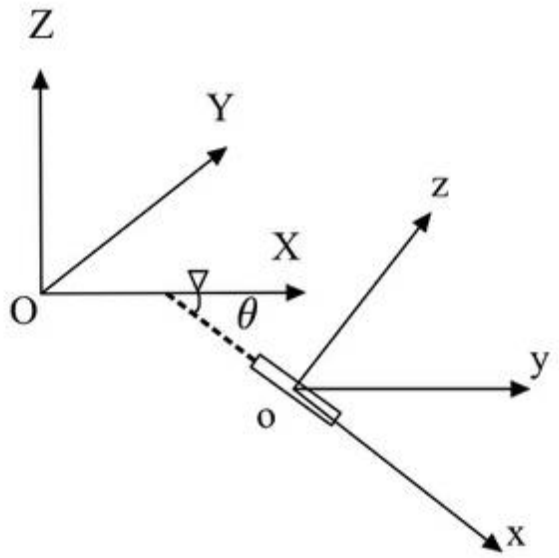

Figure 4.2 The 3D coordinate system

Xiang, Yu et al. (2016b) proposed a new 3D theory for dropped cylinders by extending equations (4.1) – (4.3) based on slender body theory (Newman, 1977):

$$(m-\rho\nabla)gsin(\theta)+F_{dx}=m(\dot{U}_1+U_3\Omega_2+U_2\Omega_3) \tag{4.12}$$

$$-(m-\rho\nabla)gcos(\theta)sin(\phi)+F_{Ly}+F_{dy}=[m_{22}\dot{U}_2+U_1m_{t2}U_2-U_1(x_tm_{t2})\Omega_3]+m\big(\dot{U}_2+U_1\Omega_3-U_3\Omega_1\big) \tag{4.13}$$

$$-(m-\rho\nabla)gcos(\theta)cos(\phi)+F_{Lz}+F_{dz}=[m_{33}\dot{U}_3+U_1m_{t3}U_3-U_1(x_tm_{t3})\Omega_2]+m\big(\dot{U}_3-U_2\Omega_1-U_1\Omega_2\big) \tag{4.14}$$

$$\dot{\Omega}_1=c \tag{4.15}$$

$$M_{Ly}+M_{dy}=[-U_1(m_{33}+x_tm_{t3})U_3+U_1{x_t}^2m_{t3}\Omega_2+m_{55}\dot{\Omega}_2]+M_{55}\dot{\Omega}_2+(M_{44}-M_{66})\Omega_1\Omega_3 \tag{4.16}$$

$$M_{Lz}+M_{dz}=[-U_1(m_{22}+x_tm_{t2})U_2+U_1{x_t}^2m_{t2}\Omega_3+m_{66}\dot{\Omega}_3]+M_{66}\dot{\Omega}_3+(M_{55}-M_{44})\Omega_1\Omega_2 \tag{4.17}$$

The three Euler angles can be expressed by equation (4.18).

$$\begin{bmatrix}\Omega_1\\ \Omega_2\\ \Omega_3\end{bmatrix}=\begin{bmatrix}-\dot{\psi}\sin(\theta)\\ \dot{\psi}\sin(\phi)\cos(\theta)\\ \dot{\psi}\cos(\phi)\cos(\theta)\end{bmatrix}+\begin{bmatrix}0\\ \dot{\theta}\cos(\phi)\\ -\dot{\theta}\sin(\phi)\end{bmatrix}+\begin{bmatrix}\phi\\ 0\\ 0\end{bmatrix} \tag{4.18}$$

The translational motion in the y-direction and rotation around the x- and z-axes are also considered in 3D theory. The Morison equation is used to calculate the transverse drag force F_{dy} and drag moment M_{dz}. Axial roll motion causes transverse lift force, F_{Ly}, and moment, M_{Lz}, as well as vertical lift force, F_{Lz}, and moment, M_{Ly}. For a cylinder in ideal flow (potential theory), Kutta-lift Joukowski's theorem (Glenn Research Center, 1941) is used to estimate F_{Ly}, F_{Lz} and M_{Ly}, M_{Lz}.

$$F_{dx} = -0.664\pi\sqrt{v\rho^2 L}U_1\sqrt{|U_1|} - \frac{1}{8}\rho\pi C_{dz}D^2U_1|U_1| \tag{4.19}$$

$$F_{dy} = 0.5\int_{-0.5L}^{0.5L}\rho C_{dy}DU_y(x)\left|U_y(x)\right|dx \tag{4.20}$$

$$F_{dz} = 0.5\int_{-0.5L}^{0.5L}\rho C_{dz}DU_z(x)|U_z(x)|dx \tag{4.21}$$

$$F_{Ly} = \int_{-0.5L}^{0.5L}\rho U_z(x)\Gamma dx = \int_{-0.5L}^{0.5L}\rho U_z(x)\pi D\Omega_1\frac{D}{2}dx \tag{4.22}$$

$$F_{Lz} = -\int_{-0.5L}^{0.5L}\rho U_y(x)\Gamma dx = -\int_{-0.5L}^{0.5L}\rho U_y(x)\pi D\Omega_1\frac{D}{2}dx \tag{4.23}$$

$$M_{Ly} = \int_{-0.5L}^{0.5L}\rho U_y(x)\Gamma x dx = -\int_{-0.5L}^{0.5L}\rho U_y(x)\pi D\Omega_1\frac{D}{2}dx \tag{4.24}$$

$$M_{Lz} = -\int_{-0.5L}^{0.5L}\rho U_y(x)\Gamma x dx = -\int_{-0.5L}^{0.5L}\rho U_y(x)\pi D\Omega_1\frac{D}{2}dx \tag{4.25}$$

$$M_{dy} = -0.5\int_{-0.5L}^{0.5L}\rho C_{dz}DU_z(x)|U_z(x)|xdx \tag{4.26}$$

$$M_{dz} = 0.5\int_{-0.5L}^{0.5L}\rho C_{dy}DU_y(x)\left|U_y(x)\right|xdx \tag{4.27}$$

Γ is the circulation in equations (4.22) – (4.25). $U_y(x)$ and $U_z(x)$ denotes the y- and z- axis local relative velocity respectively.

$$U_z(x) = -(U_3 - \Omega_2 x), \quad \text{for} -0.5L < x < 0.5L \tag{4.28}$$

$$U_y(x) = -(U_2 - \Omega_3 x), \quad \text{for } -0.5L < x < 0.5L \tag{4.29}$$

Based on the three-dimensional rotation transformation matrix of Euler angles from local to global, the global velocities change of the dropped object during the small-time change can be expressed as equation (4.30):

$$\left[\dot{X}\ \dot{Y}\ \dot{Z}\right] = [U_1\ \ U_2\ U_3]\left\{\begin{bmatrix}1 & 0 & 0\\ 0 & \cos(\phi) & \sin(\phi)\\ 0 & -\sin(\phi) & \cos(\phi)\end{bmatrix}\begin{bmatrix}\cos(\theta) & 0 & -\sin(\theta)\\ 0 & 1 & 0\\ \sin(\theta) & 0 & \cos(\theta)\end{bmatrix}\begin{bmatrix}\cos(\psi) & \sin(\psi) & 0\\ -\sin(\psi) & \cos(\psi) & 0\\ 0 & 0 & 1\end{bmatrix}\right\} \tag{4.30}$$

Similarly, we derive the 3D state-space model for a freely falling cylinder as follows

$$\dot{x}_k = f_k(x_k) =$$

$$\begin{bmatrix}
\frac{1}{m}(m-\rho\nabla)g\sin x_{8,k} - \frac{0.664}{m}\pi\sqrt{v\rho^2 L}x_{1,k}\sqrt{|x_{1,k}|} - \frac{1}{8m}\rho\pi C_{dx}D^2x_{1,k}|x_{1,k}| - x_{3,k}\,x_{5,k} - x_{2,k}\,x_{6,k}\\
\frac{1}{m_{22}+m}[-(m-\rho\nabla)gcos(x_{8,k})\sin(x_{7,k}) + F_{Ly} + F_{dy} - x_{1,k}m_{t2}x_{2,k} + x_{1,k}(x_t m_{t2})x_{6,k} - m(x_{1,k}x_{6,k} - x_{3,k}x_{4,k})]\\
\frac{1}{m_{33}+m}[-(m-\rho\nabla)g\cos(x_{7,k})\cos(x_{8,k}) + F_{Lz} + F_{dz} - x_{1,k}m_{t3}x_{3,k} + x_{1,k}(x_t m_{t3})x_{5,k} - m(x_{2,k}x_{4,k} - x_{1,k}x_{5,k})]\\
\text{c}\\
\frac{1}{m_{55}+M_{55}}[M_{Ly} + M_{dy} + x_{1,k}(m_{33}+x_t m_{t3})x_{3,k} - x_{1,k}{x_t}^2 m_{t3}x_{5,k} - (M_{44}-M_{66})x_{4,k}x_{6,k}]\\
\frac{1}{m_{66}+M_{66}}[M_{Lz} + M_{dz} + x_{1,k}(m_{22}+x_t m_{t2})x_{2,k} - x_{1,k}{x_t}^2 m_{t2}x_{6,k} - (M_{55}-M_{44})x_{4,k}x_{2,k}]\\
x_{4,k} + \frac{x_{5,k}\sin(x_{7,k}) + x_{6,k}\cos(x_{7,k})}{\cos x_{8,k}}\sin(x_{8,k})\\
x_{5,k}\cos(x_{7,k}) - x_{6,k}\sin(x_{7,k})\\
\frac{x_{5,k}\sin(x_{7,k}) + x_{6,k}\cos(x_{7,k})}{\cos x_{8,k}}
\end{bmatrix}$$

$$F_{dy,k}=\begin{cases}-\frac{1}{2}\rho C_{dy}D\left({x_{2,k}}^2L+\frac{1}{12}{x_{6,k}}^2L^3\right) & \frac{x_{2,k}}{x_{6,k}}\geq\frac{L}{2}\\ -\frac{1}{2}\rho C_{dy}D\left(\frac{2}{3}\frac{{x_{2,k}}^2}{x_{6,k}}+\frac{1}{2}L^2x_{2,k}x_{6,k}\right) & \frac{x_{2,k}}{x_{6,k}}\in\left(-\frac{L}{2},\frac{L}{2}\right)\\ \frac{1}{2}\rho C_{dy}D\left({x_{2,k}}^2L+\frac{1}{12}{x_{6,k}}^2L^3\right) & \frac{x_{2,k}}{x_{6,k}}\leq-\frac{L}{2}\\ -\frac{1}{2}\rho C_{dy}DL{x_{2,k}}^2 & x_{6,k}=0\end{cases}$$

$$F_{dz,k}=\begin{cases}-\frac{1}{2}\rho C_{dz}D\left({x_{3,k}}^2L+\frac{1}{12}{x_{5,k}}^2L^3\right) & \frac{x_{3,k}}{x_{5,k}}\geq\frac{L}{2}\\ -\frac{1}{2}\rho C_{dz}D\left(\frac{2}{3}\frac{{x_{3,k}}^2}{x_{5,k}}+\frac{1}{2}L^2x_{3,k}x_{5,k}\right) & \frac{x_{3,k}}{x_{5,k}}\in\left(-\frac{L}{2},\frac{L}{2}\right)\\ \frac{1}{2}\rho C_{dz}D\left({x_{3,k}}^2L+\frac{1}{12}{x_{5,k}}^2L^3\right) & \frac{x_{3,k}}{x_{5,k}}\leq-\frac{L}{2}\\ -\frac{1}{2}\rho C_{dz}DL{x_{3,k}}^2 & x_{5,k}=0\end{cases}$$

$$F_{Ly,k}=-\rho\pi Dx_{4,k}\frac{D}{2}(x_{3,k}L)$$

$$F_{Lz,k}=\rho\pi Dx_{4,k}\frac{D}{2}(x_{2,k}L)$$

$$M_{Ly,k}=\rho\pi Dx_{4,k}\frac{D}{2}(\frac{1}{12}x_{6,k}L^3)$$

$$M_{Lz,k}=-\rho\pi Dx_{4,k}\frac{D}{2}(\frac{1}{12}x_{5,k}L^3)$$

$$M_{dy,k}=\begin{cases}-\frac{1}{12}\rho C_{dz}DL^3x_{3,k}x_{5,k} & \frac{x_{3,k}}{x_{5,k}}\geq\frac{L}{2}\\ -\frac{1}{2}\rho C_{dz}D\left(\frac{1}{32}L^4{x_{5,k}}^2+\frac{1}{4}L^2{x_{3,k}}^2-\frac{2}{3}\frac{{x_{5,k}}^4}{{x_{3,k}}^2}\right) & \frac{x_{3,k}}{x_{5,k}}\in\left(-\frac{L}{2},\frac{L}{2}\right)\\ \frac{1}{12}\rho C_{dz}DL^3x_{3,k}x_{5,k} & \frac{x_{3,k}}{x_{5,k}}\leq-\frac{L}{2}\\ 0 & x_{5,k}=0\end{cases}$$

$$M_{dz,k}=\begin{cases}-\frac{1}{12}\rho C_{dy}DL^3x_{2,k}x_{6,k} & \frac{x_{2,k}}{x_{6,k}}\geq\frac{L}{2}\\ -\frac{1}{2}\rho C_{dy}D\left(\frac{1}{32}L^4{x_{6,k}}^2+\frac{1}{4}L^2{x_{2,k}}^2-\frac{2}{3}\frac{{x_{6,k}}^4}{{x_{2,k}}^2}\right) & \frac{x_{2,k}}{x_{6,k}}\in\left(-\frac{L}{2},\frac{L}{2}\right)\\ \frac{1}{12}\rho C_{dy}DL^3x_{2,k}x_{6,k} & \frac{x_{2,k}}{x_{6,k}}\leq-\frac{L}{2}\\ 0 & x_{6,k}=0\end{cases}\qquad(4.31)$$

where,

$$x_k=\left[x_{1,k},x_{2,k},x_{3,k},x_{4,k},x_{5,k},x_{6,k},x_{7,k},x_{8,k},x_{9,k}\right]'=\left[U_{1,k},U_{2,k},U_{3,k}\Omega_{1,k},\Omega_{2,k},\Omega_{3,k},\phi_k,\theta_k,\psi_k\right]'$$

4.3 Comparison of dropped cylinders using 2D model and 3D model

For the heave-pitch coupling term on the X-Y plane, $\boldsymbol{U_3 \times \Omega_2}$, Aanesland 's two-dimensional theory does not have this term, but this term exists in Xiang at al. (2016)'s 3D theory. It's actually a higher-order item of the two-dimensional theory. When I degenerate the three-dimensional theory into two dimensions, this item is retained in the two-dimensional theory, and it has a significant change in the results as shown in Figure 4.3, but the original author did not discuss this coupling term separately, so I show the effect of this term on the system.

The heave-pitch coupling term $\boldsymbol{U_3 \times \Omega_2}$ on the X-Y plane is a higher-order term of the two-dimensional theory. This term is ignored in Aanesland's 2D theory but retained in Xiang's 3D theory. But the original author did not discuss this coupling item separately, so I show the effect of this item on the system here. I degenerate the three-dimensional theory into two-dimensional, that is, set the parameters on the non-X-Y plane to 0, and then compare the 3D trajectory with the term, the 3D trajectory without the item, and the 2D trajectory, and the result is shown in Figure 4.3, This term has a significant impact on the trajectory. After removing the two-dimensional coupling term, the 3D result is completely consistent with the 2D result, which further verifies the correctness of the theory. Compared with the 3D results without this term, the presence of this term makes the fall trajectory smoother and completely within the experimental trajectory envelope.

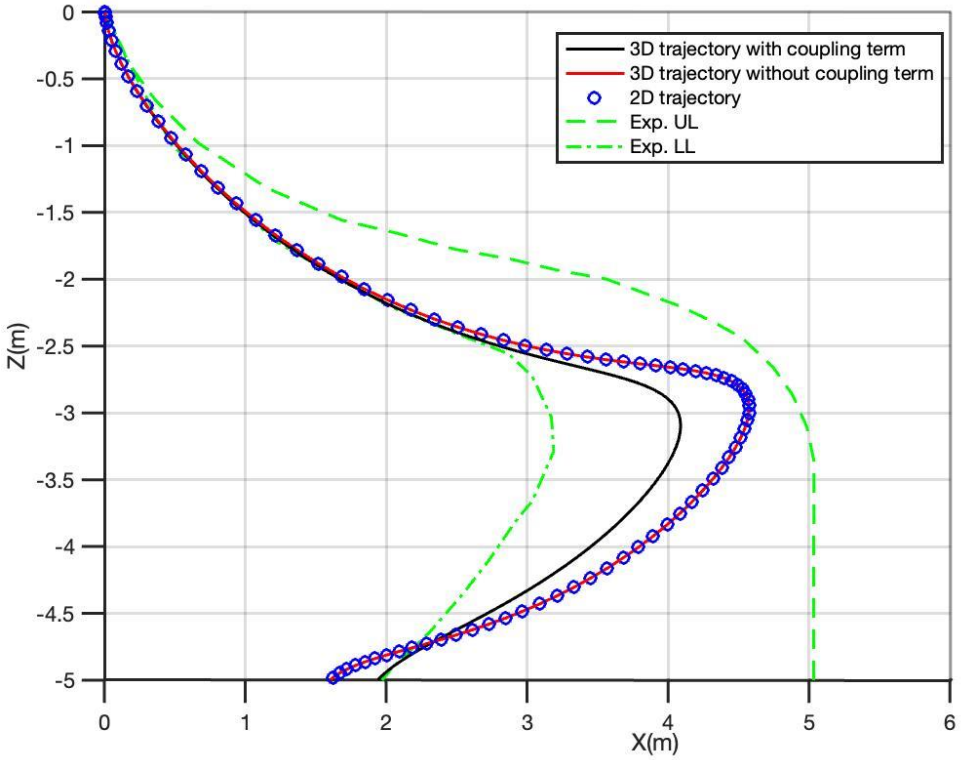

Figure 4.3 Comparison of trajectories of dropped cylinders using 2D model and 3D model at drop angle 45°

4.4 Statistical methods to calculate the trajectory envelope

In previous studies, all numerical predictions about dropped cylinders turned out to be deterministic trajectories, but in experiments, the distribution of landing points for dropped cylinders appeared to be random. We propose a 3D trajectory envelope as a practical solution that uses three probabilistic approaches based on 3D theory-based state-space models, instead of only deterministic trajectories as before. On the one hand, as the most common random sampling method, the Monte Carlo (MC) method is used to calculate the statistical analysis of the corresponding trajectories of the cylinder under different dropped angle conditions. On the other hand, the well-known trajectory tracking algorithms in electrical engineering, the unscented method, and the cubature method, are both adopted because they have better results than similar methods when dealing with problems.

4.4.1 Statistical methods

This section gives an introduction of the three statistical methods in subsequent section of this dissertation. The exposition of the methods is based on Julier and Uhlmann (1997), Durrant-Whyte (2000), Arasaratnam and Haykin, (2009).

4.4.1.1 Monte Carlo method

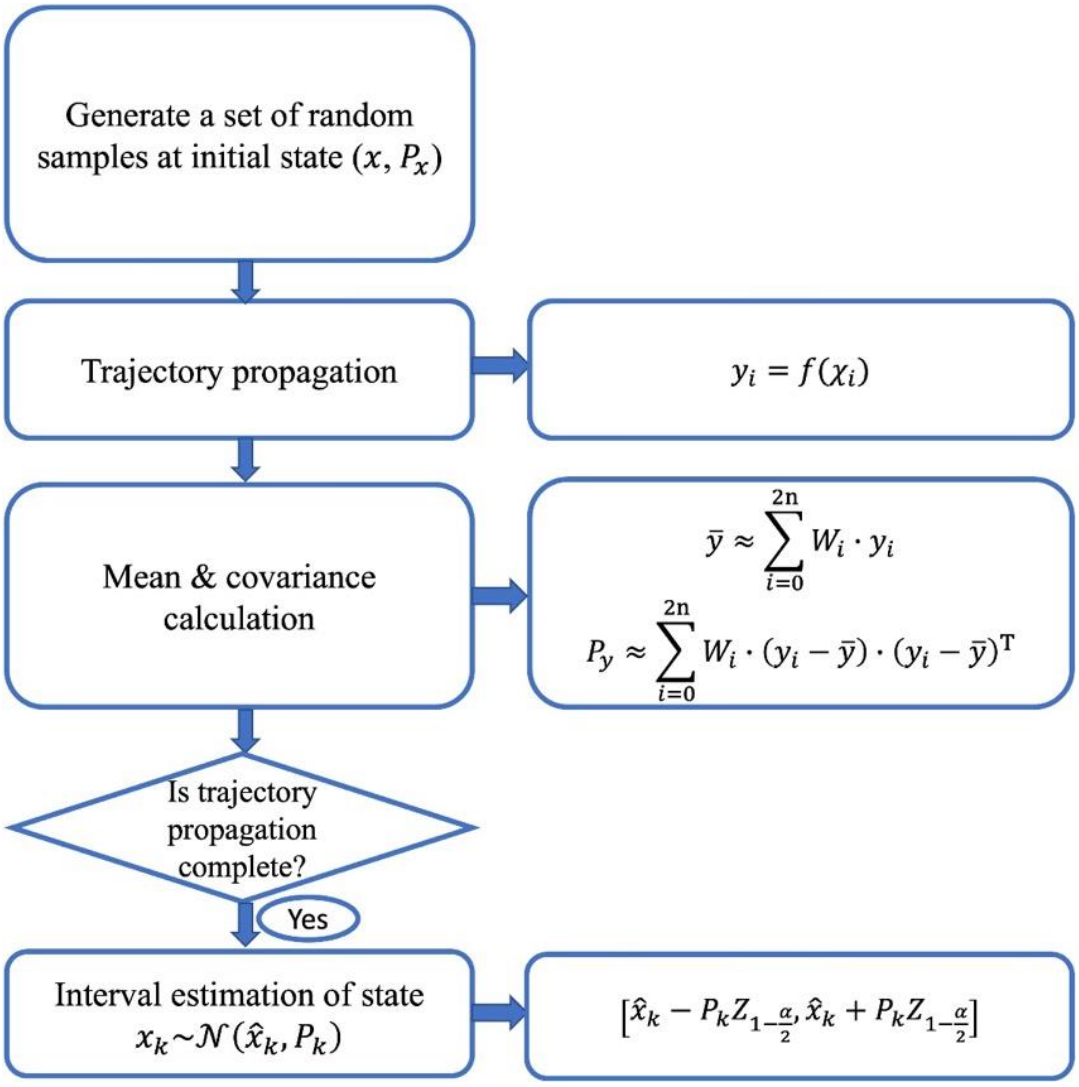

Figure 4.4 Flowchart of MC method

The MC method is reliable under the premise of sufficiently large samples. The flowchart of the MC method in this dissertation is shown in Figure 4.4. According to the actual data detected in the drop experiment, this dissertation demonstrates a fluctuation at the initial state of the falling object, and the fluctuation is modeled to be a Gaussian distribution. Therefore, we add Gaussian perturbations to the surge, sway, pitch, and the initial angle in the initial state x_0. Their variances are

$$P_0 = \left[10^{-4}\ m^2/s^2, 10^{-4}\ m^2/s^2, \left(\frac{\pi}{90}\right)^2\ rad^2/s^2, \left(\frac{\pi}{90}\right)^2\ rad^2\right] \tag{4.32}$$

Correspondingly, for the state of the 3D theory at each moment:

$$x_k = [U_{1,k,}U_{2,k}, U_{3,k}\Omega_{1,k}, \Omega_{2,k}, \Omega_{3,k}, \phi_k, \theta_k, \psi_k]$$

The corresponding random disturbance variance is:

$$P_{\mathrm{k}} = \left[10^{-4}\frac{m^2}{s^2}, 10^{-4}\frac{m^2}{s^2}, 10^{-4}\frac{m^2}{s^2}, 10^{-4}\frac{m^2}{s^2}, \left(\frac{\pi}{90}\right)^2\frac{rad^2}{s^2}, \left(\frac{\pi}{90}\right)^2\frac{rad^2}{s^2}, \left(\frac{\pi}{90}\right)^2\frac{rad^2}{s^2}, \left(\frac{\pi}{90}\right)^2\ rad^2, \left(\frac{\pi}{90}\right)^2\ rad^2, \left(\frac{\pi}{90}\right)^2\ rad^2, \right]$$

All subsequent methods uniformly use the above variance for estimation.

Since the initial state of the problem is described by four terms, when the MC method is performed, the number of simulations is set to be a power of 4, such as 2^4, 3^4… To obtain the mean $\bar{y}$ and variance P_{y}, Equation (4.33) is imported in the simulation results at every time steps, and for each time step, we have the equal Monte Carlo weight.

$$\begin{cases} \bar{y} = \frac{1}{n}\sum_{i=1}^{n} y_i \\ P_{\mathrm{y}} = \frac{1}{n}\sum_{i=1}^{n}(\bar{y} - y_i)^2 \end{cases} \tag{4.33}$$

According to the mean $\bar{y}$ and variance P_{y}, we can obtain an estimated interval based on Gaussian distribution $\mathcal{N}(\bar{y}, P_{\mathrm{y}})$, which is described in detail in the subsequent subsection.

4.4.1.2 Unscented method

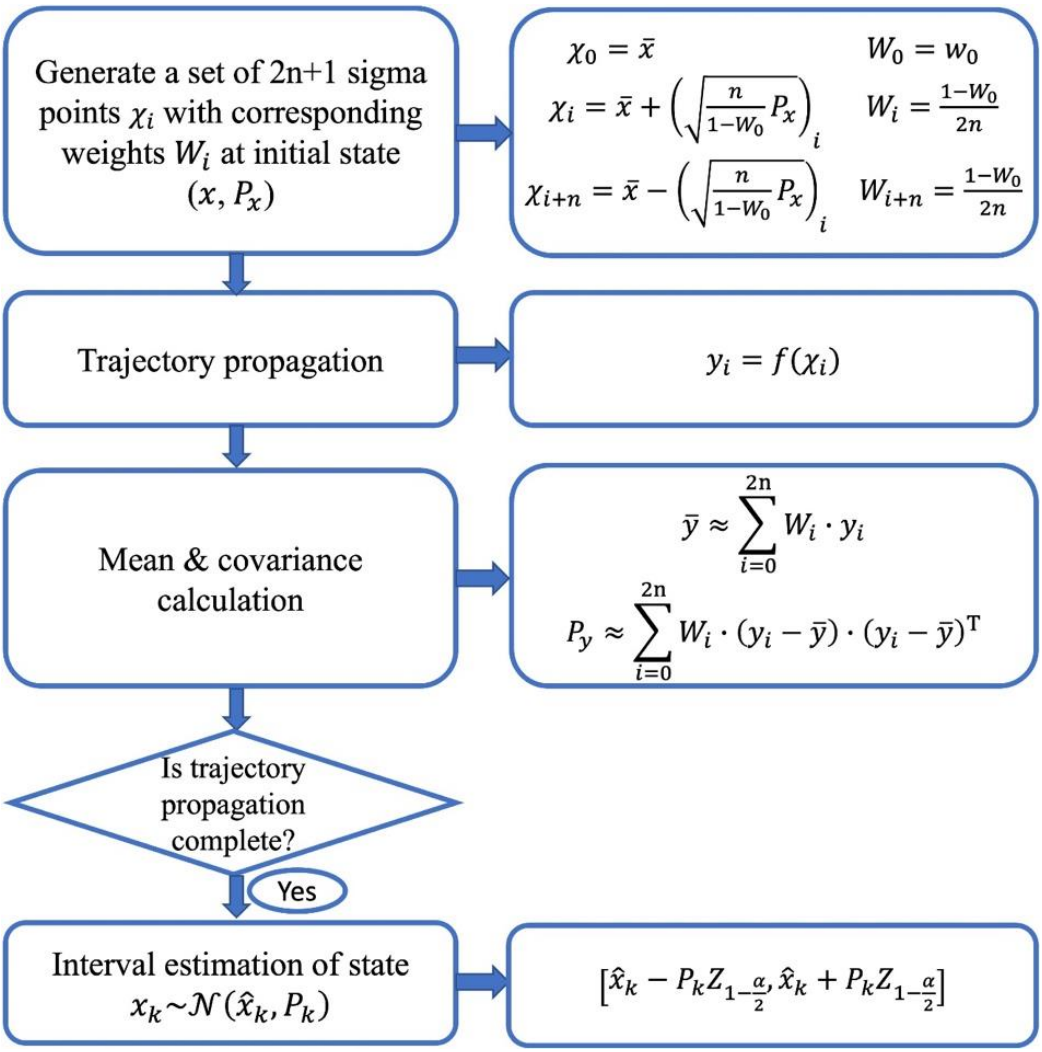

Figure 4.5 Flowchart of unscented method

The unscented method is a data processing algorithm that uses a deterministic sampling strategy to approximate the distribution sought-after proposed by Julier and Uhlman (1997). Its process is shown in Figure 4.5. As a newly developed method, the state distribution of the unscented method is usually represented by Gaussian random distributions. However, the specific sampling form is deterministic sampling, not random sampling like the MC method. Compared with the MC method, which requires thousands of sample points to obtain accurate results, the unscented method can obtain comparably accurate results by only using dozens of deterministic sample points. The sample points of the unscented method are called the Sigma points. In general, the number of the Sigma points of a random variable x with dimension n is $2n + 1$, the true mean and the $2n$ symmetrically distributed sample points around the true mean. When propagating through a nonlinear system, the unscented method captures the posterior mean and covariance to obtain accurate results.

Specifically, in the nonlinear transformation, $y = f(x)$ with the n-dimensional random input $x \sim (\bar{x}, P_x)$, the generation of a set of $2n + 1$ Sigma points $\mathcal{X}_i$ with the corresponding weights W_i is as follows:

$$\begin{cases} \mathcal{X}_0 = \bar{x} & W_0 = w_0 \\ \mathcal{X}_i = \bar{x} + \left(\sqrt{\frac{n}{1-W_0}P_x}\right)_i & W_i = \frac{1-W_0}{2n} \\ \mathcal{X}_{i+n} = \bar{x} - \left(\sqrt{\frac{n}{1-W_0}P_x}\right)_i & W_{i+n} = \frac{1-W_0}{2n} \end{cases} \tag{4.34}$$

where $\mathcal{X}_0$ is the mean of the above 2n+1 values, $\mathcal{X}_i$ and $\mathcal{X}_{i+n}$ are symmetrical about $\mathcal{X}_0$, $i = 1, 2, \dots, n$. w_0 is the weight on the mean point determined by the situation, in this case, it is set to 1/3, the remaining weights are equally distributed. The operator $\sqrt{\cdot}$ is the Cholesky decomposition, which can be seen as taking the square root of the matrix, and $(\sqrt{\cdot})_i$ represents the ith row of the decomposition matrix. $\sqrt{\frac{n}{1-W_0}}$ is scaled to retain the original mean and covariance when the non-linear transformation degenerates to a linear one. By propagating $y = f(x)$ in the Sigma point set$\{\mathcal{X}_i\}$, the transformed Sigma point set $\{\mathcal{Y}_i\}$:

$$\mathcal{X}_{i,k|k-1} = f(\mathcal{X}_{i,k-1|k-1}) \tag{4.35}$$

Accordingly, the mean $\bar{x}_{k|k-1}$, and covariance $P_{k|k-1}$ are approximated by

$$\begin{cases} \bar{x}_{k|k-1} \approx \sum_{i=1}^{2n} W_i \cdot \mathcal{X}_{i,k|k-1} \\ P_{k|k-1} \approx \sum_{i=1}^{2n} W_i \cdot (\mathcal{X}_{i,k|k-1} \cdot \mathcal{X}^T{}_{i,k|k-1} - \bar{x}_{k|k-1} \cdot \bar{x}^T{}_{k|k-1} + Q_{k-1}) \end{cases} \tag{4.36}$$

where $\bar{x}_{k|k-1}$and $P_{k|k-1}$ are also the estimated mean value and variance in the next time step. It is worth noting that $\bar{x}_{k|k-1}$ is not the $\mathcal{X}_{i,k-1|k-1}$ at the beginning in the next time step. The new Sigma points $\mathcal{X}_{i,k-1|k-1}$ with corresponding weights W_i should be reselected according to Equation (4.34).

4.4.1.3 Cubature method

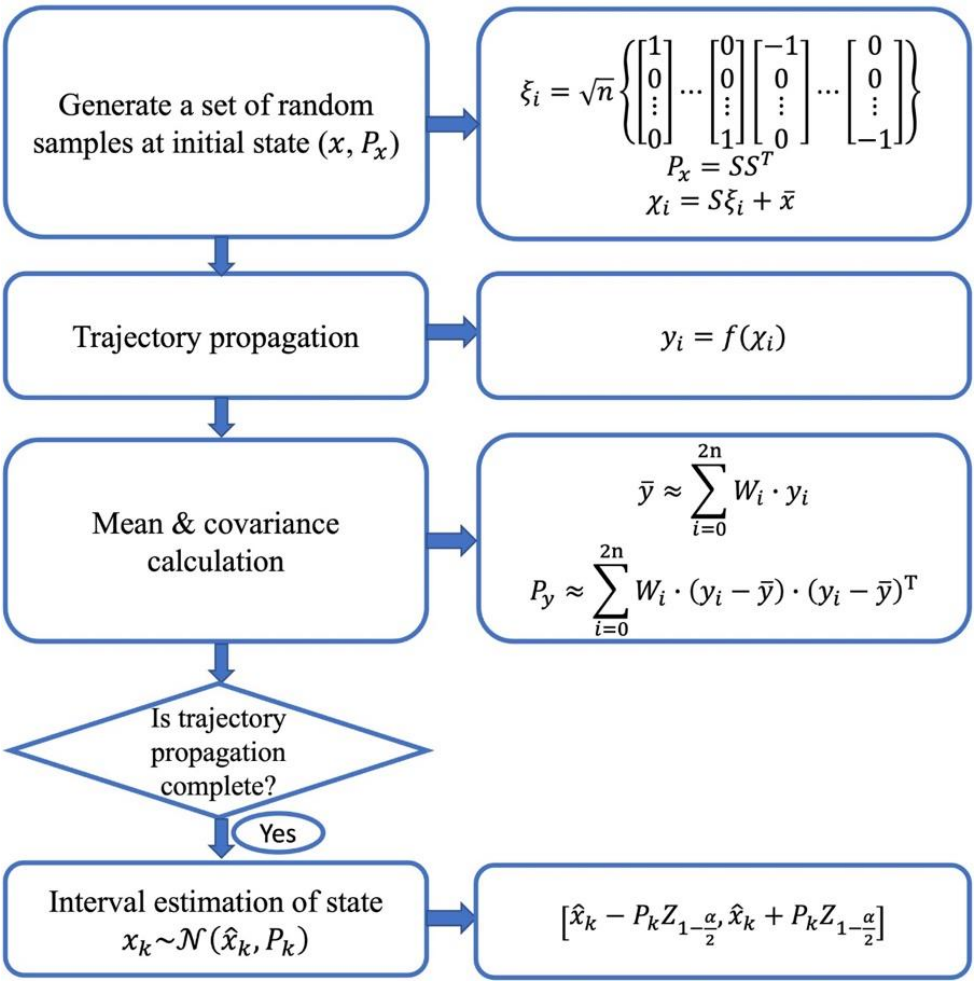

Figure 4.6 Flowchart of Cubature method

The Cubature method is another effective method for high-dimensional state estimation. Figure 4.6 depicts the flowchart of the Cubature method used in this dissertation. As the heart of the Cubature method, a third-degree spherical radial Cubature rule developed by Arasaratnam and Haykin (2009) yields a collection of symmetric Cubature points that scale linearly with the state dimension. That is, the Cubature method and the unscented method have similar algorithm structures but are based on entirely different strategies for sample points and weight distribution.

The spherical-radial transformation, as the name suggests, is to transform a variable from the Cartesian coordinate system to the spherical-radius coordinate system. Define an integral in the Cartesian coordinate

$$I(f) = \int_{\mathbb{R}^n} f(x) exp(-x^T x) dx \quad x \in \mathbb{R}^n \tag{4.37}$$

Set $x = ry$ with $y^T y = 1$, then, the integral (4.37) is represented in a spherical-radial coordinate system as

$$I(f) = \int_0^{\infty} \int_{U_n} h(ry) r^{n-1} exp(-r^2) d\sigma(y) dr \qquad y \in \mathbb{R}^n \ \ and \ r \in [0, \infty) \tag{4.38}$$

where U_n is the surface of the sphere as specified by $U_n = \{y \in \mathbb{R}^n | y^T y = 1\}$ and $\sigma(\cdot)$ is the spherical area element on U_n.

Apply the third-degree spherical-radial rule to Equation (4.38), the standard Gaussian weighted integral can be computed in the Cartesian coordinate as follow:

$$I(f) = \sum_{i=1}^{2n} W_i f(\xi_i) \tag{4.39}$$

where n is the dimension of the variable x_i, W_i is its weight and

$$\xi_i = \sqrt{n}\left\{\begin{bmatrix}1\\0\\\vdots\\0\end{bmatrix}\cdots\begin{bmatrix}0\\0\\\vdots\\1\end{bmatrix}\begin{bmatrix}-1\\0\\\vdots\\0\end{bmatrix}\cdots\begin{bmatrix}0\\0\\\vdots\\-1\end{bmatrix}\right\}$$

According to the Cubature rule, the set of points are fully symmetric with the same weight value, we have

$$W_i = \frac{1}{2n}\ i = 1,2,\ldots,2n$$

Consider the random variable x with mean $\bar{x}$, and covariance is P, we first factorize $P_{k-1|k-1}$:

$$P_{k-1|k-1} = S_{k-1|k-1} S^T{}_{k-1|k-1} \tag{4.40}$$

The Cubature points $\mathcal{X}_{i,k-1|k-1_i}$ (Similar as the Sigma points in the unscented method) with the corresponding weights W_i can be evaluated by the spherical-radial transformation:

$$\begin{cases}\mathcal{X}_{i,k-1|k-1} = S_{k-1|k-1}\xi_i + \bar{x}_{,k-1|k-1}\\ W_i = \frac{1}{2n}\end{cases} \tag{4.41}$$

Propagate the Cubature points:

$$\mathcal{X}_{i,k|k-1} = h(\mathcal{X}_{i,k-1|k-1}) \tag{4.42}$$

The mean $\bar{x}_{k|k-1}$, and covariance $P_{k|k-1}$ are estimated:

$$\begin{cases}\bar{x}_{k|k-1} \approx \sum_{i=1}^{2n} W_i \cdot \mathcal{X}_{i,k|k-1}\\ P_{k|k-1} \approx \sum_{i=1}^{2n} W_i \cdot (\mathcal{X}_{i,k|k-1} \cdot \mathcal{X}^T{}_{i,k|k-1} - \bar{x}_{k|k-1} \cdot \bar{x}^T{}_{k|k-1} + Q_{k-1})\end{cases} \tag{4.43}$$

where Q is the error covariance matrix

It is not difficult to see that the unscented method and the Cubature method are similar in structure. They both generate a set of weighted points through the initial mean and variance and propagate these points to estimate the position of the points at the next step. However, the unscented method needs to artificially set the w_0 value of the initial mean (4.34), which significantly impacts the generation of points later. The prediction result's numerical accuracy is significantly related to the appropriateness of w_0 (Arasaratnam and Haykin, 2009). In the following case study, to get more accurate results compared with the other two methods, the weight w_0 of the unscented method is pre-tuned according to the ideal true (trajectory without noise). In contrast, people usually emphasize the Cubature rule, having preferred numerical quality criterion over efficiency (Arasaratnam and Haykin, 2009). As a completely automatic numerical algorithm, the state estimation of the Cubature method only depends on the initial mean and variance, with no need to carefully select the initial weights. Under the premise of consistent prediction results, the Cubature method does not need to be tuned, making itself easier and more suitable on operation, especially for real-time risk assessment.

4.4.1.4 Square-root Cubature method

The two basic properties of an error covariance matrix are i) symmetry and ii) positive definiteness. It is important that we preserve these two properties in each update cycle. The reason is that the use of a forced

symmetry on the solution of the matrix Ricatti equation improves the numerical stability of the Kalman filter, whereas the underlying meaning of the covariance is embedded in the positive definiteness. In practice, due to errors introduced by arithmetic operations performed on finite word-length digital computers, these two properties are often lost. Specifically, the loss of the positive definiteness may probably be more hazardous as it stops the Kalman filter to run continuously.

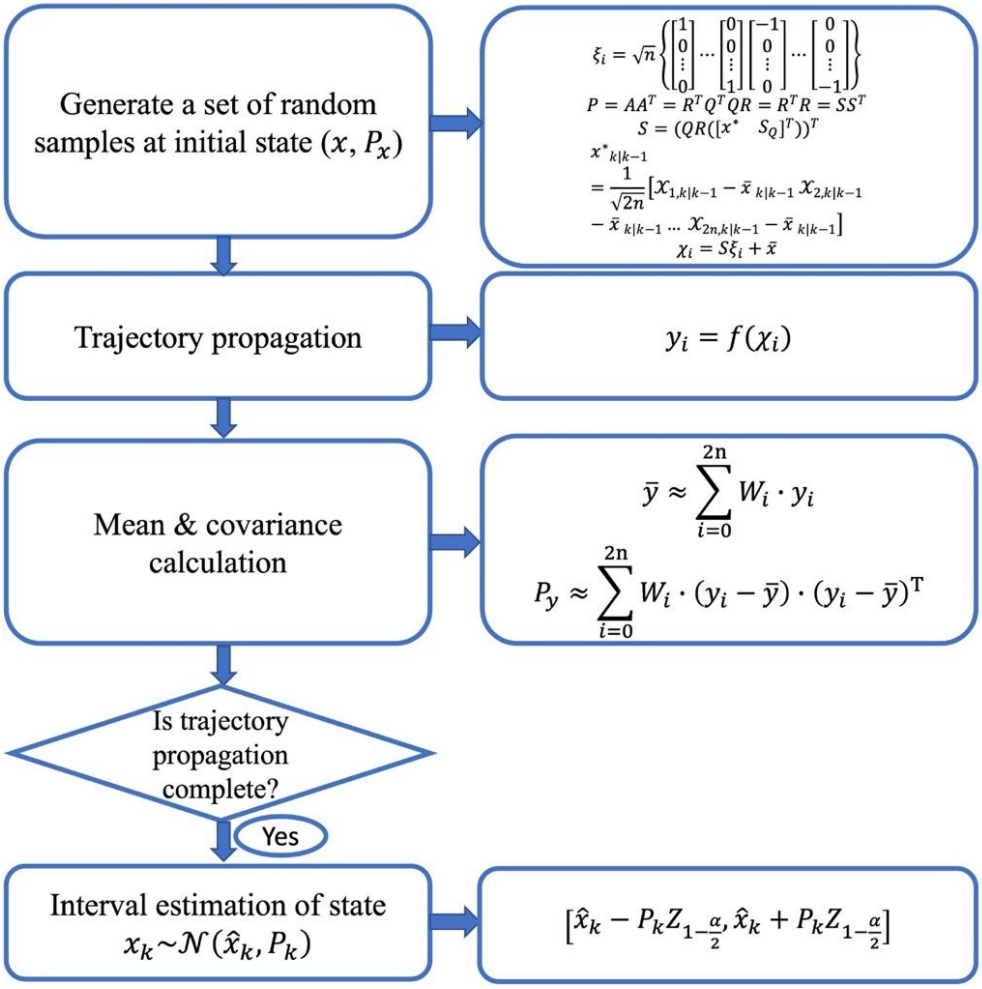

Figure 4.7 Flowchart of square-root Cubature method

A square-root version of the Cubature method is derived for improving the numerical stability. Instead of factorizing covariance P only, a general triangularization algorithm, QR decomposition, is denoted as $S = QR(A)$, then,

$$P = AA^T = R^TQ^TQR = R^TR = SS^T \tag{4.44}$$

Compute $\bar{x}$ and P from Equation 4.43 as above, then estimate the predicted error covariance:

$$P_{k|k-1} = S_{k|k-1}{S_{k|k-1}}^T \tag{4.45}$$

where $S_{k|k-1} = (QR([{x^*}_{k|k-1} \quad S_{k|k-1}]^T))^T$ is a lower triangular matrix, S_Q denotes a square-root factor of Q, and

$${x^*}_{k|k-1} = \frac{1}{\sqrt{2n}}[\mathcal{X}_{1,k|k-1} - \bar{x}_{k|k-1}\ \mathcal{X}_{2,k|k-1} - \bar{x}_{k|k-1} \dots \mathcal{X}_{2n,k|k-1} - \bar{x}_{k|k-1}] \tag{4.46}$$

Unfortunately, it may be impossible for us to formulate the square-root unscented method that enjoys numerical advantages like the square-root Cubature method. Because the unscented method -computed covariance matrix is not always guaranteed to be positive definite. Hence, the unavailability of the square-root covariance causes the unscented method to halt its operation (Arasaratnam and Haykin, 2009). In this study, the flowchart for square-root Cubature method is clearly shown in Figure 4.7.

4.4.2 Improvement by feedback

In the estimation of the two-dimensional trajectory, the measurement-update module was not added to the simulation because the simulation results were good enough. However, because the 3D model is more complex then 2D, the simulation results obtained by using the previous filter are not expectable. Therefore, the measurement-update module is added in the simulation process to improve the accuracy of the 3D estimation results.

Consider that the state x_k at time *k* is obtained from the filters above, the measurement equation is described as:

$$z_k = h(x_k) + v_k \tag{4.47}$$

where z_k is the observation and h is the measurement function. The measurement noise $v_k's$ is assumed to be white Gaussian with zero mean.

Instantiate each of the prediction points through the observation model:

$$\mathcal{Z}_{i,k|k-1} = h(\mathcal{X}_{i,k|k-1}) + v_k \qquad i = 1,2,\dots,2n \tag{4.48}$$

The predicted observation is calculated by

$$\bar{z}_{k|k-1} = \sum_{i=1}^{2n} W_i \cdot \mathcal{Z}_{i,k|k-1} \tag{4.49}$$

and the measurement-update equations are

$$P_{\bar{z}\bar{z},k|k-1} = \sum_{i=1}^{2n} W_i \cdot \left(\mathcal{Z}_{i,k|k-1} - \bar{z}_{k|k-1}\right) \cdot \left(\mathcal{Z}_{i,k|k-1} - \bar{z}_{i,k|k-1}\right)^{\mathrm{T}} + R_k \tag{4.50}$$

$$P_{\bar{x}\bar{z},k|k-1} = \sum_{i=1}^{2n} W_i \cdot \left(\mathcal{X}_{i,k|k-1} - \bar{x}_{k|k-1}\right) \cdot \left(\mathcal{Z}_{i,k|k-1} - \bar{z}_{i,k|k-1}\right)^{\mathrm{T}} \tag{4.51}$$

$$\mathcal{K}_k = P_{\bar{z}\bar{z},k|k-1} \cdot P^{-1}{}_{\bar{x}\bar{z},k|k-1} \tag{4.52}$$

$$\begin{cases} \bar{x}_{k|k} = \bar{x}_{k|k-1} + \mathcal{K}_k\left(\mathcal{Z}_k - \bar{z}_{k|k-1}\right) \\ P_{k|k} = P_{k|k-1} - \mathcal{K}_k P_{\bar{z}\bar{z},k|k-1} {\mathcal{K}_k}^T \end{cases} \tag{4.53}$$

where $\bar{x}_{k|k-1}$ and $P_{k|k-1}$ are the old mean and covariance from the filters above, $\bar{x}_{k|k}$, and $P_{k|k}$ are the updated mean and covariance.

4.4.3 Interval estimation

Since the trajectories of dropped objects in water is affected by many uncontrollable factors, it is impossible to obtain two entirely same trajectories by repeatedly dropping the cylinder with small disturbances in the experiment. Calculating an exact trajectory from the statistical methods and then using this trajectory as the solution to this problem is not realistic. The problem of dropped objects is not deterministic. For this reason, this dissertation expands the calculation results based on the mean and variance obtained by the probabilistic methods and tries to estimate the interval instead of a definite trajectory as the solution to this problem.

The estimated state $x_k \sim \mathcal{N}(\hat{x}_k, P_k)$ assumed to follow the Gaussian distribution (DNV, 2010) is obtained from the three statistical methods discussed about.

The confidence interval of each element of the state is

$$\left[\hat{x}_{i,k} - P_{ii,k} Z_{1-\frac{\alpha}{2}}, \hat{x}_{i,k} + P_{ii,k} Z_{1-\frac{\alpha}{2}}\right] \tag{4.54}$$

where $\hat{x}_{i,k}$ represent the i-th element of the estimation state x_k and $P_{ii,k}$ is the i-th diagonal element of the error covariance P_k. $Z_{1-\frac{\alpha}{2}}$ is obtained by the two-tail table of Gaussian distribution based on the confidence coefficient α.

After estimated the value of $\hat{x}_{i,k}$ and $P_{ii,k}$ at each time step *k* through the statistical methods, the envelope of the trajectory prediction can be obtained by substituting the values (4.31) into the coordinate transformation (4.30).

Chapter 5: Case Study II – Cylindrical objects

As described in Chapter 1, Aanesland (1987) conducted a series of drop tests to study the drop process of drill pipes from the platform deck to the seabed. Further, he concluded six drop patterns of drill pipes based on these tests. DNV has adopted these patterns and included them in the Recommended Practice (DNV, 2010). In this chapter, we apply the 3D state-space model that is derived in Chapter 4 to calculate the trajectory envelopes, and further compare them with the experimental results.

5.1 Properties of dropped pipes

Table 5.1 shows the properties of the drilling pipes (Aanesland,1987). In our numerical study, they are assumed to freely fall down from the calm water surface to 5m-deep tank bed.

Table 5.1 Properties of scaled dropped cylinders

Parameters	Unit	Full Scale	Model Scale (1:20.32)
Length (L)	m	9.95	0.45
Mass density (ρ_c)	kg/m	225	0.548
Diameter (D)	m	0.203	0.01

5.2 Simulated results of dropped cylindrical objects using 2D theory

5.2.1 Force components at drop angle 30°

For the numerical results of the cylinder model, firstly, the force component in the x direction consists of two parts, the frictional drag (F_{dx1}) and the form drag (F_{dx2}). As shown in Figure 5.1, 5.4 and 5.7, the form drag dominates initially but decays rapidly over time. The transient part almost vanishes after 17s around, and the steady-state part becomes obvious. In the steady state, the frictional drag is still smaller than the form drag, which means that the form drag F_{dx2} is the main component in this example.

The calculation of the force F_{dz} in the z direction is based on the Morison equation. Only the drag term is retained here. The magnitude of F_{dz} rises sharply after entering the water, and it becomes periodic after two cycles. In Figures 5.2 and 5.3, Figures 5.5 and 5.6, Figures 5.8 and 5.9, the pitch moment M_{dy} shows a very similar pattern with F_{dz} at drop angle 30°, 45°, 60°indicated by equations (5) and (6).

It should be noted that in our current discussion, we have ignored the impact of water-entry.

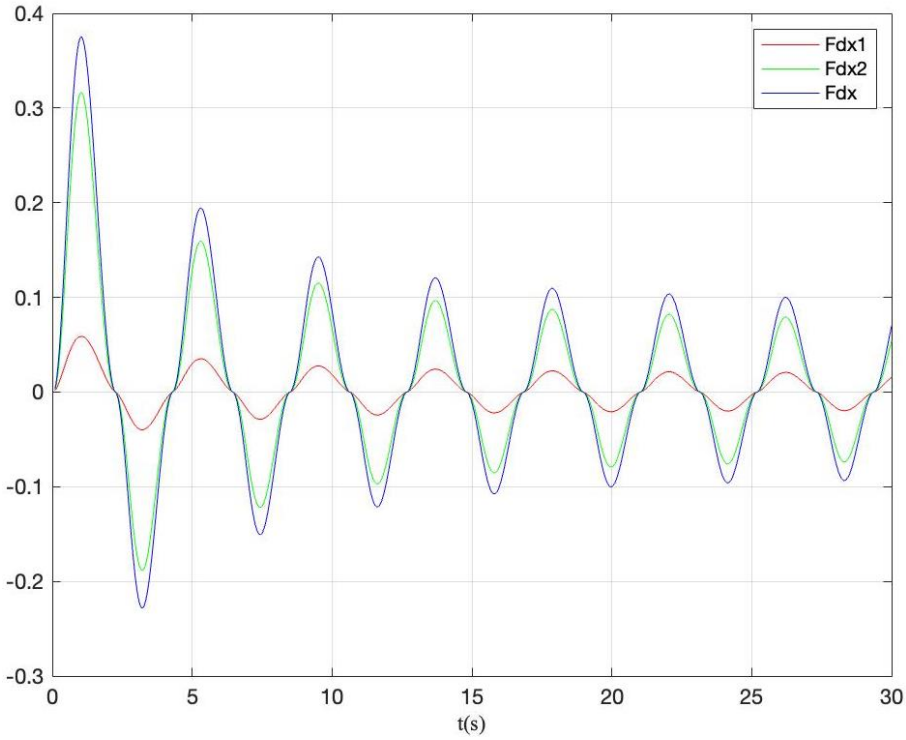

Figure 5.1 Surge force at drop angle 30°

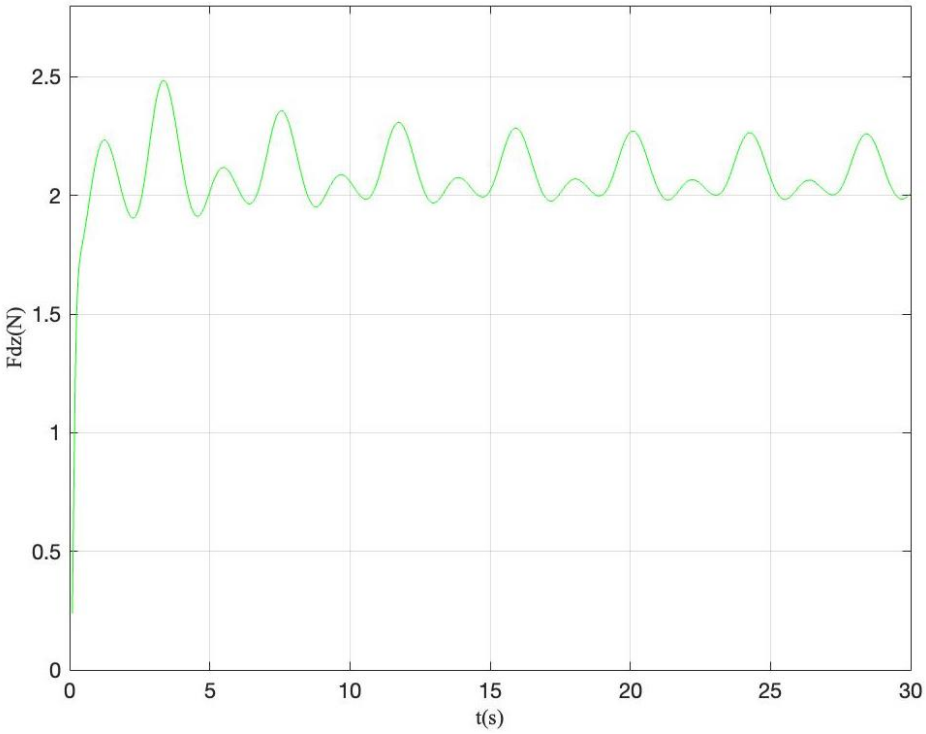

Figure 5.2 Heave force at the drop angle 30°

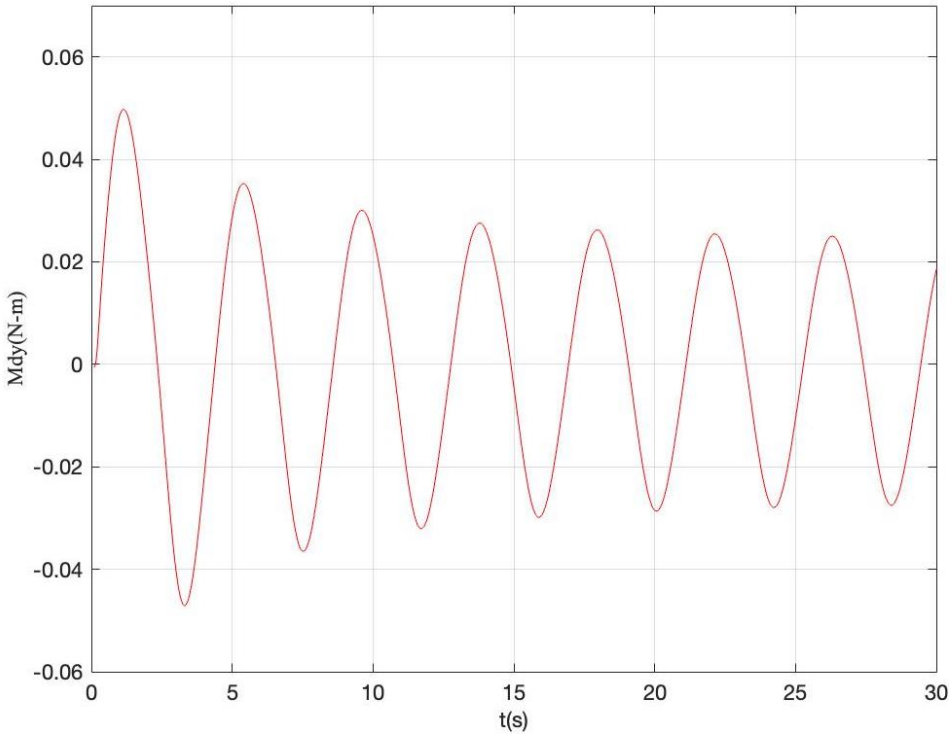

Figure 5.3 Pitch moment at the drop angle 30°

5.2.2 Force components at drop angle 45°

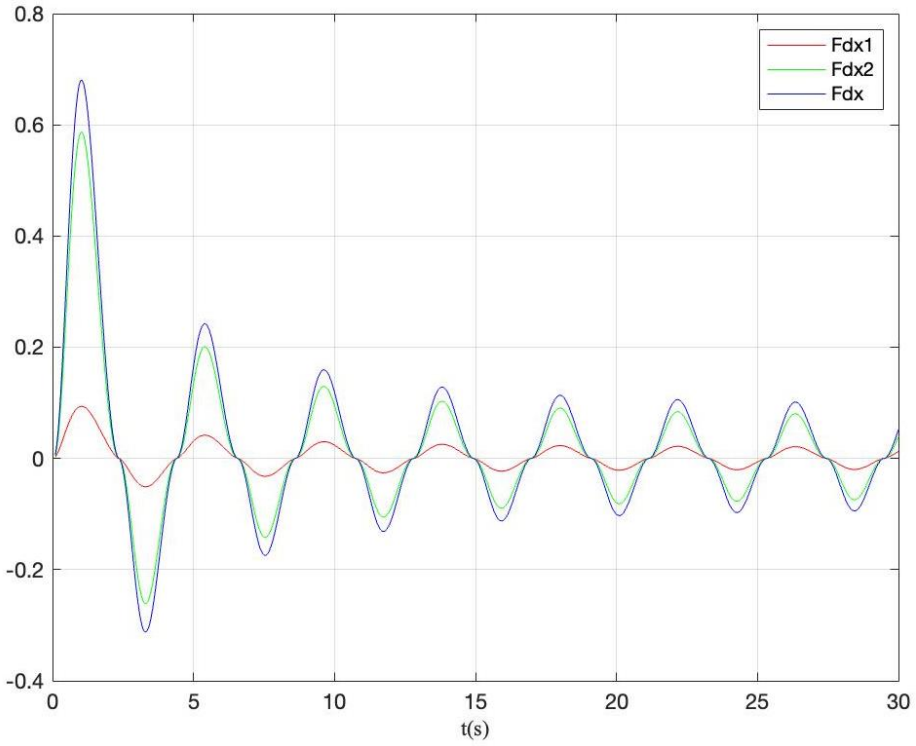

Figure 5.4 Surge force at drop angle 45°

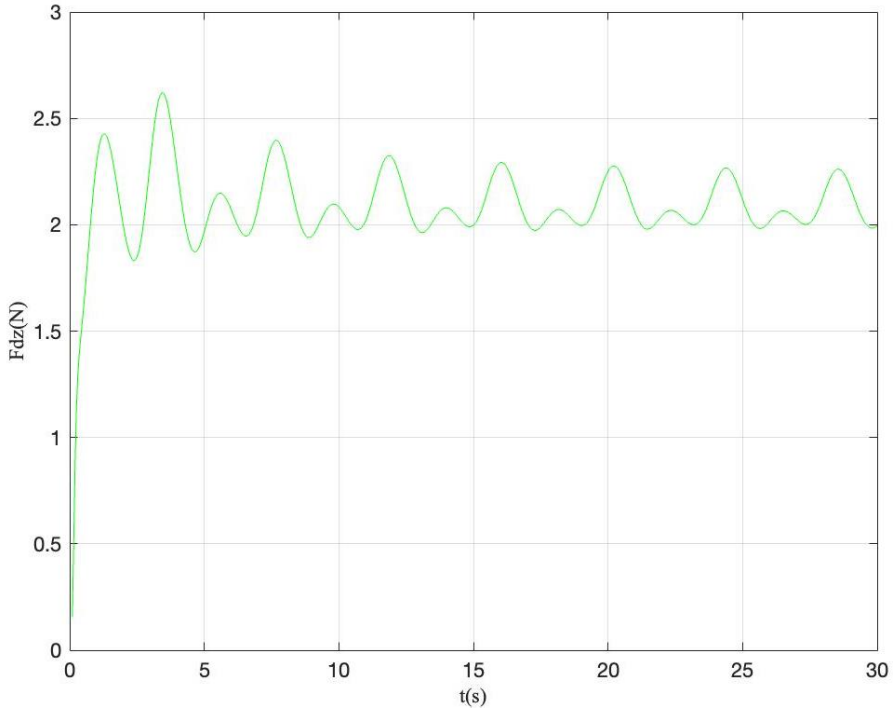

Figure 5.5 Heave force at the drop angle 45°

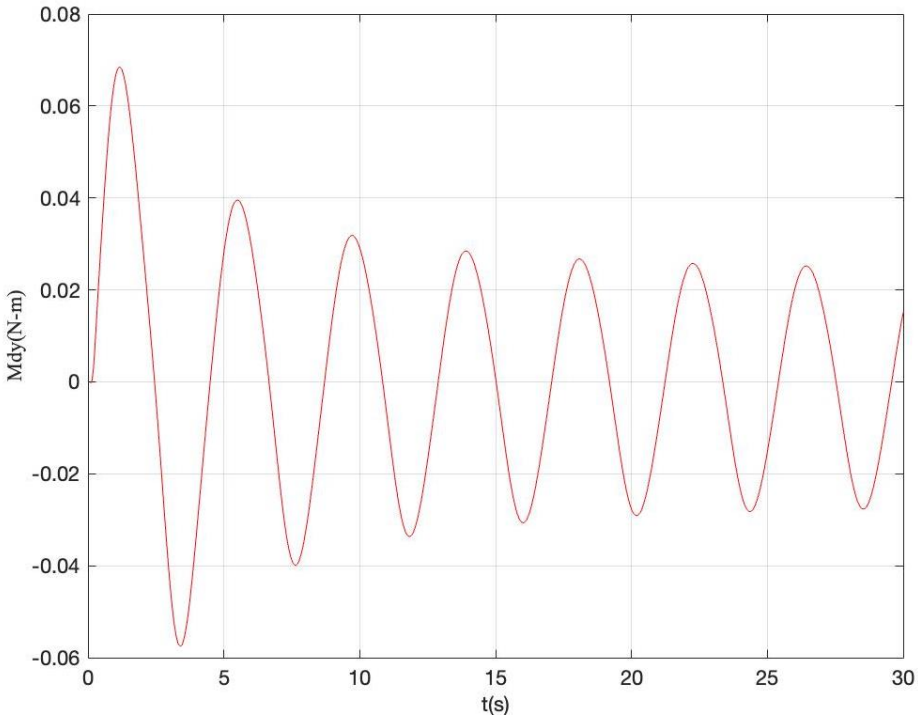

Figure 5.6 Pitch moment at the drop angle 45°

5.2.3 Force components at drop angle 60°

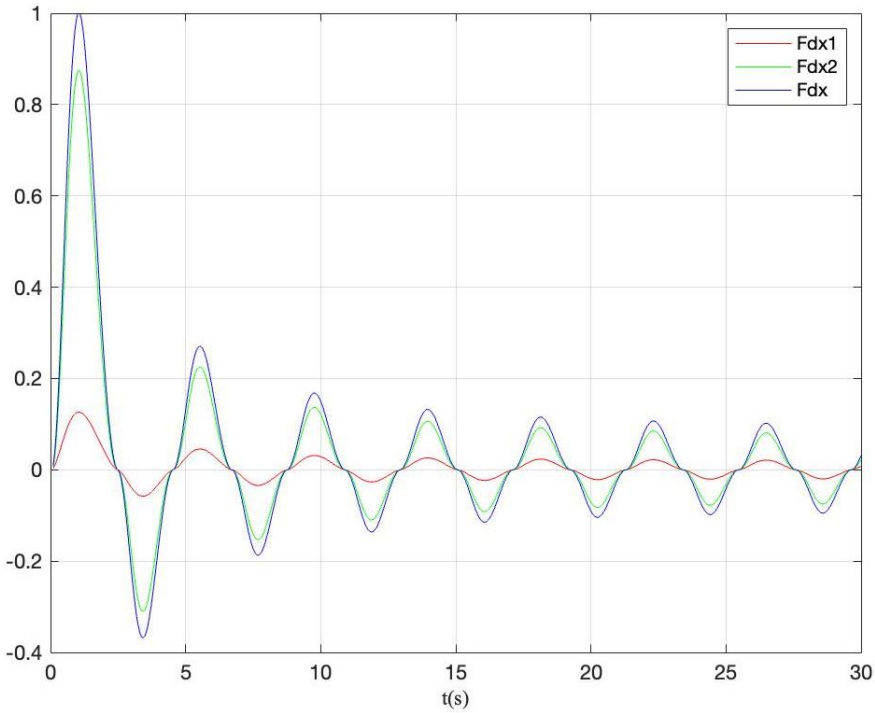

Figure 5.7 Surge force at drop angle 60°

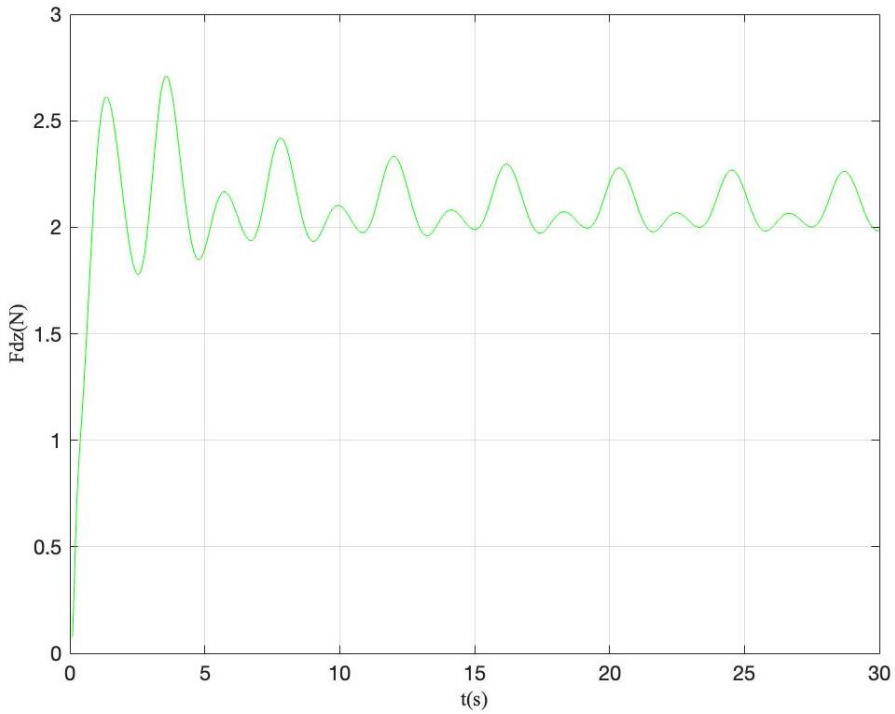

Figure 5.8 Heave force at the drop angle 60°

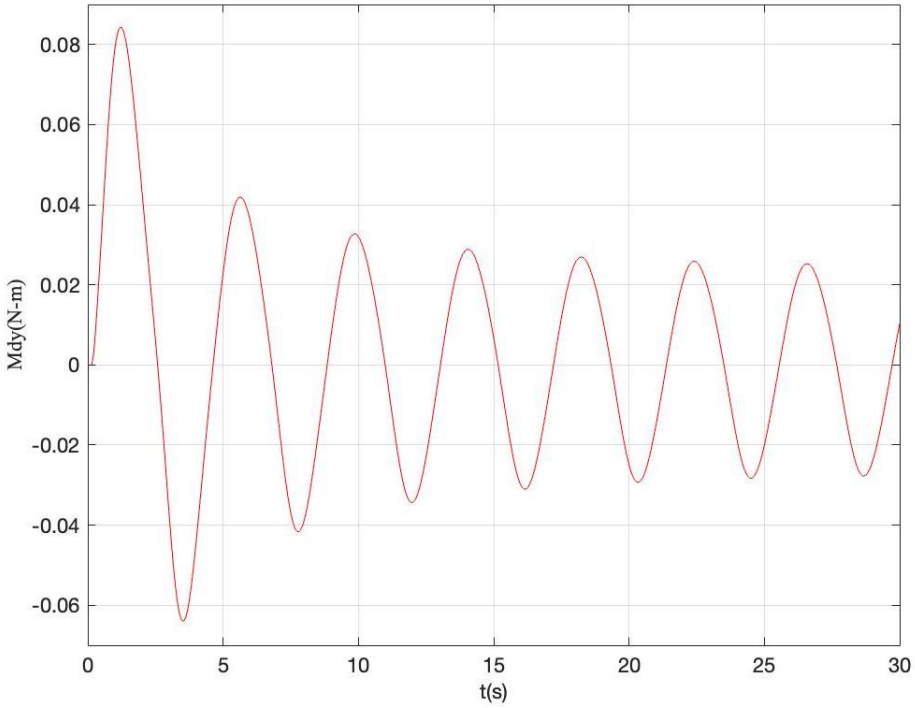

Figure 5.9 Pitch moment at the drop angle 60°

5.3 Probability histogram of dropped cylinders with a fitting normal density function

Since the 3D trajectory is propagated through a nonlinear system, although the noise added in the propagation process is Gaussian distributed, this does not mean that the landing points of the trajectory are also Gaussian distributed. Therefore, we draw a histogram of the landing points of 10,000 random trajectories at a water depth of 5m and fit it with a normal density function, as shown in Figures 5.10-5.12:

As shown in these figures, based on the 3D theory, when adding noise that obeys a Gaussian distribution, the distribution of dropped point of the falling cylinder also approximately obeys a Gaussian distribution.

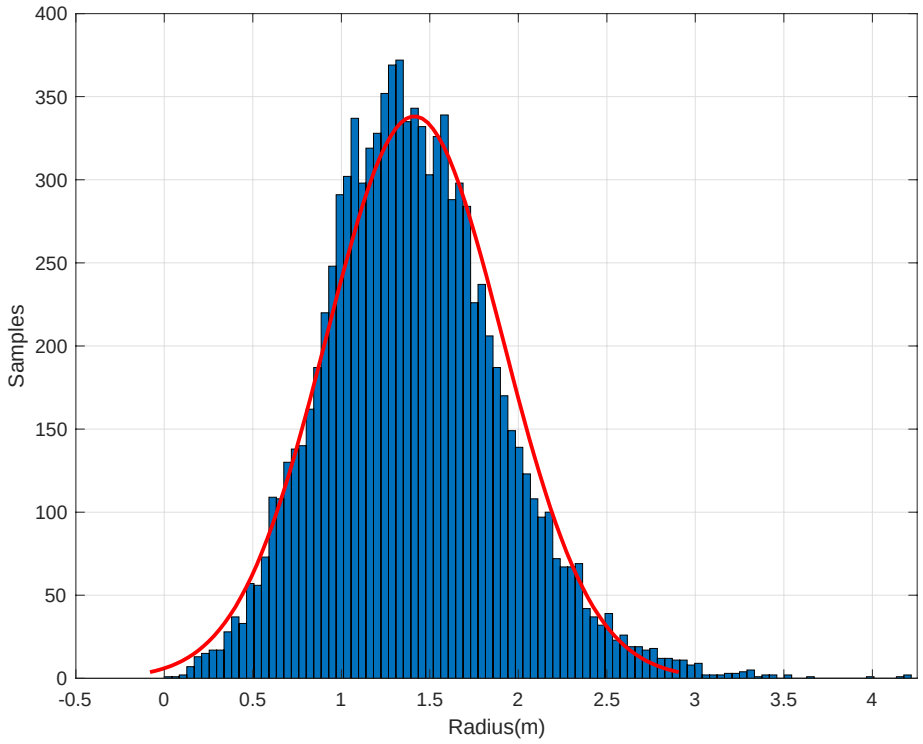

Figure 5.10 Probability histogram of dropped cylinders with a fitting normal density function at the drop angle 30°

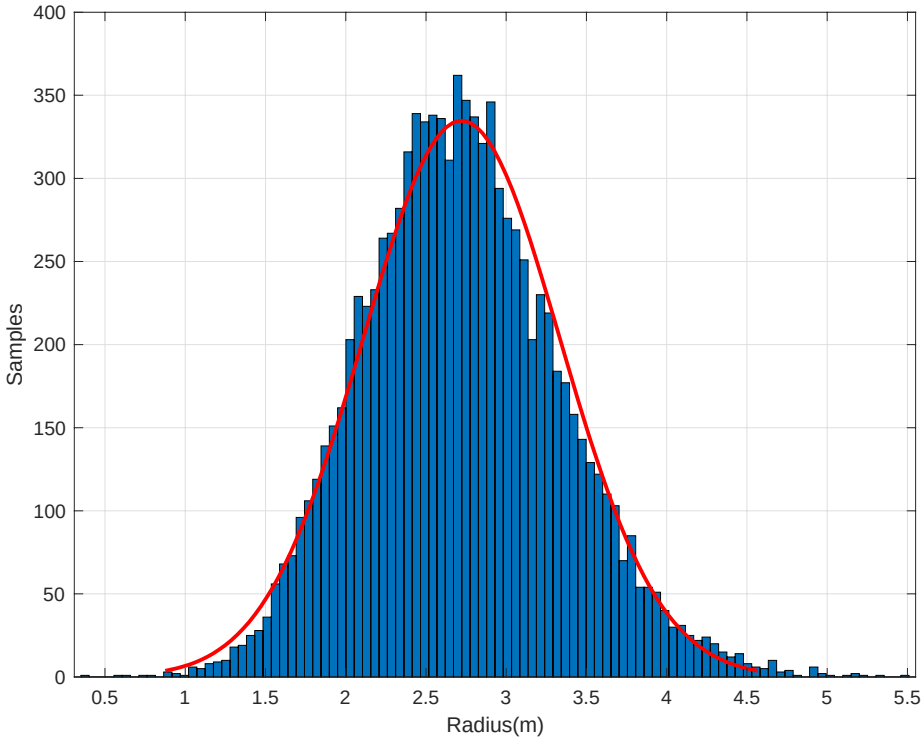

Figure 5.11 Probability histogram of dropped cylinders with a fitting normal density function at the drop angle 45°

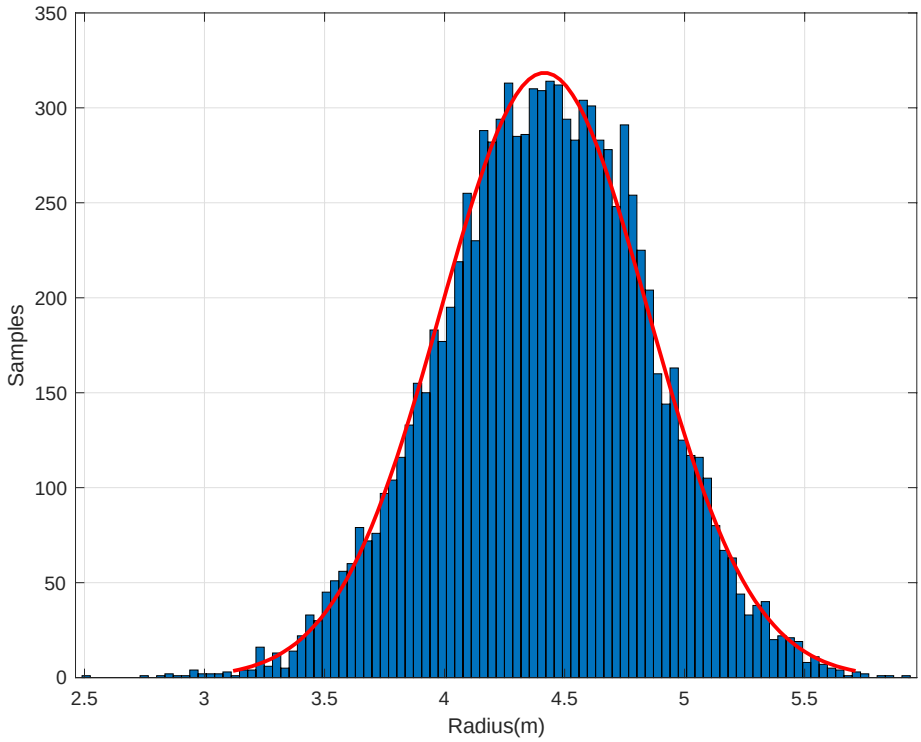

Figure 5.12 Probability histogram of dropped cylinders with a fitting normal density function at the drop angle 60°

5.4 Simulated trajectories and envelopes of dropped cylindrical objects using 2D theory

As mentioned earlier, the state-space model of the dropped cylinder is successfully constructed. And this model provides us with a convenient way to consider the effects of random noise. The results obtained by the MC method, unscented method and Cubature method are shown below. First, consider the case where the drop angle is 45 °. In Figure 5.4, the black and green solid line represent the ideal true (the trajectory without noise), and predicted trajectory from the MC method, respectively. The green dash line and the green dash-dot line represent the upper limit (UL) and lower limit (LL) of the MC method, respectively. The blue dash line and the blue dash-dot line represent the upper limit (UL) and lower limit (LL) of the experimental test, respectively.

In Figure 5.10, the result corresponds to the MC method based on 1296 samples. The sigma range is equal to 1, which means the probability is 0.6826, and the drop angle is 45 °. In general, the trajectory (green line) predicted by the MC method is very close to the ideal true (black line). In Figure 5.11, the "cyan" shaded area is the overlapping area A_{olp} between the predicted drop range from the MC method and the experimental envelope, which covers the area A_{ee}. Yu et al. (2019) proposed a new performance parameter, namely the ratio of the overlap area A_{olp} to the experimental envelope area A_{ee}, as shown below

$$R_A = \frac{A_{olp}}{A_{ee}} \tag{5.1}$$

The above ratio R_A can be used to measure the quality of numerical results, which are compared with the experimental data. Usually, when R_A is greater than 0.5, it is considered that the area of coincidence is large, and the probability of occurrence is also large. Further, the other performance parameter (Yu et al. 2019),

R_L, can be proposed similarly, and it is the ratio between the overlap length $L_{olp}$and the experimental envelope L_{ee} at the bottom, that is

$$R_L = \frac{L_{olp}}{L_{ee}} \tag{5.2}$$

It can measure the accuracy of the probable range at the bottom if compared with the experimental data.

Similarly, the above parameters are also applied to evaluate the results of the unscented method and Cubature method, as shown in Figures 5.12 – 5.15. Compared with the results of the MC method, the trajectory (green line), the overlap area A_{olp} and the overlap length L_{olp} predicted by unscented method and Cubature method are very close, which means the results obtained by the three methods are not significantly different. Table 5.2 compares the results obtained from Figures 5.10 to 5.15. Except for the considerable difference in the calculation time of MC, the other values obtained by the three methods have no difference.

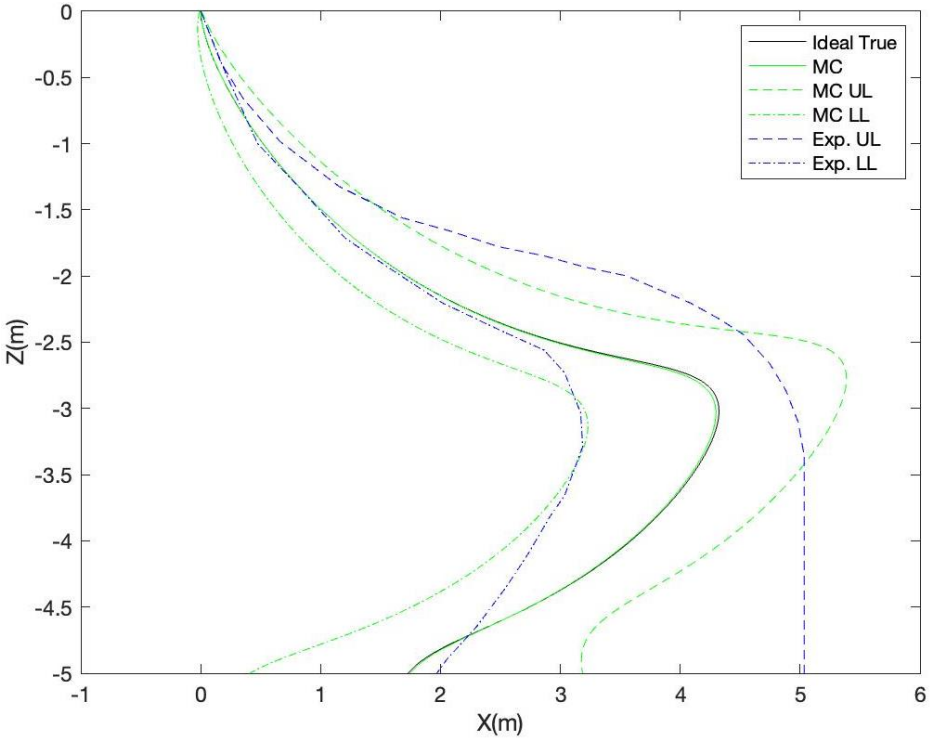

Figure 5.13 Trajectory prediction at the drop angle 45° using MC method (Samples =1296, α =0.6826)

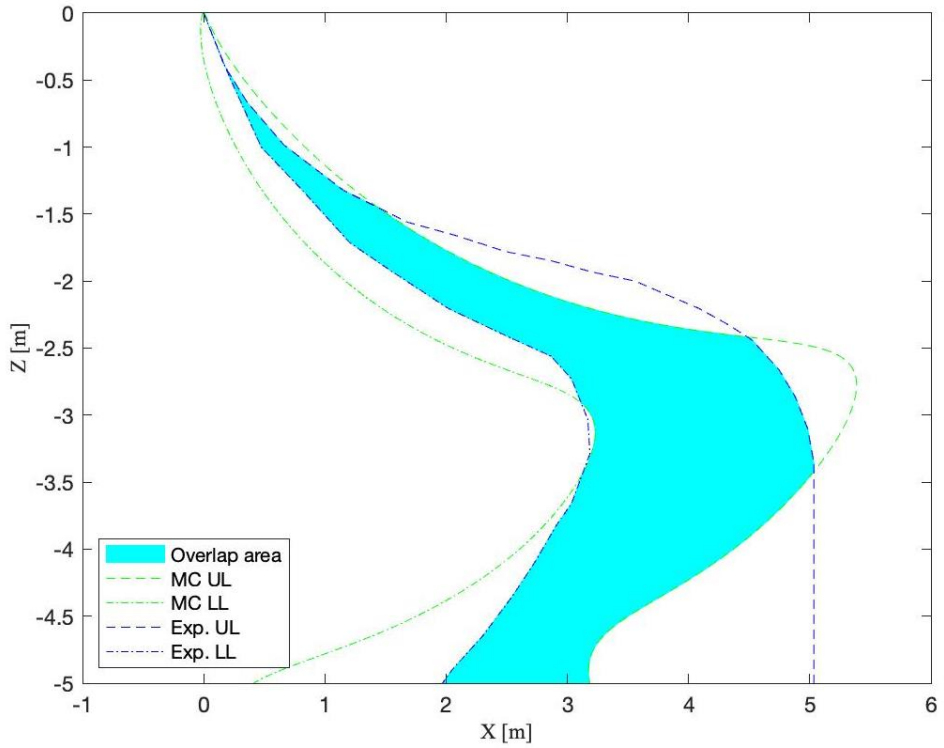

Figure 5.14 Overlap area between MC method and experimental envelope with the drop angle 45°(Samples =1296, α =0.6826)

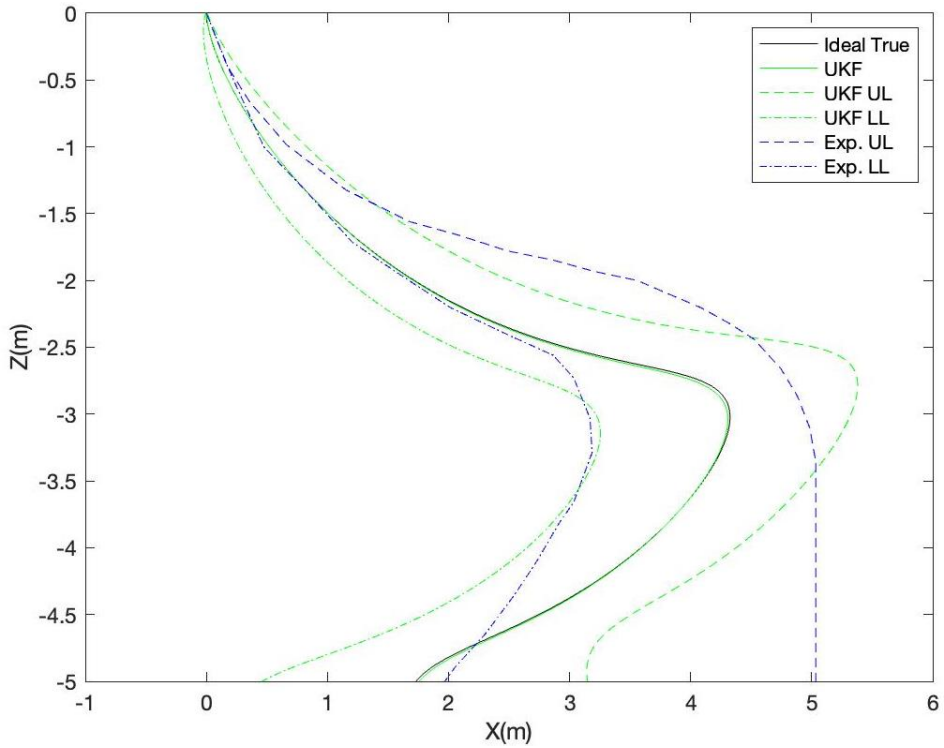

Figure 5.15 Trajectory prediction at the drop angle 45° using unscented method (α =0.6826)

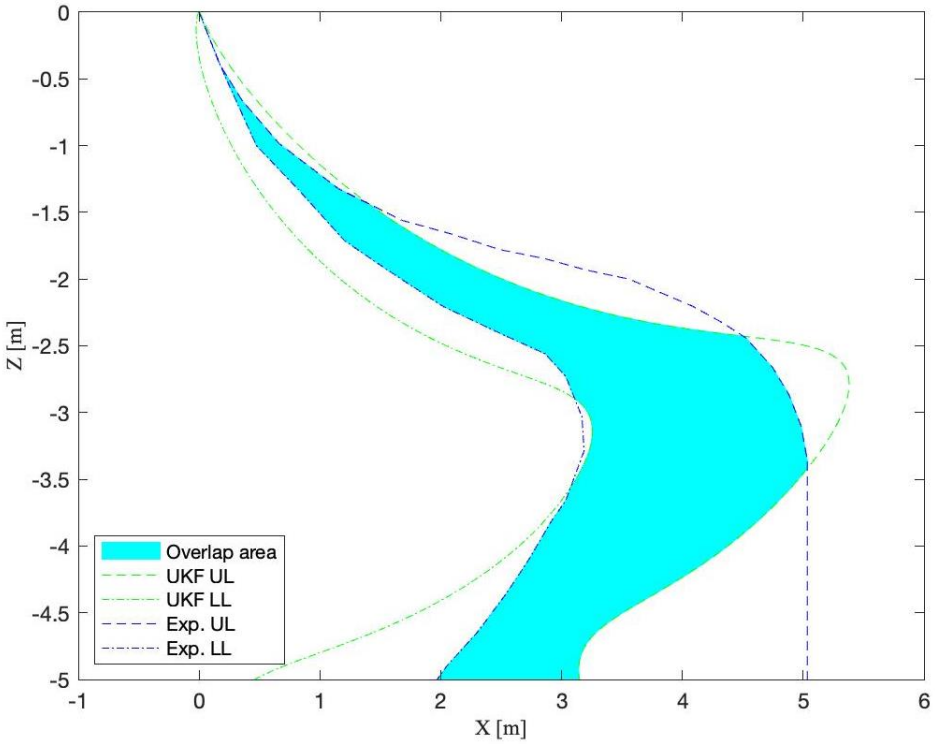

Figure 5.16 Overlap area between unscented method and experimental envelope with the drop angle 45°(α =0.6826)

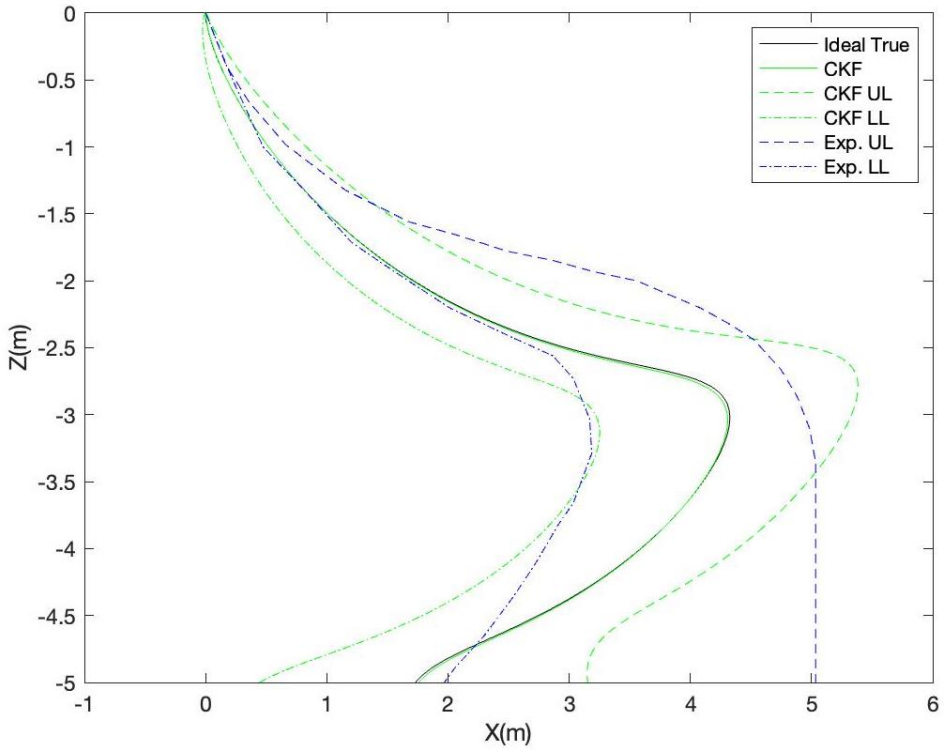

Figure 5.17 Trajectory prediction at the drop angle 45° using Cubature method (α =0.6826)

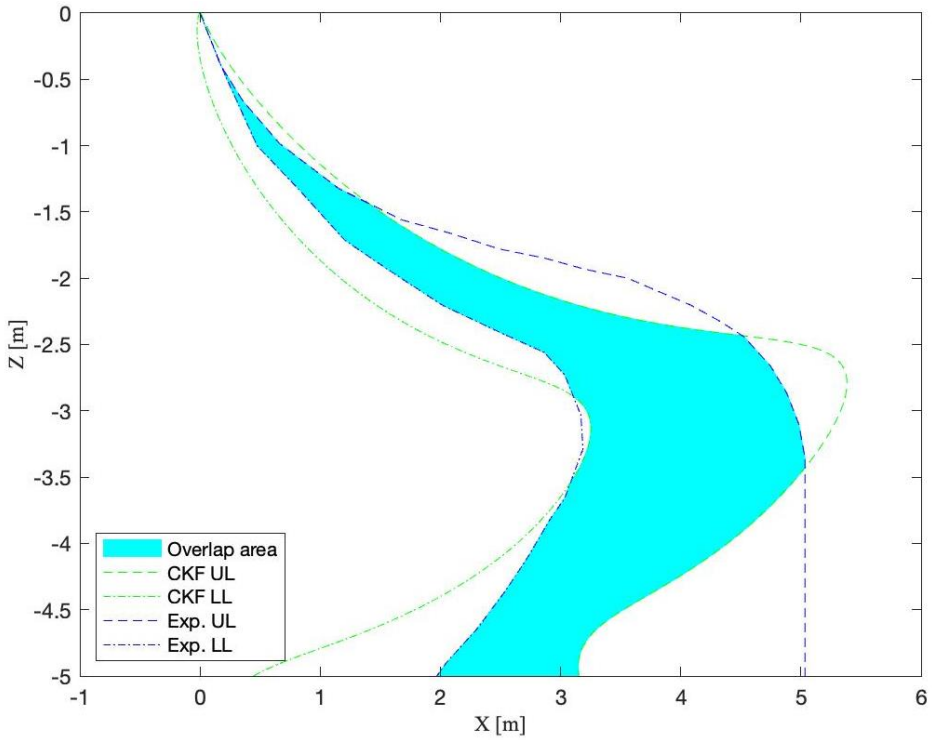

Figure 5.18 Overlap area between Cubature method and experimental envelope with the drop angle 45°(α =0.6826)

Table 5.2 Prediction results derived from these three methods under the same conditions at drop angle= 45°

Method	α	Time(s)	R_A	R_L	MSE
MC method (Samples=1296)	0.6826	34.133	0.701	0.397	3.40E-04
Unscented method	0.6826	1.873	0.695	0.385	3.24E-04
Cubature method	0.6826	1.636	0.697	0.387	3.07E-04

For the drop angle of 45 °, R_A and R_L calculated by the MC method under different samples have been summarized in Table 5.2. MSE, the mean square error between MC and the ideal true. A smaller MSE value indicates that the method produces a precise solution closer to the ideal true.

Since the MSE of the results given by the other two methods is 0 when three decimal places are taken (Table 5.6 and 5.7), In Table 5.3, the MSE is equal to 0 only when the samples are greater than 12,96. Therefore, the results of the MC method with the samples of 1296 are compared with the other two methods. The application of the MC method requires a large number of samples to obtain relatively accurate results. Increasing the number of samples is not an effective way to improve accuracy. Also, from Table 5.4, even when the MSE is small, the R_A and R_L obtained by the MC method under the same samples are very different. The envelope obtained by the MC method is not stable. In contrast, the other two methods can

always get the same result when solved multiple times under the same conditions. Therefore, in the actual calculation, the MC method needs to repeat the sampling ten times under the same number of samples and take the average of the ten results to obtain relatively reliable results. Figure 5.16 shows the relationship between $\ln(Simples)$ and time from the MC method for drop angle $45°$, which indicates the calculation time increases exponentially with the number of samples.

Table 5.3 Prediction results derived from MC method at drop angle=45° (Samples =1296, α =0.6826)

Samples	Time	R_A	R_L	MSE
$2^4 = 16$	0.432	0.623	0.297	2.71E-02
$3^4 = 81$	2.012	0.671	0.382	6.96E-03
$4^4 = 256$	6.478	0.691	0.384	1.74E-03
$5^4 = 625$	16.076	0.699	0.393	5.17E-04
$6^4 = 1296$	34.134	0.701	0.397	3.40E-04
$7^4 = 2401$	66.261	0.704	0.402	2.51E-04
$8^4 = 4096$	123.046	0.708	0.404	2.63E-04
$9^4 = 6561$	215.957	0.709	0.405	2.87E-04

Table 5.4 Prediction results derived from MC method at drop angle=45° (Samples =10×1296, α =0.6826)

Samples	Time	R_A	R_L	MSE
1296	34.350	0.707	0.403	1.1E-03
1296	35.276	0.697	0.398	1.2E-03
1296	34.859	0.708	0.409	2.7E-04
1296	34.832	0.711	0.412	8.1E-04
1296	34.332	0.697	0.392	2.4E-04
1296	33.943	0.712	0.413	2.8E-04
1296	34.131	0.693	0.391	7.5E-04
1296	34.097	0.692	0.385	3.0E-04
1296	34.988	0.699	0.399	6.3E-04
1296	34.190	0.707	0.406	3.1E-04

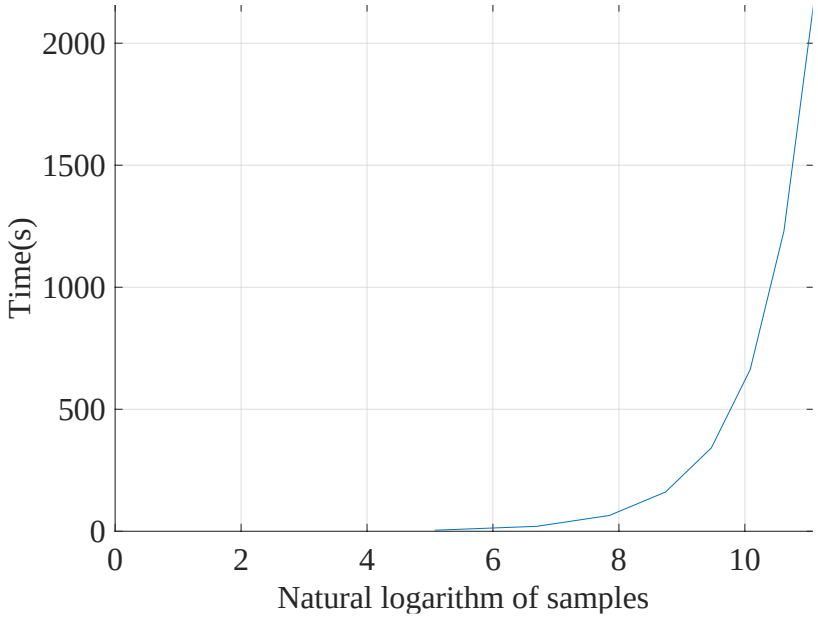

Figure 5.19 Time(s) vs. Natural logarithm of samples from MC method for drop angle 45°

Similarly, R_A and R_L determined by the three methods under different probability with a drop angle of 45 ° are reported in Tables 5.4, 5.5 and .6, respectively. The R_A and R_L obtained by the MC method are consistent with the results from the other two methods except for the calculation time. The time required by the unscented method and Cubature method is only 5% of the MC method.

In Table 5.3 and 5.4, R_A and R_L from unscented method and Cubature method are basically the same. Compared with unscented method, Cubature method is slightly better in calculation time by generating fewer sample points, which can be an advantage when computing more complex models. The difference between their R_A and R_L can be neglectable.

Table 5.5 Prediction results derived from MC method at drop angle=45° (α =0.1- 0.9)

α	Time	R_A	R_L	MSE
0.1	33.339	0.104	0.000	3.07E-04
0.2	32.329	0.206	0.041	2.62E-04
0.3	32.368	0.312	0.094	4.73E-04
0.4	32.384	0.420	0.168	3.71E-04
0.5	32.264	0.519	0.233	2.55E-04
0.6	32.842	0.615	0.315	4.73E-04
0.7	33.171	0.707	0.405	2.04E-04
0.8	32.717	0.803	0.565	4.71E-04
0.9	32.659	0.888	0.746	2.23E-04

Table 5.6 Prediction results derived from unscented method at drop angle=45° (α =0.1- 0.9)

α	Time	R_A	R_L	MSE
0.1	1.888	0.105	0.000	3.13E-04
0.2	1.892	0.205	0.039	3.07E-04
0.3	1.902	0.308	0.096	3.18E-04
0.4	1.849	0.414	0.159	3.06E-04
0.5	1.862	0.516	0.228	3.10E-04
0.6	1.918	0.615	0.307	3.26E-04
0.7	1.816	0.710	0.403	3.10E-04
0.8	1.842	0.789	0.531	3.32E-04
0.9	1.874	0.886	0.733	3.20E-04

Table 5.7 Prediction results derived from Cubature method at drop angle=45° (A =0.1- 0.9)

α	Time	R_A	R_L	MSE
0.1	1.686	0.105	0.000	3.09E-04
0.2	1.639	0.206	0.040	3.30E-04
0.3	1.639	0.309	0.098	3.49E-04
0.4	1.629	0.415	0.160	3.21E-04
0.5	1.622	0.518	0.229	3.13E-04
0.6	1.660	0.617	0.309	3.33E-04
0.7	1.651	0.712	0.405	3.19E-04
0.8	1.651	0.791	0.532	3.06E-04
0.9	1.675	0.888	0.734	3.09E-04

5.5 Simulated results of dropped cylindrical objects using 3D theory

5.5.1 Force components at drop angle 30°

For the numerical results of the cylinder model in the 3D theory without coupling term, the force components F_{dx}, F_{dz} and M_{dy} in Figures 20 – 28 are similar to the force components in 2D theory. This shows that our 3D theory is accurate.

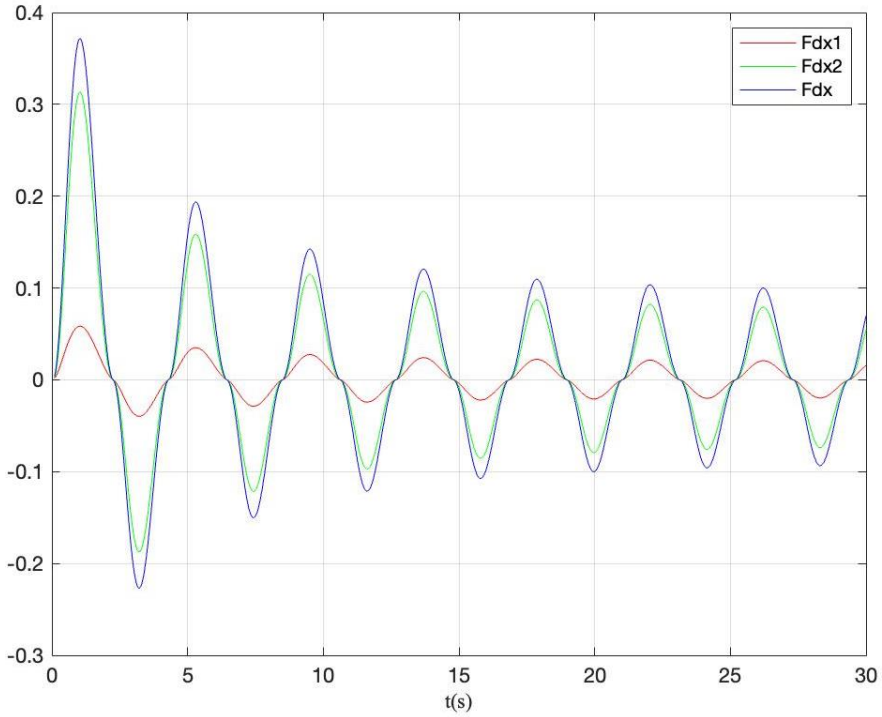

Figure 5.20 Surge force at drop angle 30°

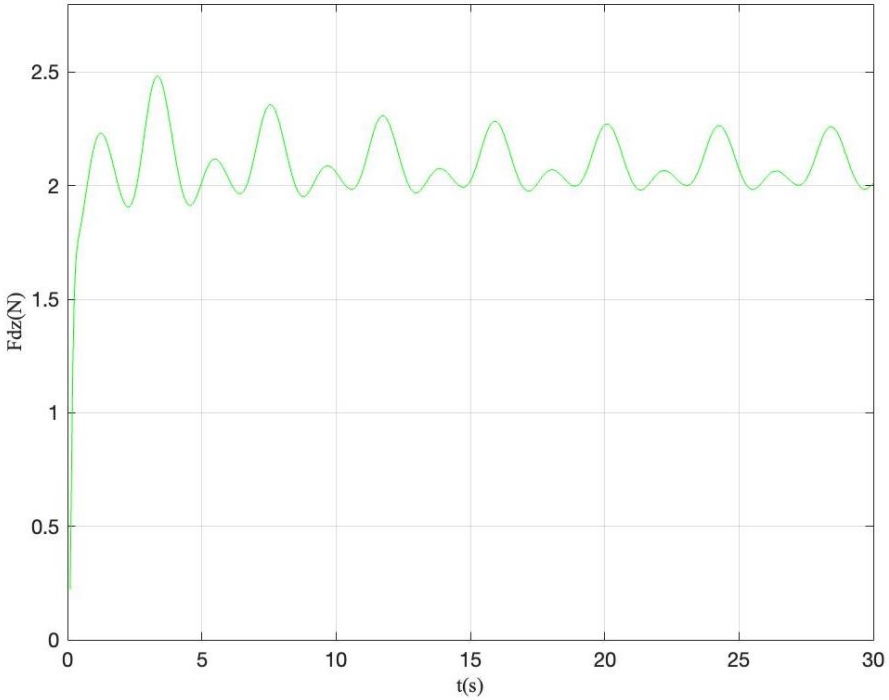

Figure 5.21 Heave force at the drop angle 30°

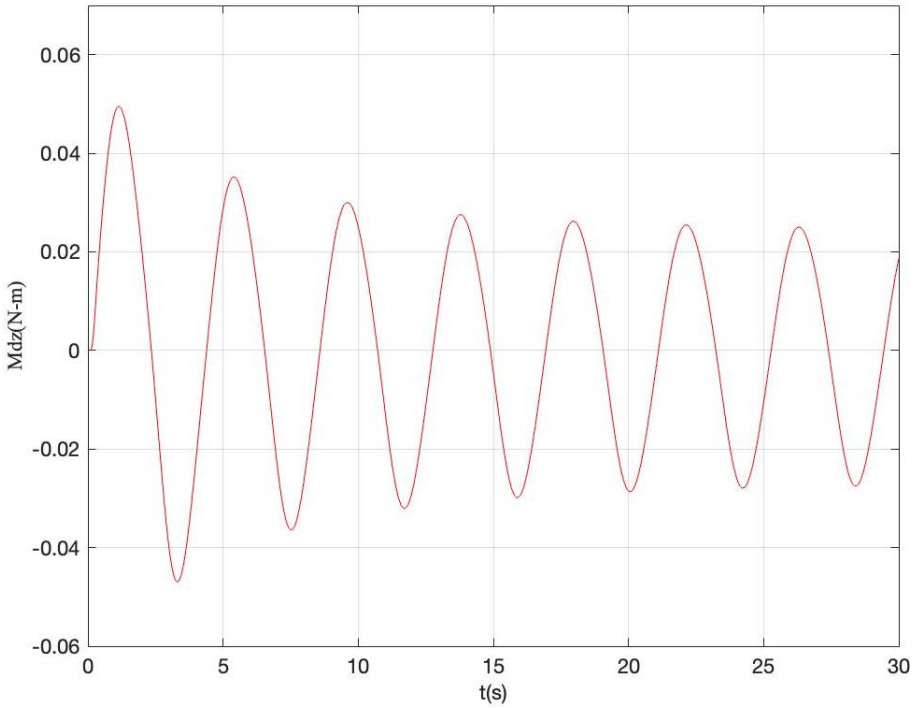

Figure 5.22 Pitch moment at the drop angle 30°

5.5.2 Force components at drop angle 45°

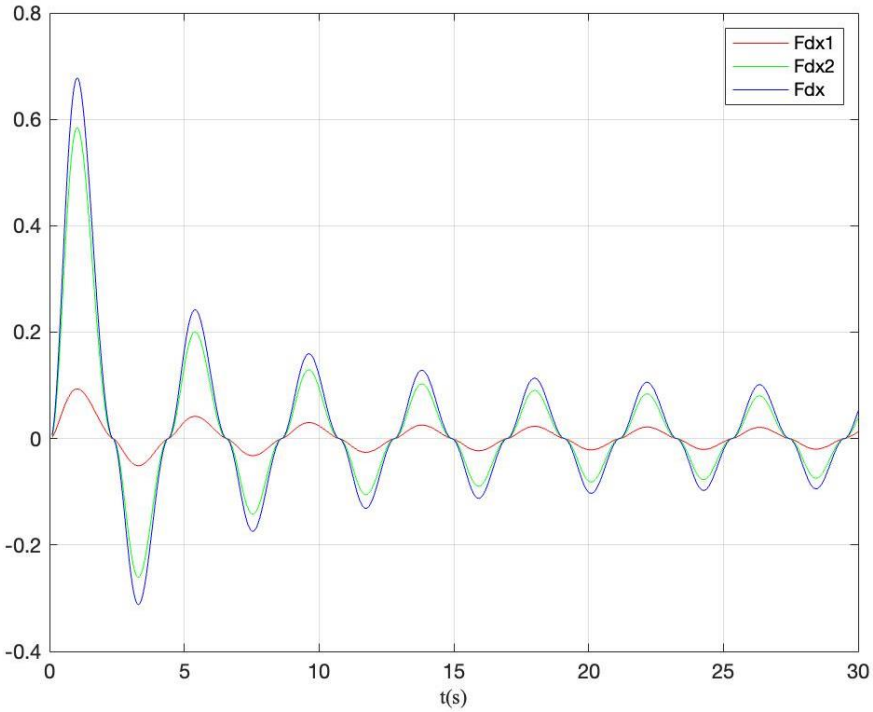

Figure 5.23 Surge force at drop angle 45°

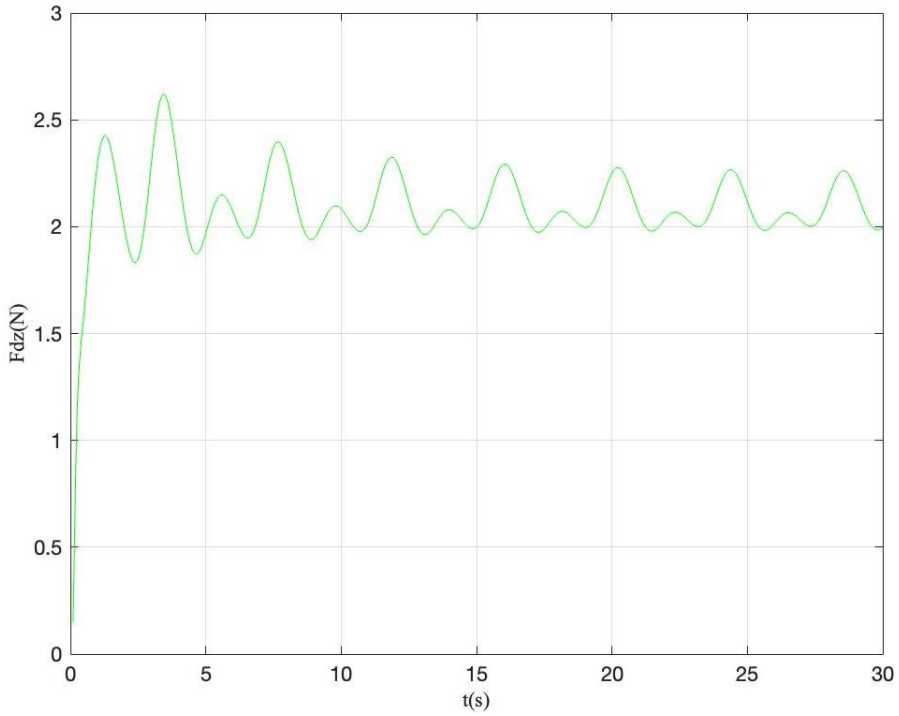

Figure 5.24 Heave force at the drop angle 45°

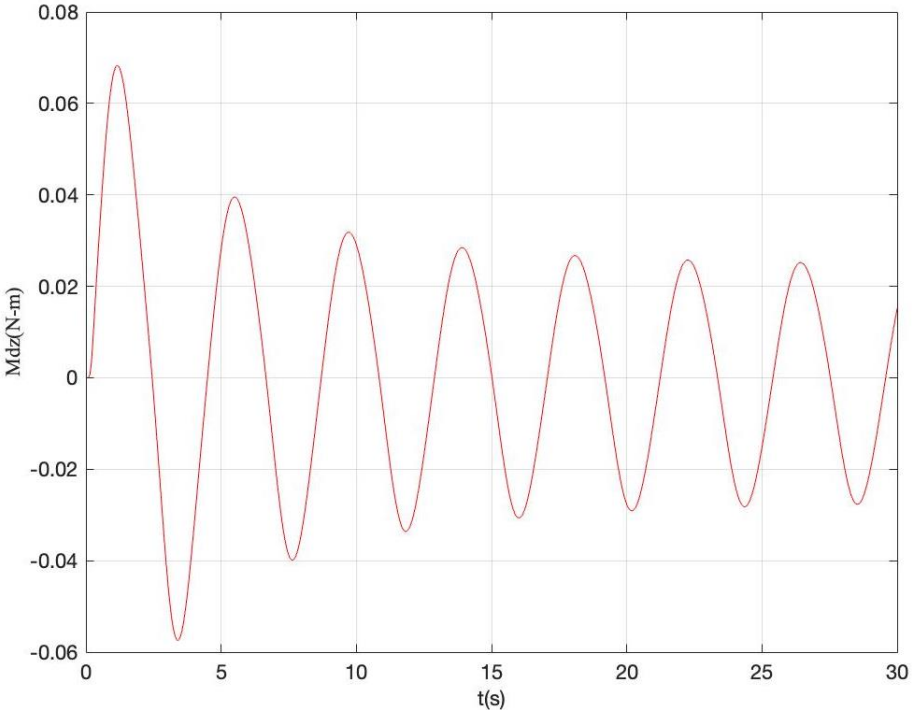

Figure 5.25 Pitch moment at the drop angle45°

5.5.3 Force components at drop angle 60°

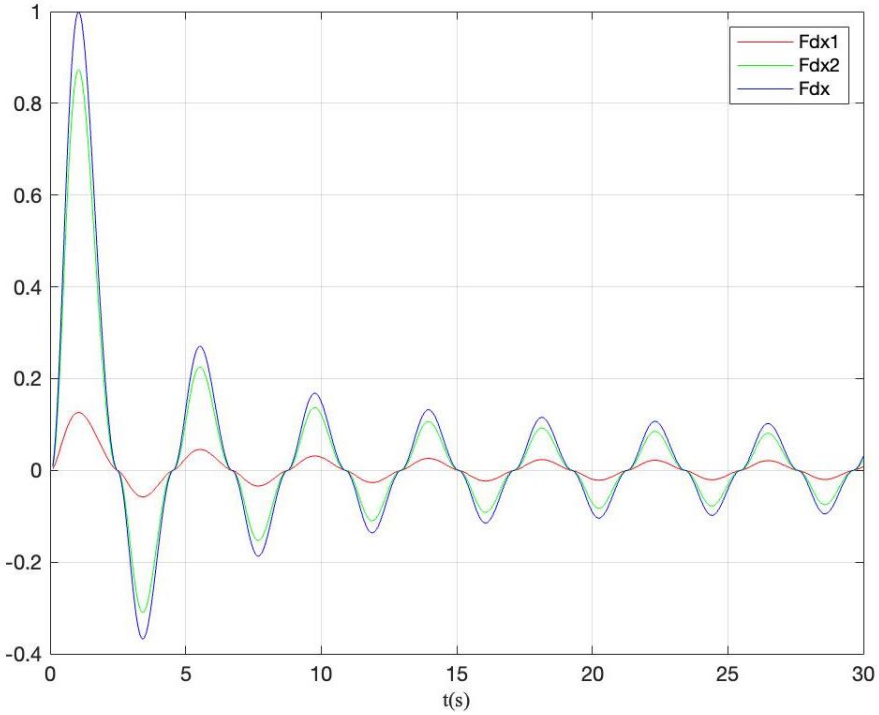

Figure 5.26 Surge force at drop angle 60°

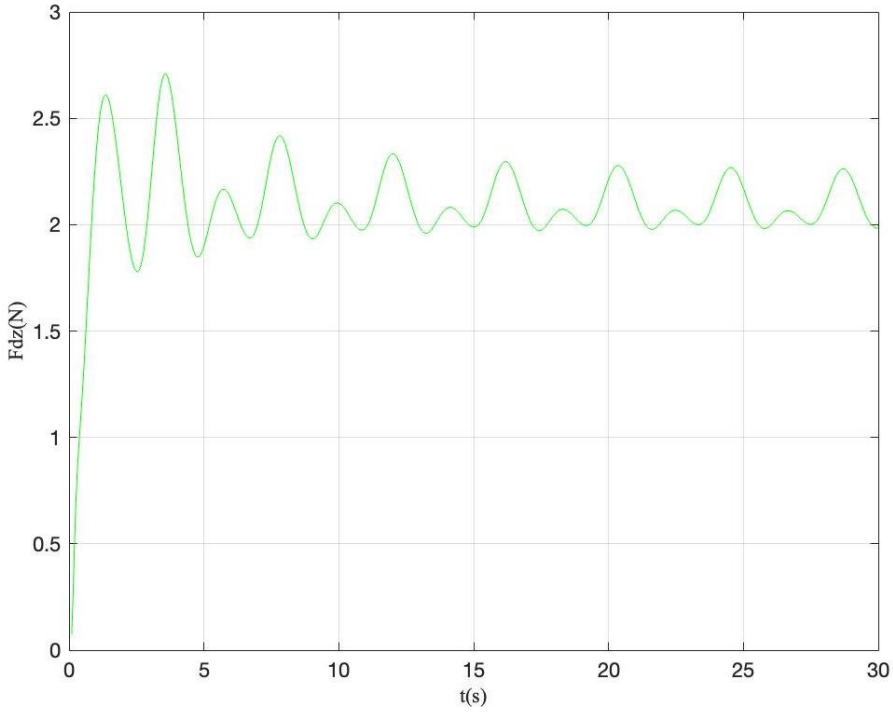

Figure 5.27 Heave force at the drop angle 60°

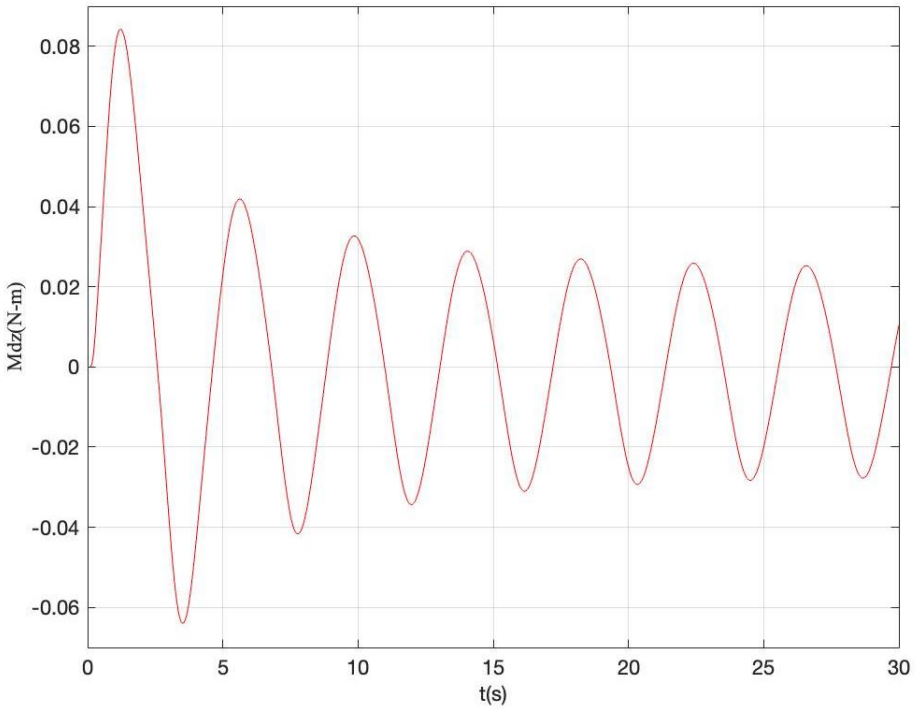

Figure 5.28 Pitch moment at the drop angle 60°

5.6 Simulated trajectories and envelopes of dropped cylindrical objects using 3D theory

Similar to 2D, we analyze the results of the above three methods with a drop angle of 45 degrees as an example. Figures 5.29, 5.31, and 5.33 show the simulated trajectories and envelopes of the three methods, respectively. Figure 5.29 shows that the trajectory of the MC simulation is very close to the ideal true at the beginning, but after the first inflection point, there is a clear difference between these two trajectories. It can also be seen from the MSE at each moment of the MC method in Figure 5.35 that the error of the MC method will continue to accumulate in the system, and the system will not correct it (in Figure 5.35, the MSE of MC method begins to decrease after 3.5s, because ideal true is about to reach the second inflection point, and the trajectory starts to show a rightward trend).

The trajectory and envelope predicted by the unscented method are shown in Figure 5.31. The simulation trajectory of the unscented method is not as good as that of the MC at the beginning. However, the measurement update part in the system will self-correct the points propagate at each time step, so its simulation results will not deviate much from ideal true in general.

Relative to the trajectory of MC method, the trajectories of unscented method and square-root Cubature method were not significantly different. Since there are far more parameters in the three-dimensional state-space model than in the two-dimensional state-space model, the calculation results are not as stable as in the 2D model. Although it can be seen from Figure 5.34 that the results for square-root Cubature method in this simulation are slightly better, after several simulations, the results between square-root Cubature method and unscented method are comparable.

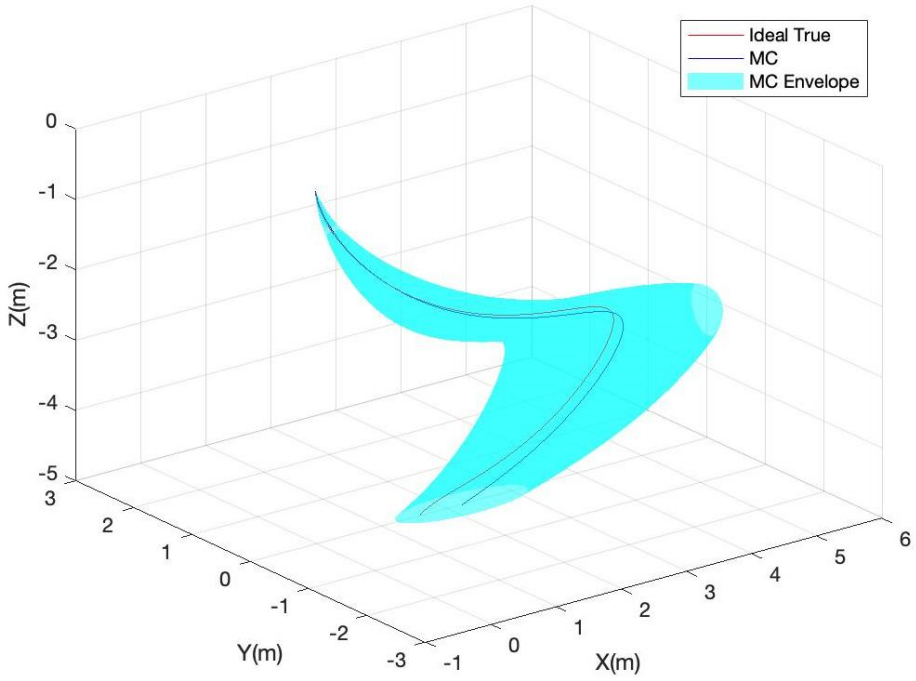

Figure 5.29 Trajectory and envelope prediction at the drop angle 45° using MC method (α =0.6826)

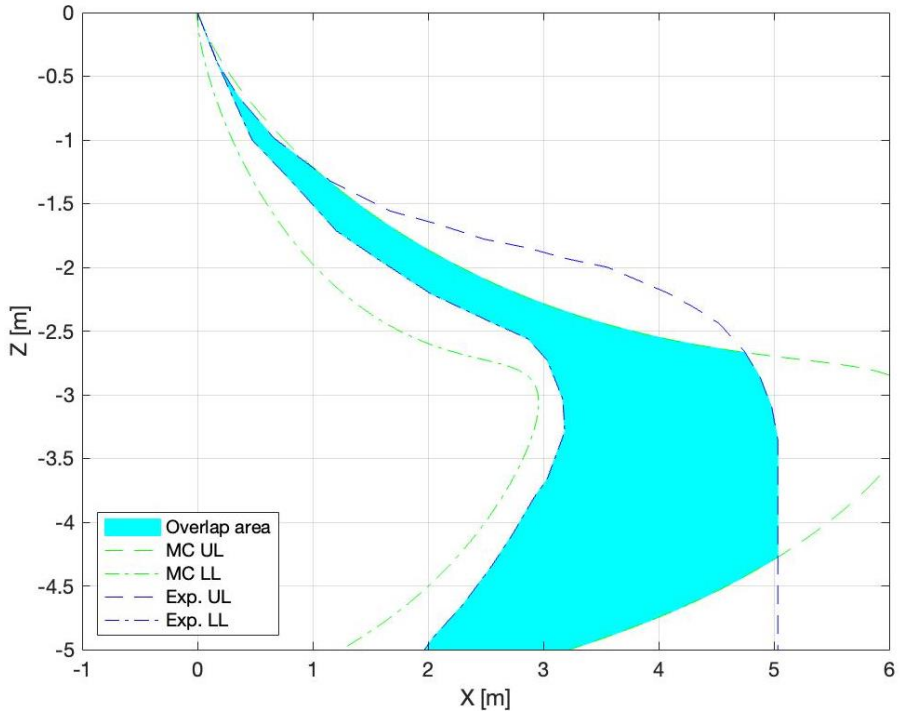

Figure 5.30 Overlap area between MC method and experimental envelope with the drop angle 45°(Samples =10000, α =0.6826)

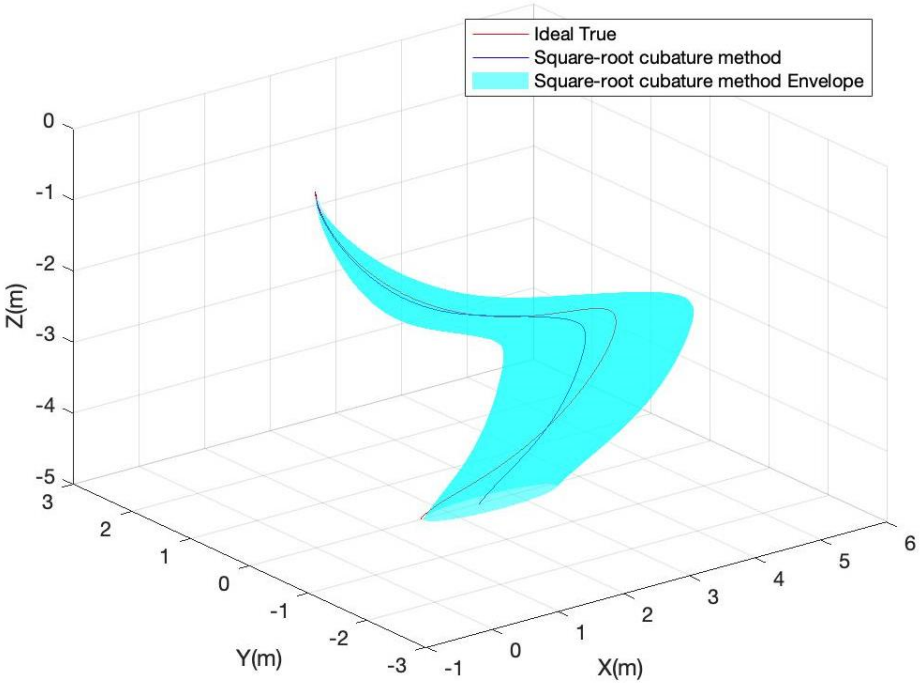

Figure 5.31 Trajectory and envelope prediction at the drop angle 45° using unscented method (α =0.6826)

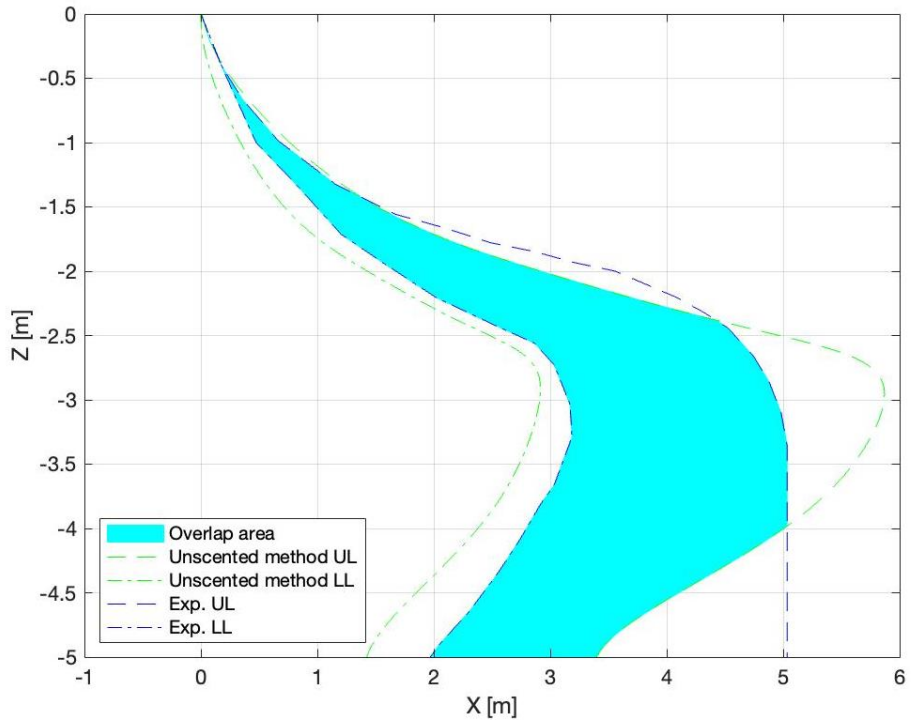

Figure 5.32 Overlap area between unscented method and experimental envelope with the drop angle 45°(α =0.6826)

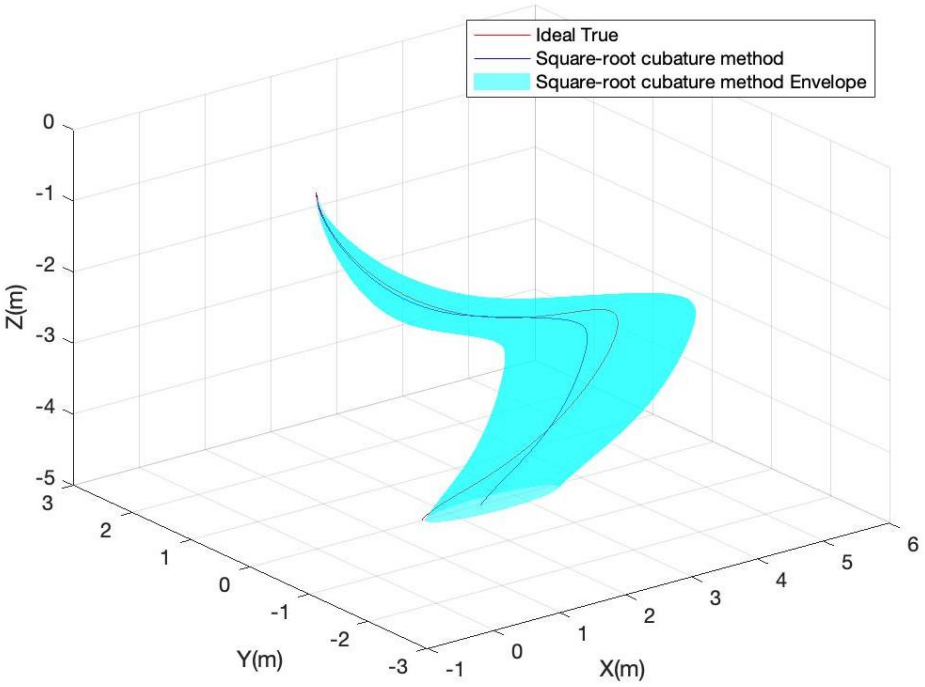

Figure 5.33 Trajectory and envelope prediction at the drop angle 45° using square-root Cubature method (α =0.6826)

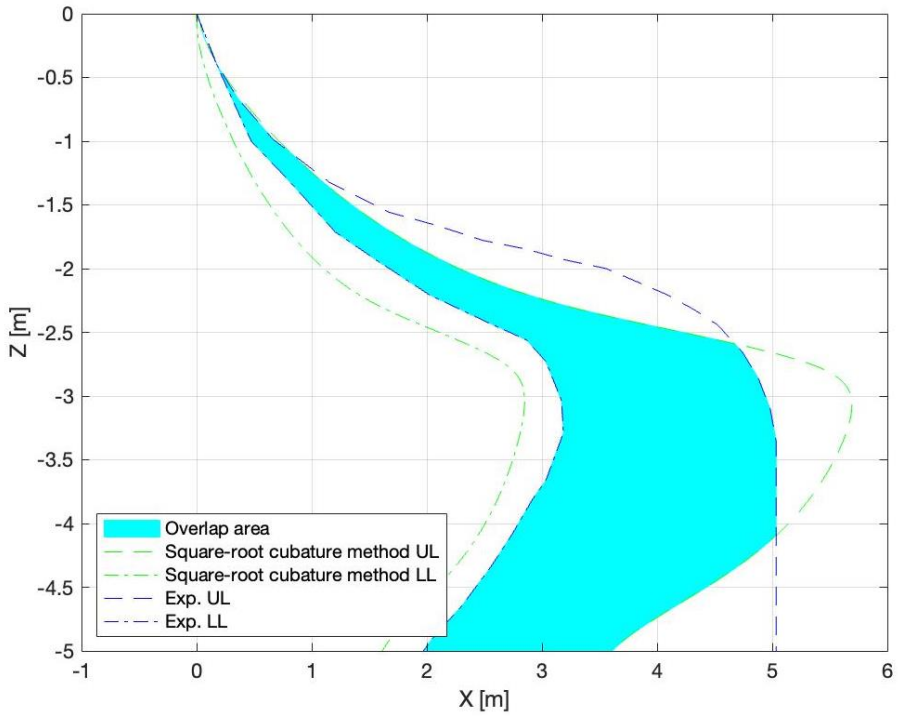

Figure 5.34 Overlap area between square-root Cubature method and experimental envelope with the drop angle 45°(α =0.6826)

As shown in Figures 5.35 -5.37, although unscented method and square-root Cubature method have large mean square error (MSE) at the beginning, after the adjustment of the measure update, their errors are rapidly reduced, that is, the accuracy of the prediction is improved. For the MC method, the MSE in the system increases over time, which can lead to inaccurate predictions when predicting long-time falling object trajectories.

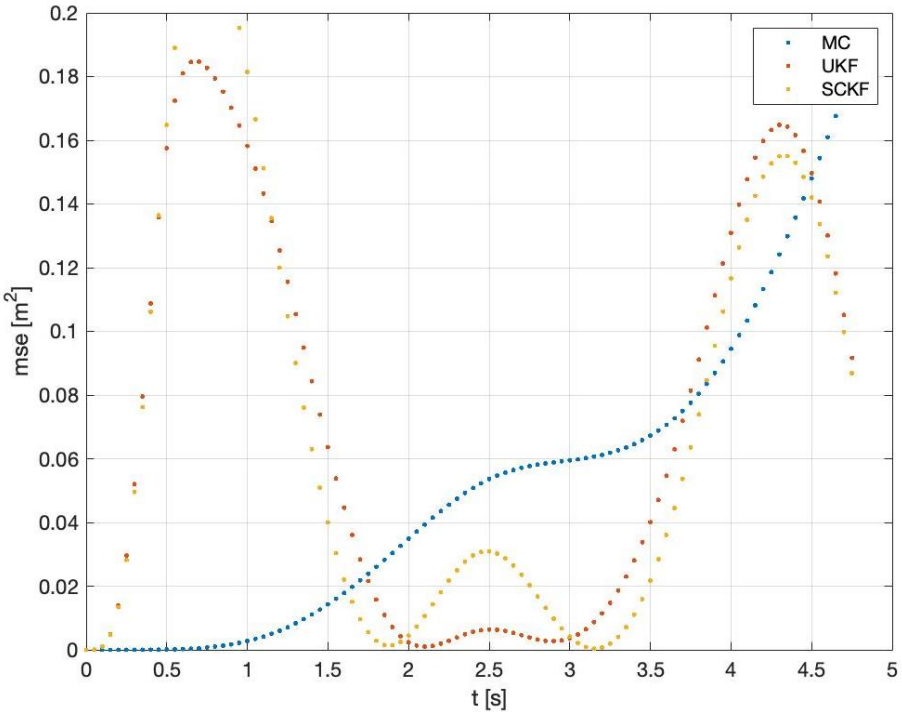

Figure 5.35 MSE between three methods and the ideal true at each time step with the drop angle 30°

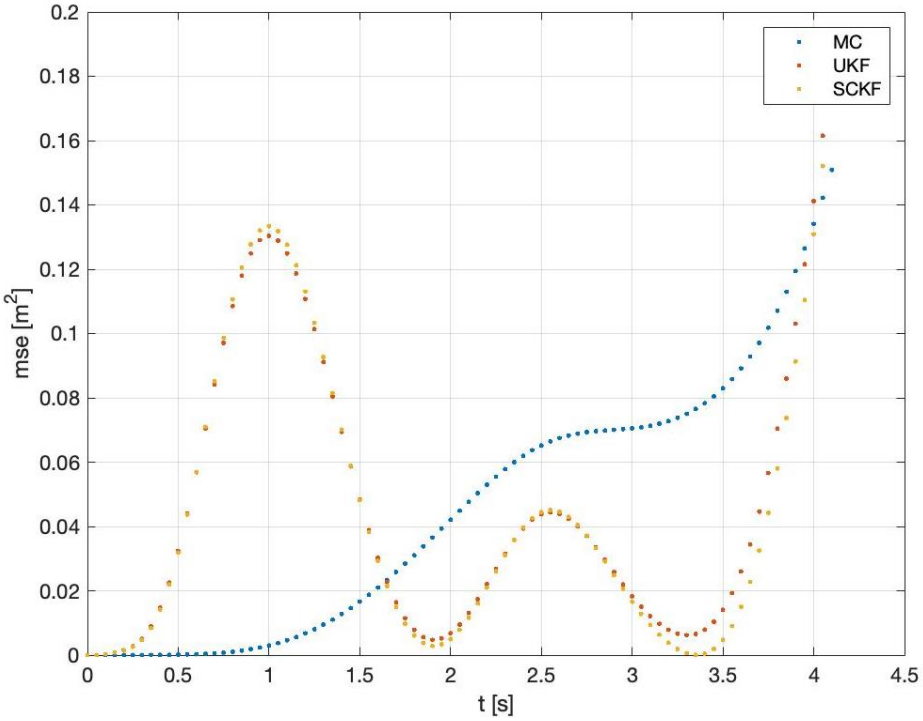

Figure 5.36 MSE between three methods and the ideal true at each time step with the drop angle 45°

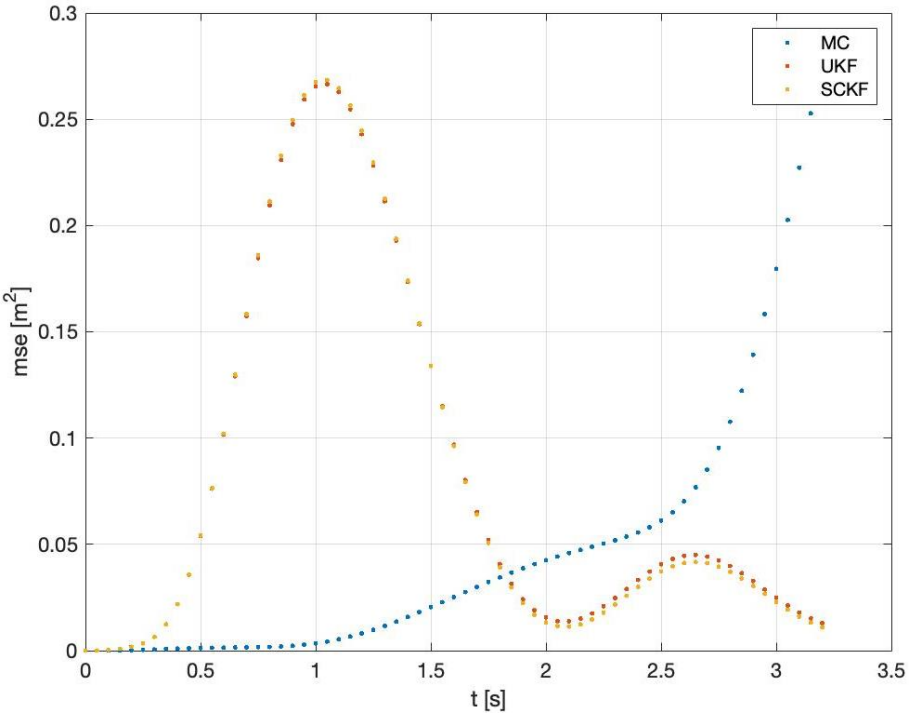

Figure 5.37 MSE between three methods and the ideal true at each time step with the drop angle 60°

For the drop angle of 30°, 45° and 60°, R_A and R_L calculated by the MC method under different samples have been summarized in Tables 5.8-5.10. MSE, the mean square error between MC and the ideal true. A smaller MSE value indicates that the method produces a precise solution closer to the ideal true. It can be seen that for these three angles, the results obtained by the three methods are very similar, but the MC method requires more computational time.

Table 5.8 Prediction results derived from these three methods under the same conditions at drop angle= 30°

Method	α	Time	R_A	R_L	MSE
MC method (Samples=10000)	0.6826	132.142	0.640	0.568	4.60E-02
Unscented method	0.6826	4.157	0.708	0.416	3.20E-02
Square-root Cubature method	0.6826	4.928	0.707	0.422	3.50E-02

Table 5.9 Prediction results derived from these three methods under the same conditions at drop angle= 45°

Method	α	Time	R_A	R_L	MSE
MC method (Samples=10000)	0.6826	131.656	0.779	0.403	5.20E-02
Unscented method	0.6826	4.277	0.834	0.474	8.90E-02
Square-root Cubature method	0.6826	5.156	0.834	0.470	9.70E-02

Table 5.10 Prediction results derived from these three methods under the same conditions at drop angle=60°

Method	α	Time	R_A	R_L	MSE
MC method (Samples=10000)	0.6826	132.022	0.596	0.820	4.70E-02
Unscented method	0.6826	4.143	0.590	0.603	8.00E-02
Square-root Cubature method	0.6826	4.694	0.598	0.603	8.00E-02

Tables 5.11-5.13 shows the results of the three methods when confidence coefficient α=0.1 - 0.9. It can be seen that the change of α will only change R_A and R_L, and has no significant effect on calculation time or MSE. For the square-root Cubature method, the three-dimensional envelopes at drop angles $30°, 45°, 60°$ and compare these envelopes with the experimental envelopes from Aanesland with α=0.1 - 0.9 are presented in Appendix.

Table 5.11 Prediction results derived from MC method at drop angle=45° (α =0.1- 0.9)

α	Time	R_A	R_L	MSE
0.1	124.811	0.106	0.072	3.61E-2
0.2	124.278	0.216	0.145	3.82E-2
0.3	124.134	0.327	0.219	3.94E-2
0.4	124.672	0.438	0.275	3.85E-2
0.5	124.282	0.531	0.315	3.77E-2
0.6	124.877	0.612	0.366	3.79E-2
0.7	124.372	0.686	0.417	3.68E-2
0.8	124.376	0.751	0.462	3.52E-2
0.9	131.381	0.802	0.520	3.78E-2

Table 5.12 Prediction results derived from unscented method at drop angle=45° (α =0.1- 0.9)

α	Time	R_A	R_L	MSE
0.1	4.115	0.145	0.080	4.26E-2
0.2	4.078	0.288	0.157	4.31E-2
0.3	3.985	0.432	0.240	4.22E-2
0.4	4.005	0.571	0.307	5.31E-2
0.5	3.968	0.667	0.366	4.87E-2
0.6	3.972	0.746	0.394	3.91E-2
0.7	3.967	0.814	0.459	4.03E-2
0.8	4.041	0.846	0.486	4.33E-2
0.9	3.989	0.886	0.529	4.08E-2

Table 5.13 Prediction results derived from square-root Cubature method at drop angle=45° (α =0.1- 0.9)

α	Time	R_A	R_L	MSE
0.1	5.245	0.140	0.078	5.82E-2
0.2	4.932	0.278	0.153	6.27E-2
0.3	5.002	0.415	0.233	6.39E-2
0.4	5.055	0.506	0.271	7.28E-2
0.5	4.943	0.616	0.328	6.76E-2
0.6	4.910	0.648	0.339	9.09E-2
0.7	4.885	0.785	0.438	5.05E-2
0.8	4.958	0.843	0.486	5.68E-2
0.9	4.908	0.891	0.570	5.45E-2

Figures 5.38-5.40 shows the area of confidence interval with different water depth at drop angle30°, 45°and 60°, It can be seen that the 3d trajectory envelopes of the three methods have similar trends, which shows the similarity between the 3D results of the three methods.

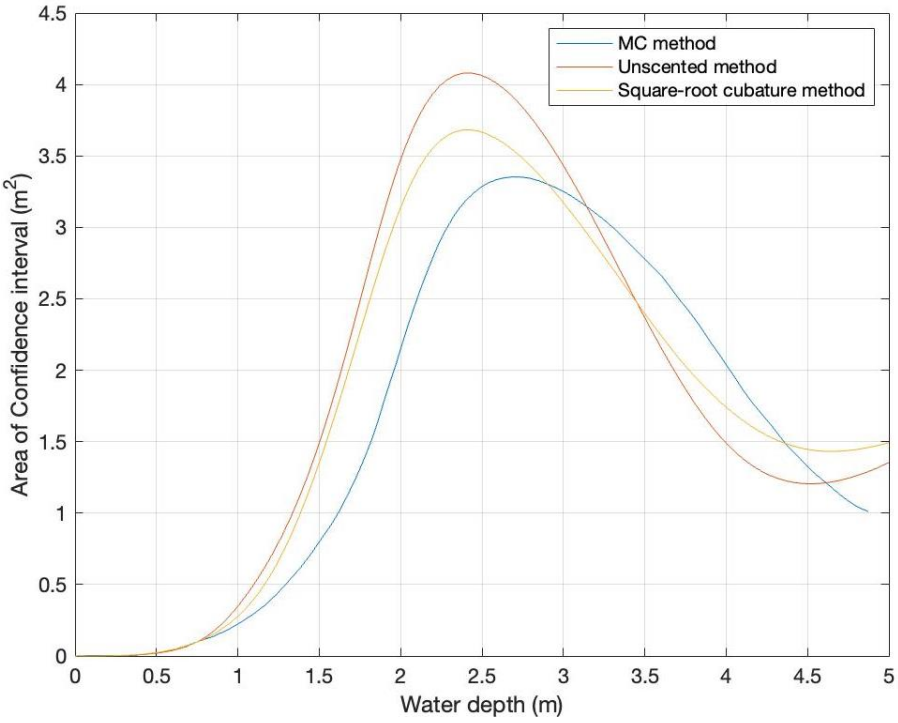

Figure 5.38 The area of confidence interval with different water depth at drop angle 30° (α =0.6826)

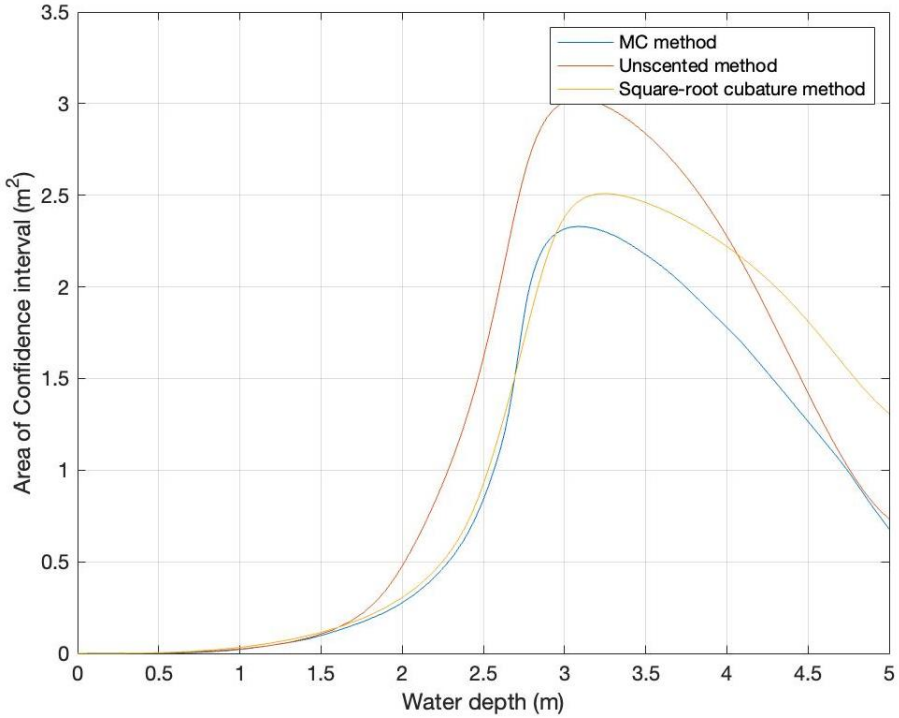

Figure 5.39 The area of confidence interval with different water depth at drop angle 45° (α =0.6826)

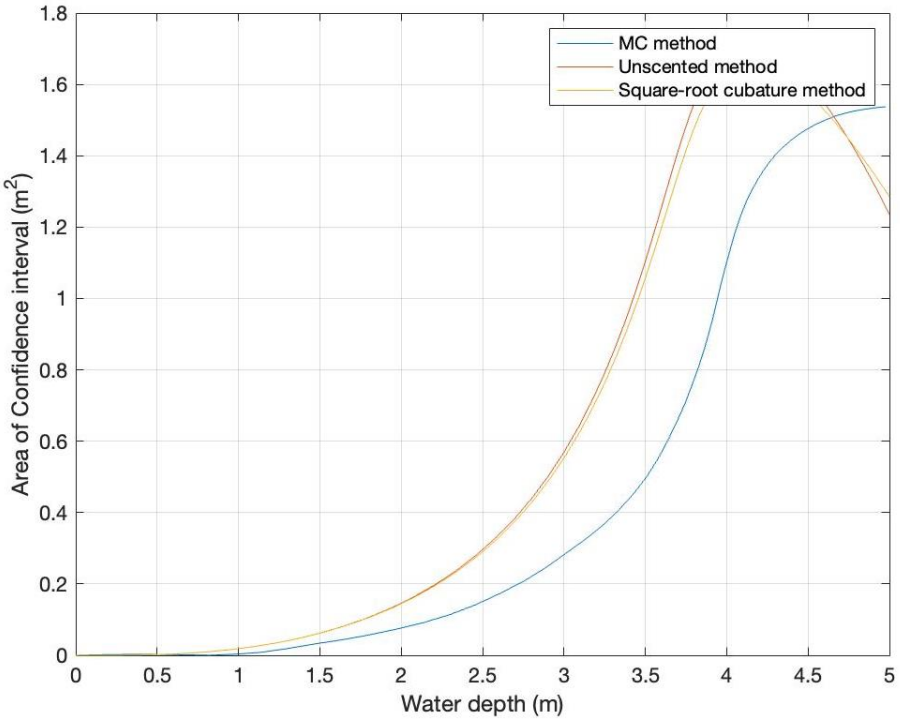

Figure 5.40 The area of confidence interval with different water depth at drop angle 60° (α =0.6826)

5.7 Comparison of dropped cylinders using 2D model and 3D model

Figures 5.27 – 5.29 show a comparison of X-Z plane trajectories from 2D and 3D simulations with drop angles of 30°, 45°, and 60° and a corresponding experimental envelope. In the absence of noise, especially when rolling frequency = 0, the 3D trajectory has no displacement in the y direction at all. It can be considered that under the same conditions, the 2D and 3D trajectories are basically the same. Except for the drop angle of 60 degrees, other trajectories are within the experimental envelope. Even in the case of 60 degrees, the trend of the simulation results is similar to the trajectory envelope. This indicates that under these three angles, the simulation results of both models are in good agreement with the experimental results.

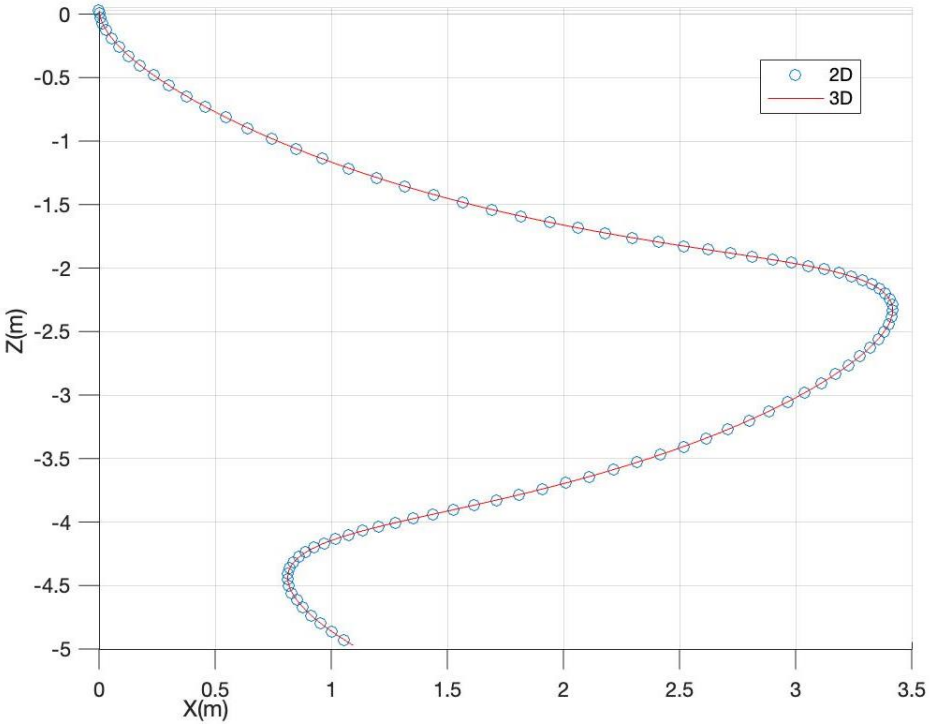

Figure 5.41 Comparison of trajectories of dropped cylinders using 2D model and 3D model at drop angle 30°

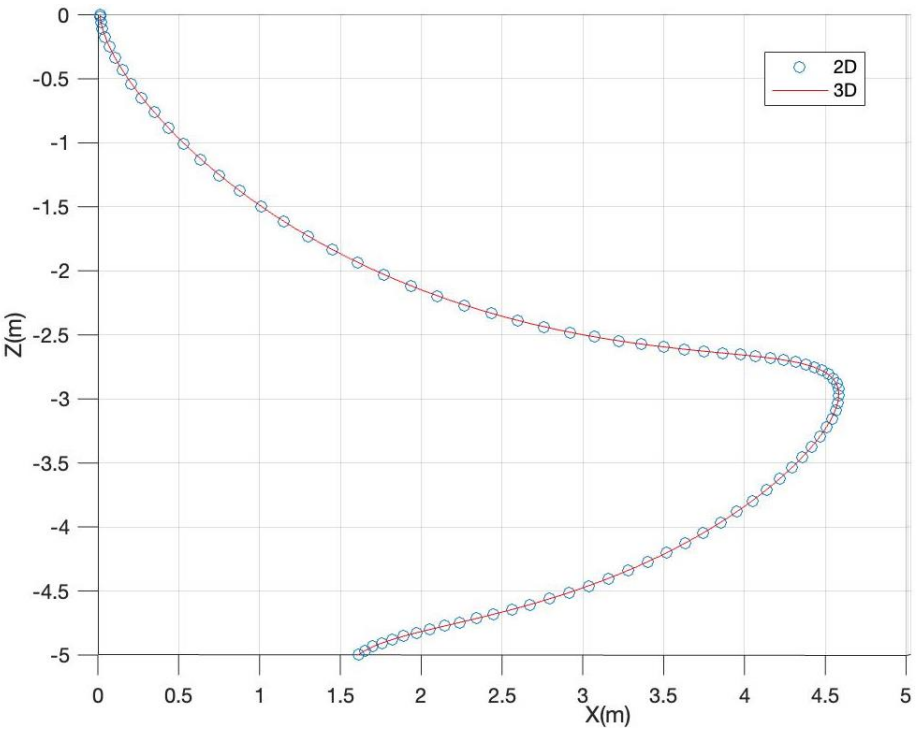

Figure 5.42 Comparison of trajectories of dropped cylinders using 2D model and 3D model at drop angle 45°

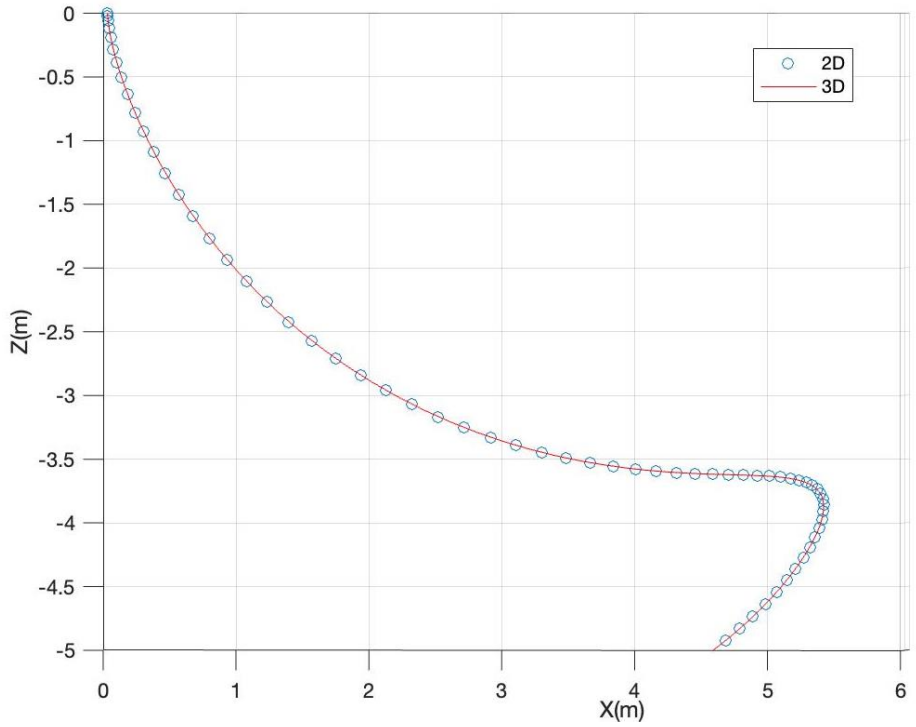

Figure 5.43 Comparison of trajectories of dropped cylinders using 2D model and 3D model at drop angle 60°

Chapter 6: Conclusions

In this doctoral dissertation, we focus on the trajectories of dropped objects, including container models and cylindrical objects.

Firstly, a Stratasys F170 FDM printer successfully produces six container models made of acrylonitrile styrene acrylate (ASA). These models represent three loading conditions with different densities and COG, each with two samples. After measurement, the relative error between the actual geometric and the pre-designed dimensions is very small, which fully meets the requirements of experimental tests in naval architecture and offshore engineering. In addition, four models with a hole are filled with heavier materials, such as steel or aluminum, to make their average density greater than water. The measured results of COG and the density agree with the theoretical design values, which also fully meet the accuracy requirements of the test. Overall, additive manufacturing provides a fast, efficient, and more economical way to make small-scaled maritime structural models.

Furthermore, four container models have been dropped into the calm water in UNO's towing tank. The effects of various factors, such as drop angle, the center of gravity and mass density, etc., on the trajectories of the dropped container models have been comprehensively investigated experimentally. In addition, the falling pattern of container models has been tentatively proposed and summarized. The drop test results also reveal that the impact of the water entry can cause a certain initial rolling velocity, which may significantly impact the lateral displacement and then affect the final landing position. More detailed research on water entry of dropped contains should be part of future work but not the focus of this article.

The probability histogram from the experimental data provides an intuitive and direct distribution map following the existing specification (DNV, 2010), which has specific significance for discovering and salvaging containers. Finally, the results about probability per area will be helpful for risk management and risk area division during container loading and unloading.

For cylindrical objects, the standard state-space model in three-dimension(3D) has been successfully constructed. Based on the comparison between 2D theory and 3D theory, we further investigate the heave-pitch coupling term, which has been neglected in classical 2D theory before, and find that it can significantly affect the trajectory of dropped cylindrical objects.

Three different statistical methods, i.e., MC method, unscented method, and square-root Cubature method, are applied to analyze the stochastic behavior of the cylinders falling into the water. In general, the MC method is reliable under the premise of a large sample size. According to the case study above, the unscented method and square-root Cubature method give similar results to the MC method when the sample size is reasonable. 3D trajectory envelopes can be calculated based on the three methods above. It is concluded that the latter two methods can give similar results if compared to the MC method but with much less computation time. Although from the results, there is no difference between the unscented method and square-root Cubature method. However, compared to the unscented method, the fully automatic character of the square-root Cubature method reduces the difficulty of the operation. It reduces the operation time, making it more suitable for dynamic and real-time risk assessment of marine transportation and installation.

References

3D INSIDER, 2021. The 9 Different Types of 3D Printers. https://3dinsider.com/3d-printer-types/#sla (accessed July, 2021).

Aanesland, V., 1987. Numerical and experimental investigation of accidently falling drilling pipes. In: Offshore Technology Conference.

American Bureau of Shipping (ABS), 2013. Guidance Notes on Accidental Load Analysis and Design for Offshore Structures. USA.

American Bureau of Shipping (ABS), 2017. ABS Advisory on Additive Manufacturing. USA.

Ali, S., Oct. 2020, A Novel Dropped Object Risk Assessment Method for Offshore Operations. In: International Ocean and Polar Engineering Conference Shanghai, China

Alsos, H.S. and Faltinsen, O.M., 2018. 3D motion dynamics of axisymmetric bodies falling through water. Ocean Engineering, 169, pp.442-456.

Anderson, B.D.O., Moore, J.B., 1979. Optimal Filtering. Prentice Hall, Englewood Cliffs, NJ.

Arasaratnam, I. and Haykin, S., 2009. Cubature Kalman Filters, IEEE Transactions on Automatic Control, vol. 54, no. 6, pp. 1254-1269.

Arnold J., Do J. Y.N., Smith L. C., Poltavets V., Smith D. A., 2021. Extrusion of shrimp shell-polylactic acid composites: Dataset for the impact of surfactants on their morphology and thermal properties. Data in Brief, Volume 36, 107059, ISSN 2352-3409. https://doi.org/10.1016/j.dib.2021.107059.

Arnold, J., Sarkar K., Smith D., 2020. 3D printed bismuth oxide-polylactic acid composites for radio-mimetic computed tomography spine phantoms. Journal of biomedical materials research. Part B, Applied biomaterials. DOI: 10.1002/jbm.b.34744.

Awotahegn, M., 2014. Experimental Investigation of Accidental Drops of Drill Pipes and Containers. Master's thesis. University of Stavanger.

Baumers, M., Dickens, P., Tuck, C., Hague, R., 2016. The cost of additive manufacturing: machine productivity, economies of scale and technology-push, Technological Forecasting and Social Change, Volume 102, Pages 193-201, ISSN 0040-1625. https://doi.org/10.1016/j.techfore.2015.02.015.

Bernhofen, D. M., El-Sahli, Z., Kneller, R., 2015. Estimating the effects of the container revolution on world trade. Journal of International Economics. PII: S0022-1996(15)00140-3. DOI: 0.1016/j.jinteco.2015.09.001.

Chawa, P. K., Mukkamala, S. K., 2018. Design and Analysis of Shipping Container made of Honeycomb Sandwich Panels (Master thesis). Department of Mechanical Engineering, Blekinge Institute of Technology, Karlskrona, Sweden.

Chennakesava, P., Narayan, Y. S., 2014. Fused Deposition Modeling - Insights. International Conference on Advances in Design and Manufacturing (ICAD&M'14)

Chu, P.C., Gilles, A., Fan, C.W., 2005. Experiment of falling cylinder through the water column. Exp. Therm. Fluid Sci. 29, 555–568.

Colwill, A., Ahilan, A., 1992. Reliability analysis of the behavior of dropped objects. In: Offshore Technology Conference.

der Merwe, R.V., Wan, E.A., 2001. The square-root unscented kalman filter for state and parameter-estimation. In: IEEE International Conference on Acoustics, Speech, and Signal Processing. Proceedings, 2001.

Det Norske Veritas (DNV), 2010. DNV Recommended Practice: Risk Assessment of Pipeline Protection, DNV- RP- F107.

Ford, S., Despeisse, M., 2016. Additive manufacturing and sustainability: an exploratory study of the advantages and challenges. Journal of Cleaner Production. PII: S0959-6526(16)30439-5. DOI: 10.1016/j.jclepro.2016.04.150.

Franchetti, M., Kress, C., 2016. An economic analysis comparing the cost feasibility of replacing injection molding processes with emerging additive manufacturing techniques. Int J Adv Manuf Technol 88, 2573–2579. https://doi.org/10.1007/s00170-016-8968-7.

Frey, O. T., DeVogelaere, A. P., 2014. The Containerized Shipping Industry and the Phenomenon of Containers Lost at Sea. Marine Sanctuaries Conservation Series ONMS14-07. U.S. Department of Commerce, National Oceanic and Atmospheric Administration, Office of National Marine Sanctuaries, Silver Spring, MD. 51 pp.

Hoerner, S., 1965. Fluid-Dynamic Drag. Hoerner Fluid Dynamics.

Ingram J.G., Experimental Modelling and Risk Assessment of Dropped Offshore Tubulars, In: School of Industrial and Manufacturing Science, Cranfield Institute of Technology,1991

Ito, K., Xiong, K., May 2000. Gaussian filters for nonlinear filtering problems. IEEE Trans. Autom. Control 45 (5), 910–927.

Julier, S.J., Uhlmann, J.K., 1997. A consistent, debiased method for converting between polar and cartesian coordinate systems. In: Proceedings of SPIE Acquisition, Tracking, and Pointing XI, 3086.

Julier, S., Uhlmann, J., Durrant-Whyte, H.F., March 2000. A new method for the nonlinear transformation of means and covariances in filters and estimators. IEEE Trans. Autom. Control 45 (3), 477–482.

Katteland, L., Øygarden, B., 1995. Risk analysis of dropped objects for deep water development. In: The International Conference on Offshore Mechanics and Arctic Engineering. American Society of Mechanical Engineers, pp. 443–450.

Koh A., 2021. Shipping Containers Fall Overboard at Fastest Rate in Seven Years [WWW Document]. URL: https://www.bloomberg.com/news/articles/2021-04-26/shipping-containers-plunge-overboard-as-supply-race-raises-risks (accessed August, 2021).

Kozior, T., Kundera, C., 2017. Evaluation of the Influence of Parameters of FDM Technology on the Selected Mechanical Properties of Models. Procedia Engineering, Volume 192, Pages 463-468, ISSN 1877-7058, https://doi.org/10.1016/j.proeng.2017.06.080.

Luo, Y., Davis, J., 1992. Motion simulation and hazard assessment of dropped objects. In: International Offshore and Polar Engineering Conference.

Mendel, J.M., 1995. In: Oppenheim, A.V. (Ed.), Lessons in Estimation Theory for Signal Processing, Communications, and Control, second ed. Prentice Hall, Mar.

Menegaz, H.M.T., Ishihara, J.Y., Borges, G.A., Vargas, A.N., Oct. 2015. A systematization of the unscented Kalman filter theory. IEEE Trans. Autom. Control 60, 2583–2598.

Meng, H., Li, X.R., Jilkov, V.P., jul 2018. Optimized Gauss-Hermite quadrature with application to nonlinear filtering. In: 2018 21st International Conference on Information Fusion (FUSION). IEEE.

Milewski, J. O., 2017. Additive Manufacturing of Metals from Fundamental Technology to Rocket Nozzles, Medical Implants, and Custom Jewelry. Springer Series in Materials Science, Volume 258.

Mood, A.M., Graybill, F.A., Boes, D.C., 1974. Introduction to the Theory of Statistics, Ser. McGraw-Hill Series in Probability and Statistics. McGraw-Hill Companies.

Newman, J.N., 1977. Marine Hydrodynamics. The MIT Press.

Ngo T. D., Kashani A., Imbalzano G., Nguyen K. T.Q., Hui D., 2018. Additive manufacturing (3D printing): A review of materials, methods, applications and challenges. Composites Part B: Engineering, Volume 143, Pages 172-196, ISSN 1359-8368. https://doi.org/10.1016/j.compositesb.2018.02.012.

Odian G., 2004. Principles of Polymerization, Fourth Edition. College of Staten Island, City University of New York, Staten Island, New York. Print ISBN: 9780471274001, online ISBN: 9780471478751, DOI: 10.1002/047147875X

Schlichting, H., 1979. Boundary Layer Theory. McGraw-Hill Book Company.

Stratasys F170 Protocol, 2020. UC Berkeley Mechanical Engineering. URL: https://me.berkeley.edu/wp-content/uploads/2020/07/Stratasys-f170-Protocol.pdf (accessed August, 2021)

Varotsis A. B., 2021. Introduction to FDM 3D printing [WWW Document]. URL: https://www.hubs.com/knowledge-base/introduction-fdm-3d-printing/#characteristics (accessed August, 2021).

Wan, E., Merwe, R.V.D., Oct. 2000. The unscented kalman filter for nonlinear estimation. In: Proceedings of the IEEE 2000 Adaptive Systems for Signal Processing, Communications, and Control Symposium. Wasalaski, R. G. Oct. 2021. Probable Causes of Losses of Containers from Container Ships. In SNAME Maritime Convention. OnePetro.

Xiang, G., Birk, L., Li, L., Yu, X., Luo, Y., 2016. Risk free zone study for cylindrical objects dropped into water. Ocean Syst. Eng. 6 (4), 377–400.

Xiang, G., Birk, L., Yu, X., Lu, H., 2017. Numerical study on the trajectory of dropped cylindrical objects. Ocean Eng. 130, 1–9.

Xiang, G., Birk, L., Yu, X., Li, X., 2017. Study on the trajectory and landing points of dropped cylindrical object with different longitudinal center of gravity. Int. J. Offshore Polar Eng. 27 (3), 274–282.

Xiang, G., Li, X., Yu, X., Luo, Y., Cao, Y., feb 2019. Motion dynamics of dropped cylindrical objects in flows after water entry. Ocean Eng. 173, 659–671.

Xiang, G., Xiang, X.B. 2021. “3D trajectory optimization of the slender body freely falling through water using cuckoo search algorithm”. Ocean Eng., 235,109354. doi:10.1016/j.oceaneng.2021.109354.

Yasseri, S., 2014. Experiment of free-falling cylinders in water. Underw. Technol. 32 (2), 177–191.

Yu, X., Li, L., Xiong, Z. and Kang, S., 2020a. Hit Probability of Cylindrical Objects Dropped on pipelines in Offshore Operations, Journal of Pipeline Systems - Engineering and Practice, 11(4): 04020048.

Yu, X., Meng, H., Zhen, Y. and Li, L., 2019. Trajectory Prediction of Cylinders Freely Dropped into Water in Two Dimensions based on State Space Model, Ocean Engineering, Vol. 187, 106154.

Yu, X., Xiang, G., Collopy, H. and Kong, X., 2020b. Trajectory tracking of a model rocket falling into the towing tank: experimental tests versus numerical simulations. Journal of Aerospace Engineering, 33(5): 04020056.

Appendix

In the following figures, we show the 3D envelopes obtained by the square- root Cubature method at 30°, 45°, 60° drop angles and compare these envelopes with the experimental envelopes of Aanesland (1987). In practical engineering applications, the confidence coefficient α can be adjusted according to actual needs, so that the search process has a better trade-off between search efficiency and economy.

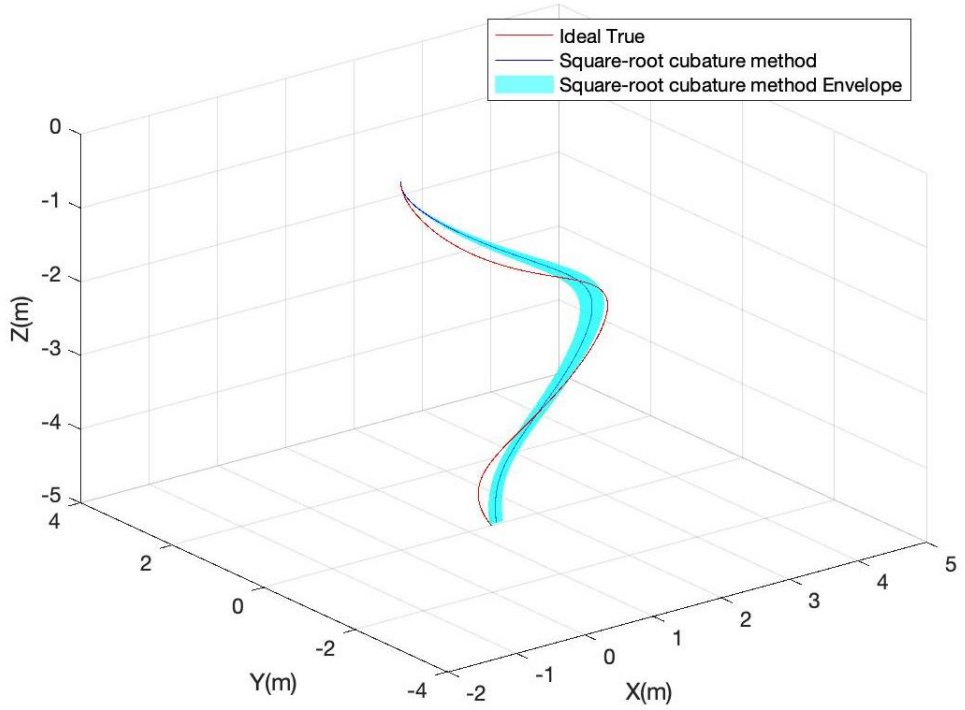

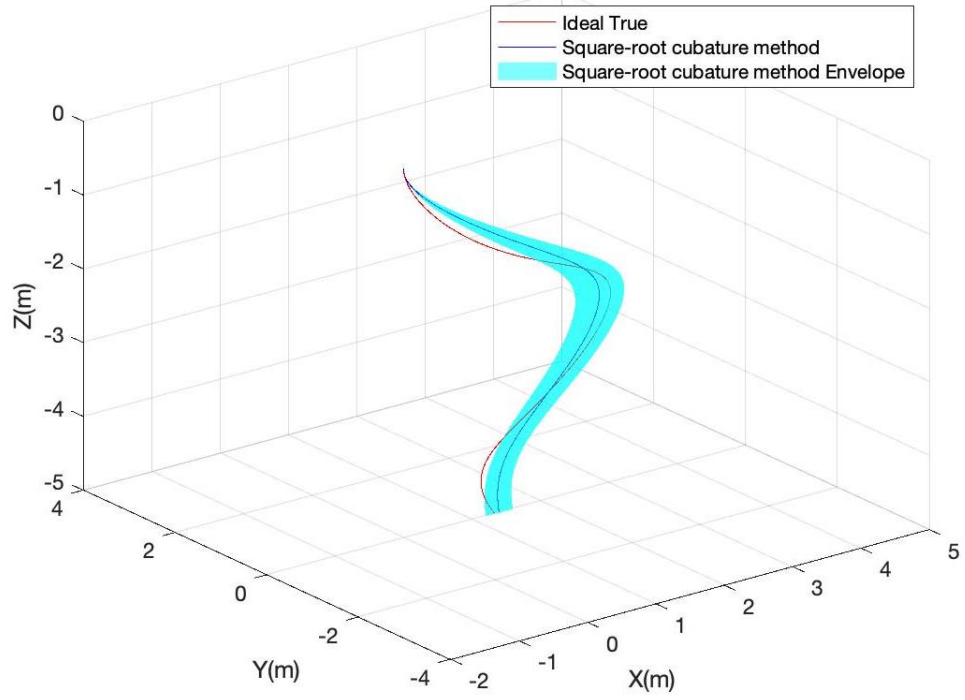

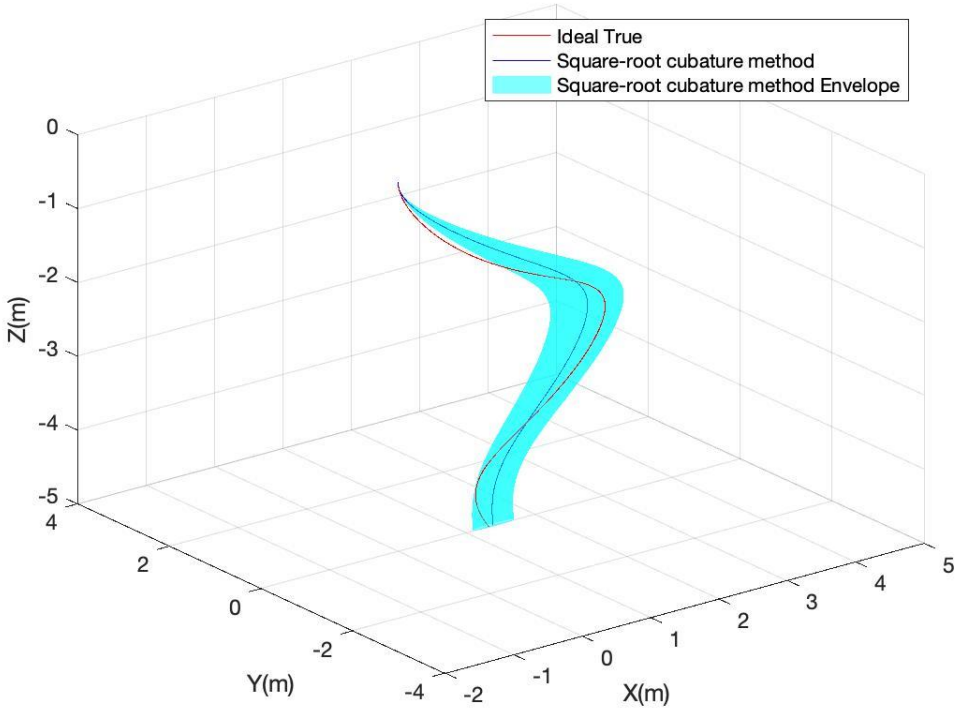
Ideal True
Square-root cubature method
Square-root cubature method Envelope
Z(m)
0
-1
-2
-3
-4
-5
Y(m)
4
2
0
-2
-4
X(m)
-2
-1
0
1
2
3
4
5

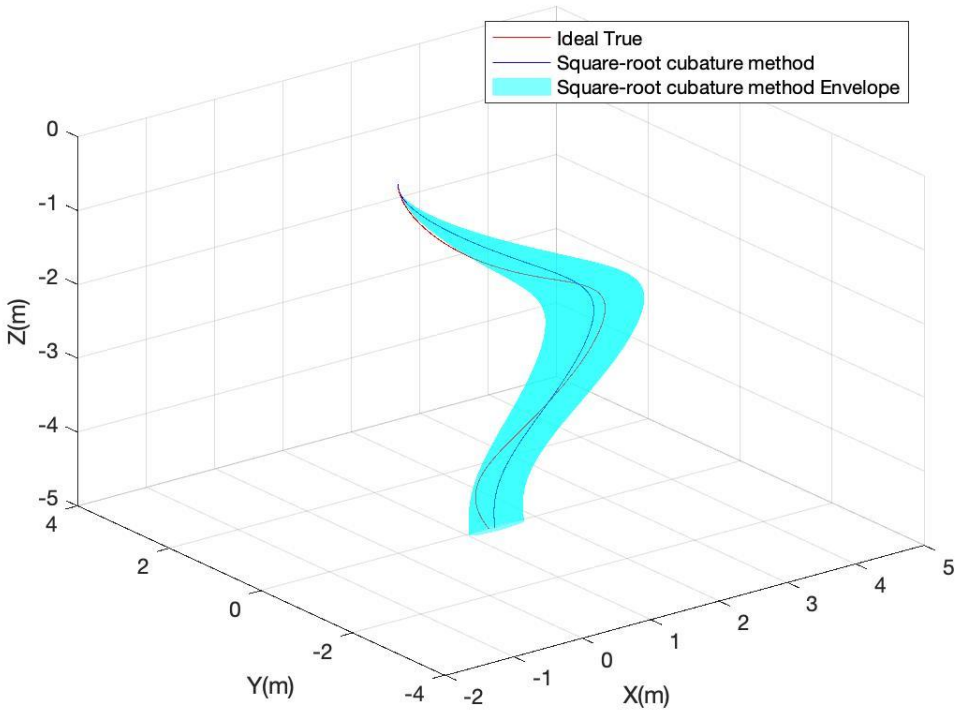
Ideal True
Square-root cubature method
Square-root cubature method Envelope
Z(m)
0
-1
-2
-3
-4
-5
Y(m)
4
2
0
-2
-4
X(m)
-2
-1
0
1
2
3
4
5

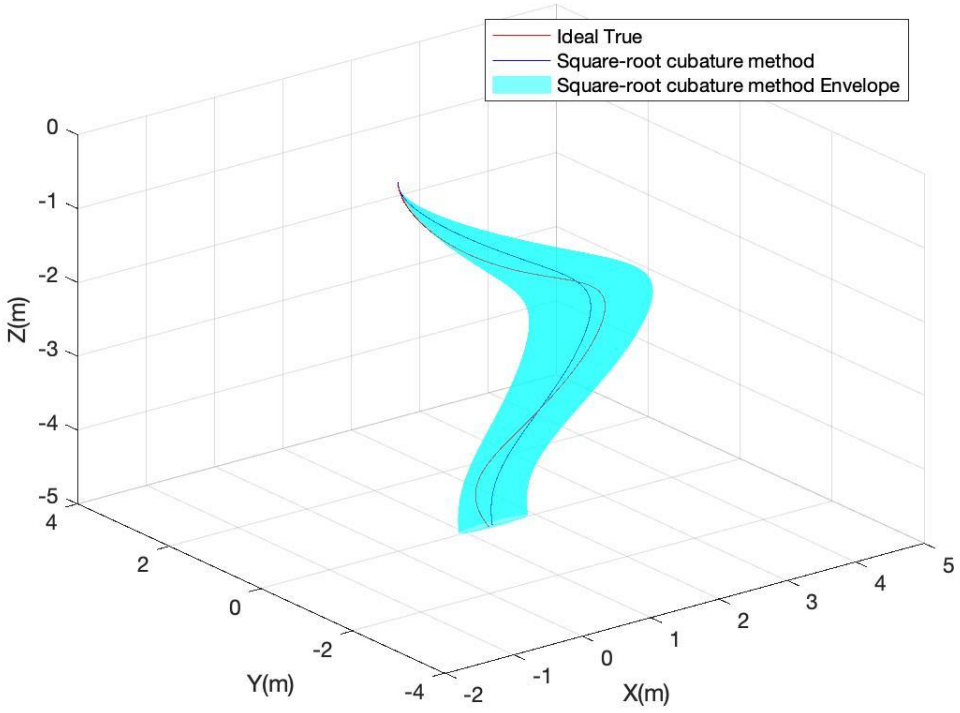
Ideal True
Square-root cubature method
Square-root cubature method Envelope
Z(m)
0
-1
-2
-3
-4
-5
Y(m)
4
2
0
-2
-4
X(m)
-2
-1
0
1
2
3
4
5

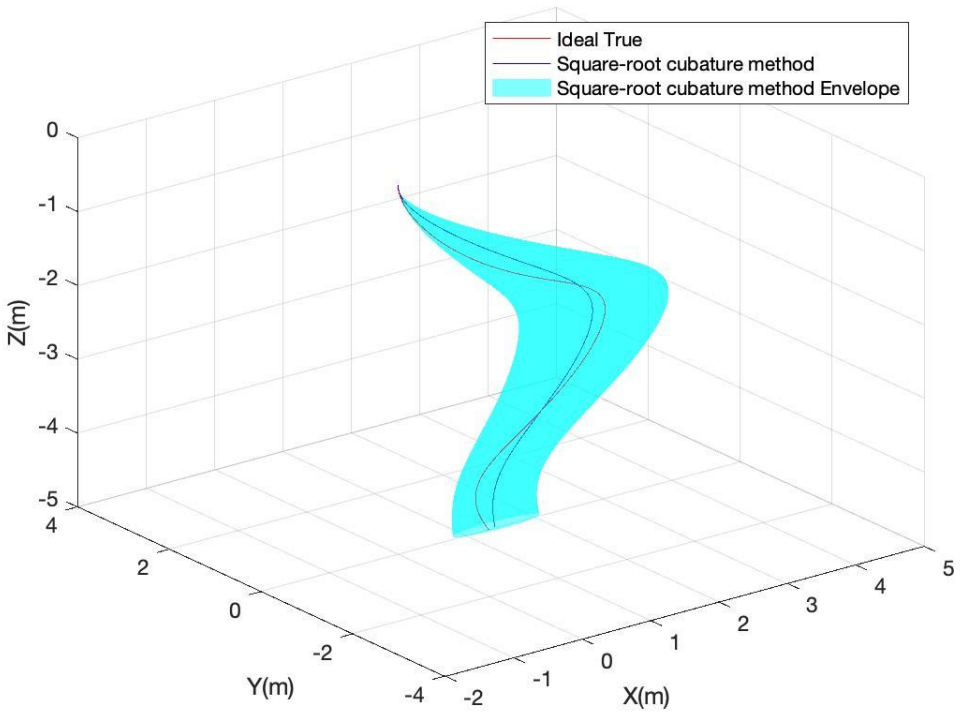
Ideal True
Square-root cubature method
Square-root cubature method Envelope
Z(m)
0
-1
-2
-3
-4
-5
Y(m)
4
2
0
-2
-4
X(m)
-2
-1
0
1
2
3
4
5

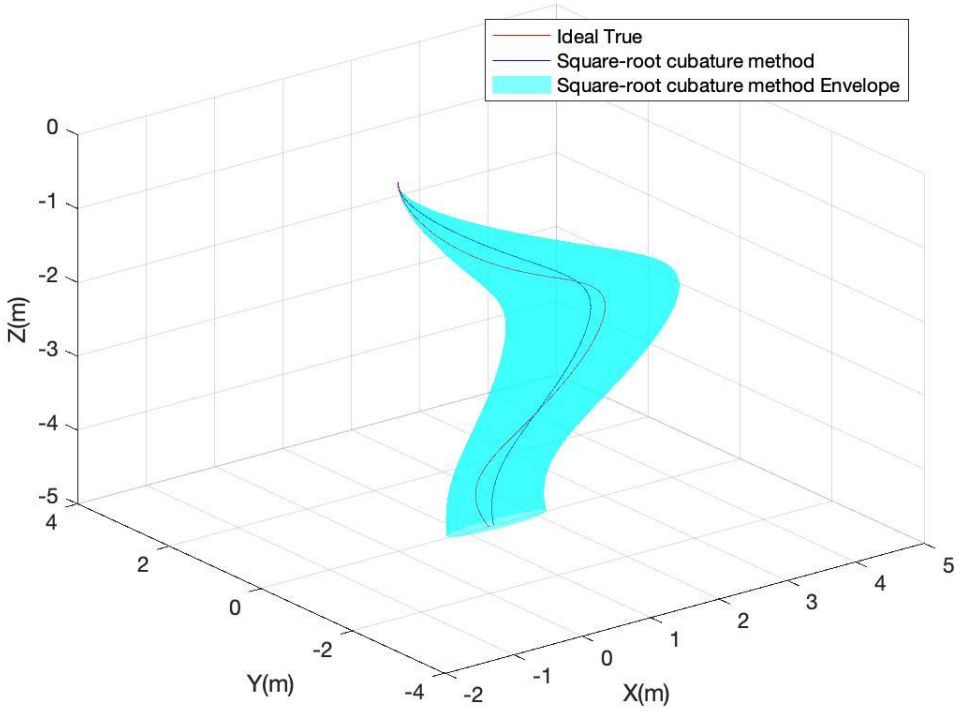
Ideal True
Square-root cubature method
Square-root cubature method Envelope
Z(m)
0
-1
-2
-3
-4
-5
Y(m)
4
2
0
-2
-4
X(m)
-2
-1
0
1
2
3
4
5

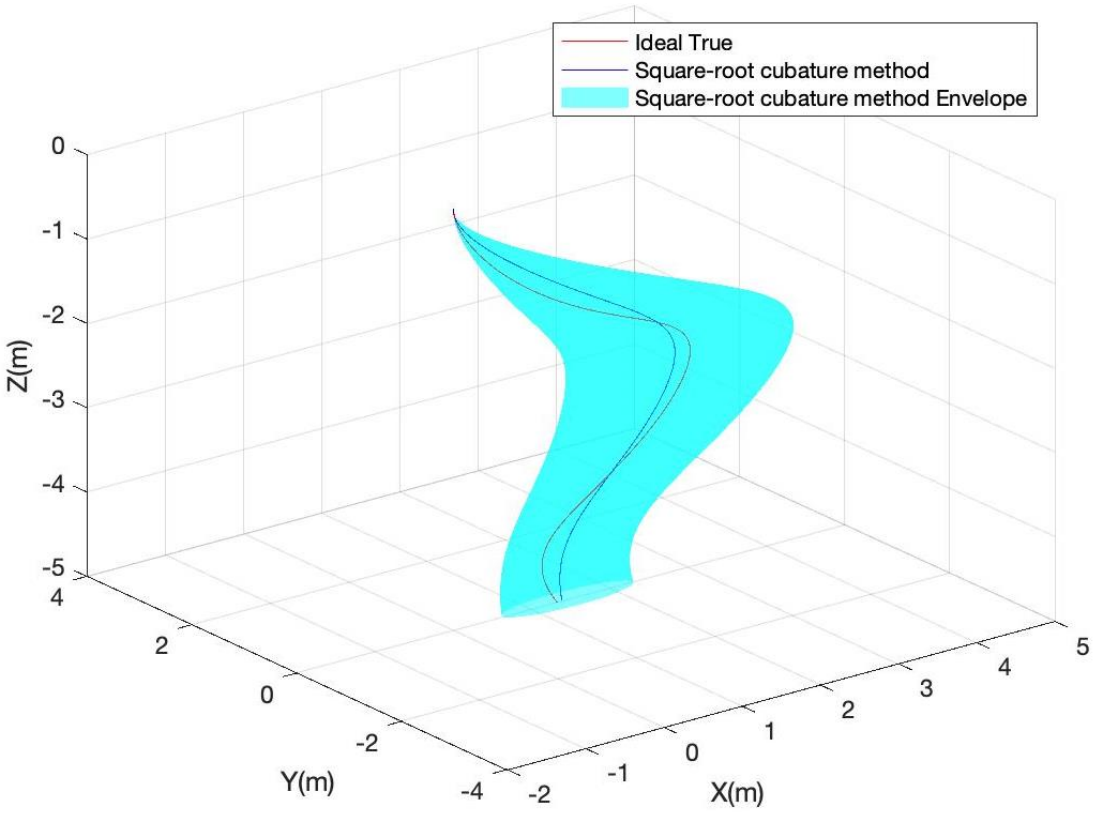
Ideal True
Square-root cubature method
Square-root cubature method Envelope
Z(m)
0
-1
-2
-3
-4
-5
Y(m)
4
2
0
-2
-4
X(m)
-2
-1
0
1
2
3
4
5

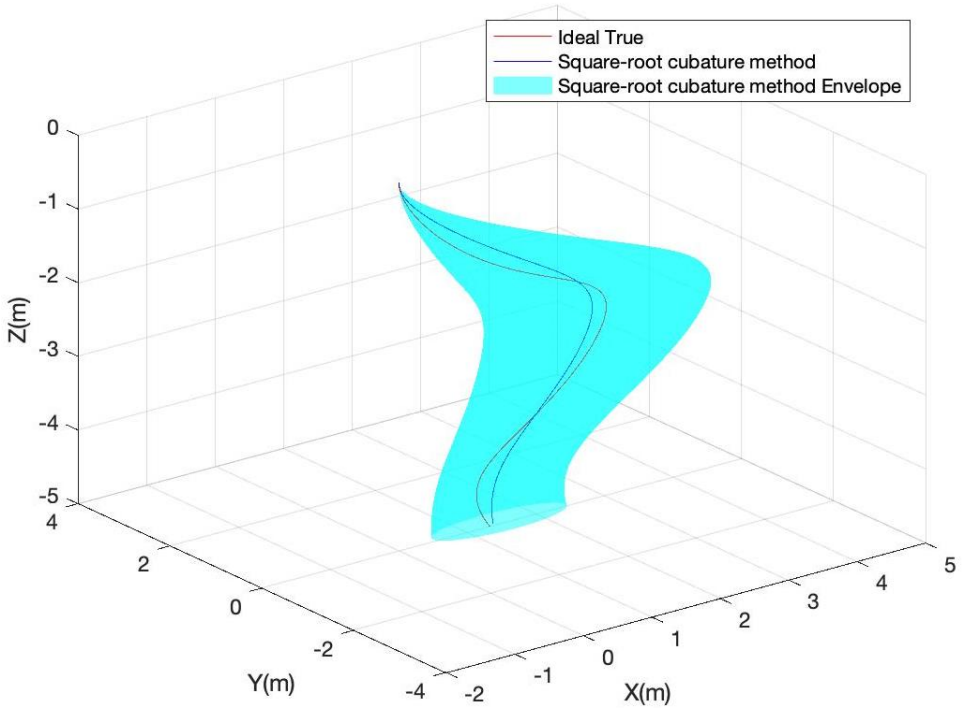

Figure A.1 Trajectory prediction at the drop angle 30° using square-root Cubature method in 3D (α =0.1-0.9)

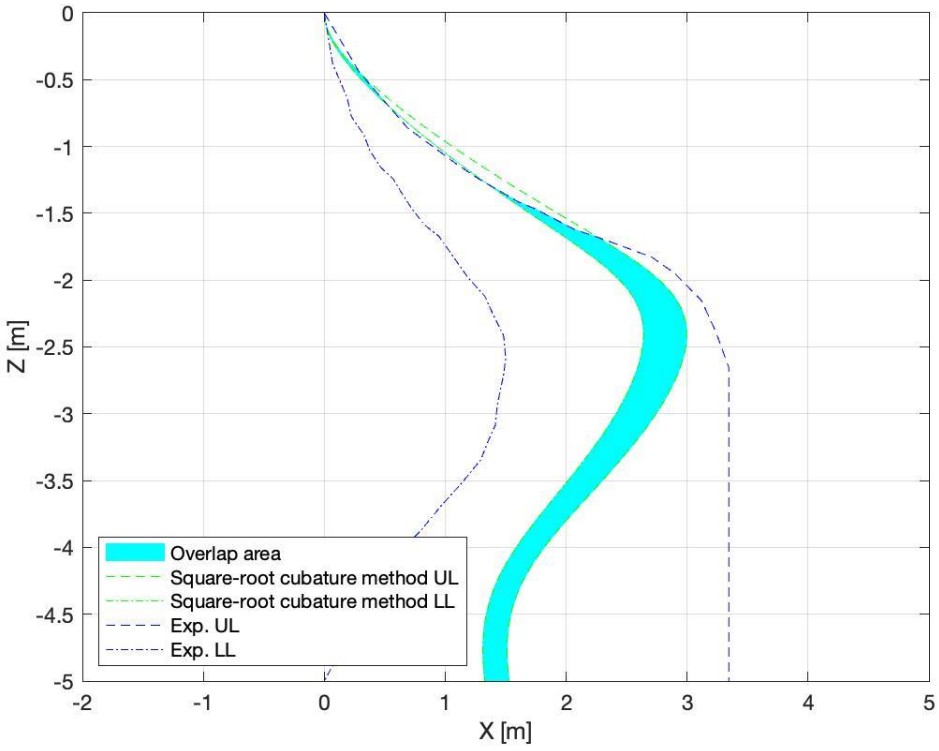
Z [m]
X [m]
Overlap area
Square-root cubature method UL
Square-root cubature method LL
Exp. UL
Exp. LL

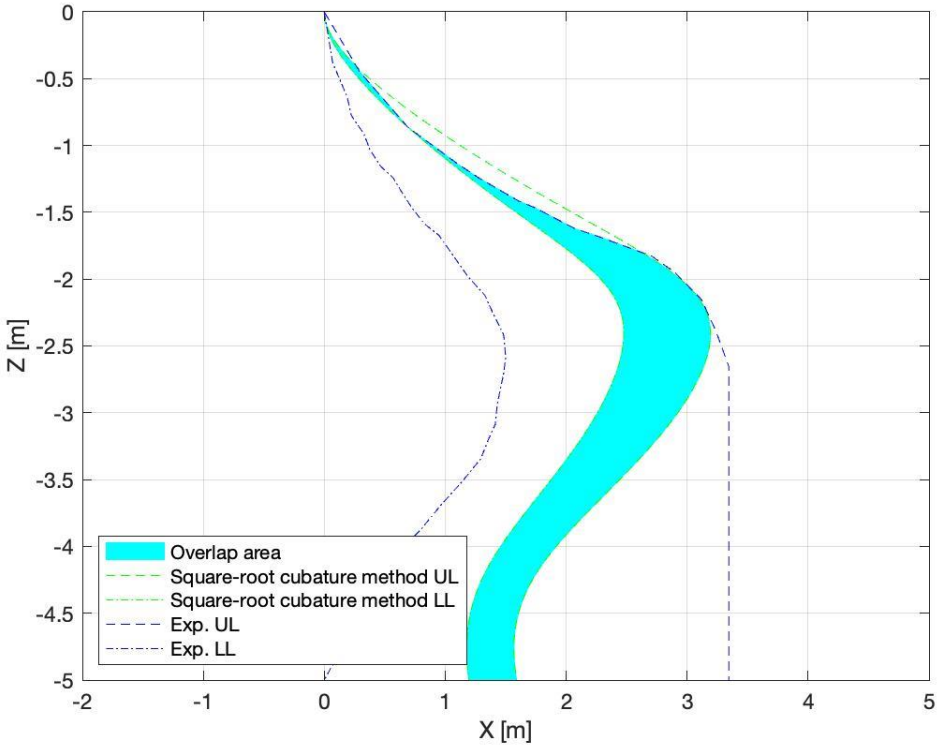
Z [m]
X [m]
Overlap area
Square-root cubature method UL
Square-root cubature method LL
Exp. UL
Exp. LL

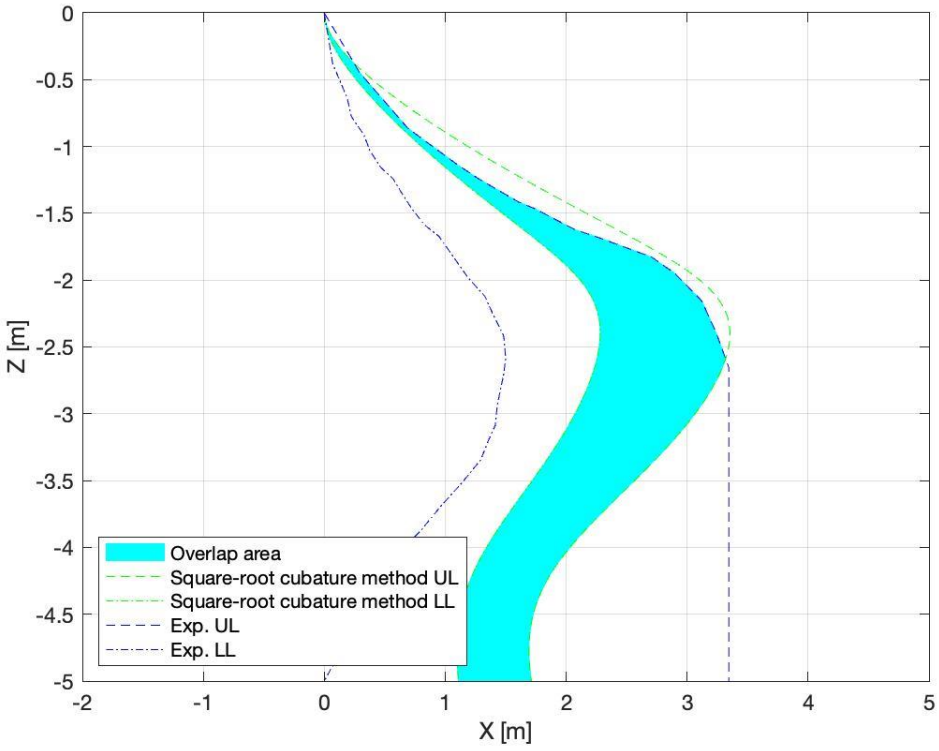
Z [m]
X [m]
Overlap area
Square-root cubature method UL
Square-root cubature method LL
Exp. UL
Exp. LL

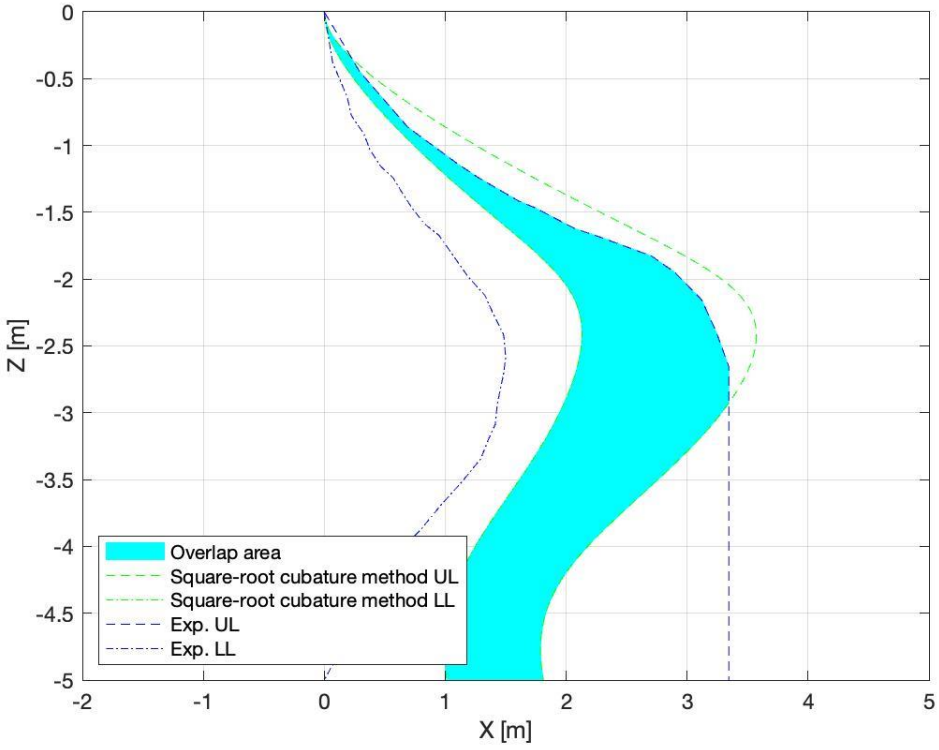
Z [m]
X [m]
Overlap area
Square-root cubature method UL
Square-root cubature method LL
Exp. UL
Exp. LL

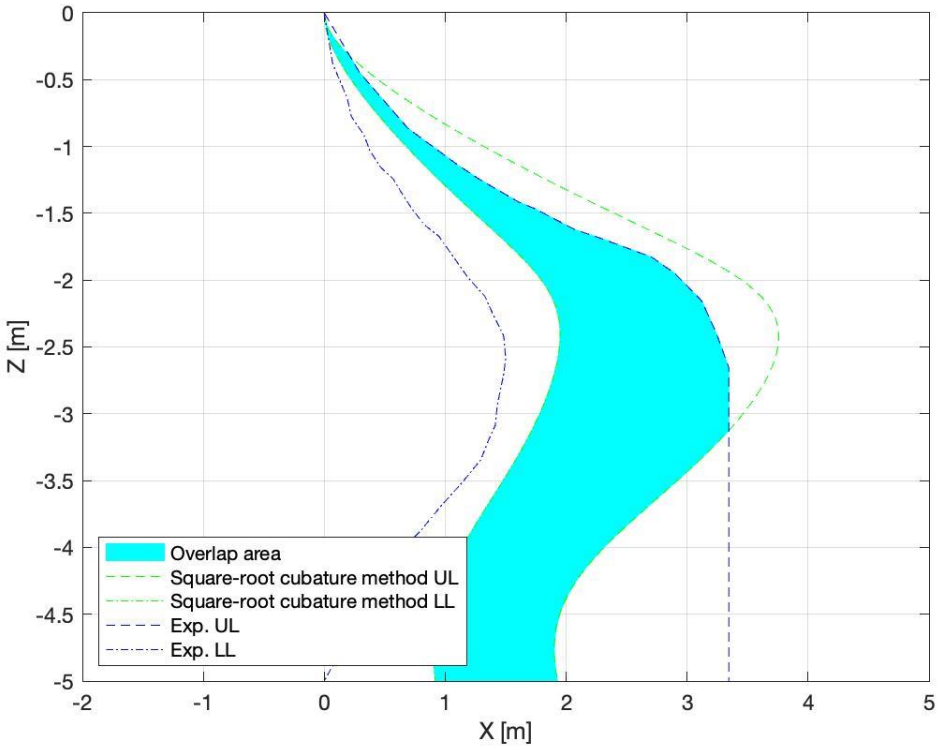
Z [m]
X [m]
Overlap area
Square-root cubature method UL
Square-root cubature method LL
Exp. UL
Exp. LL

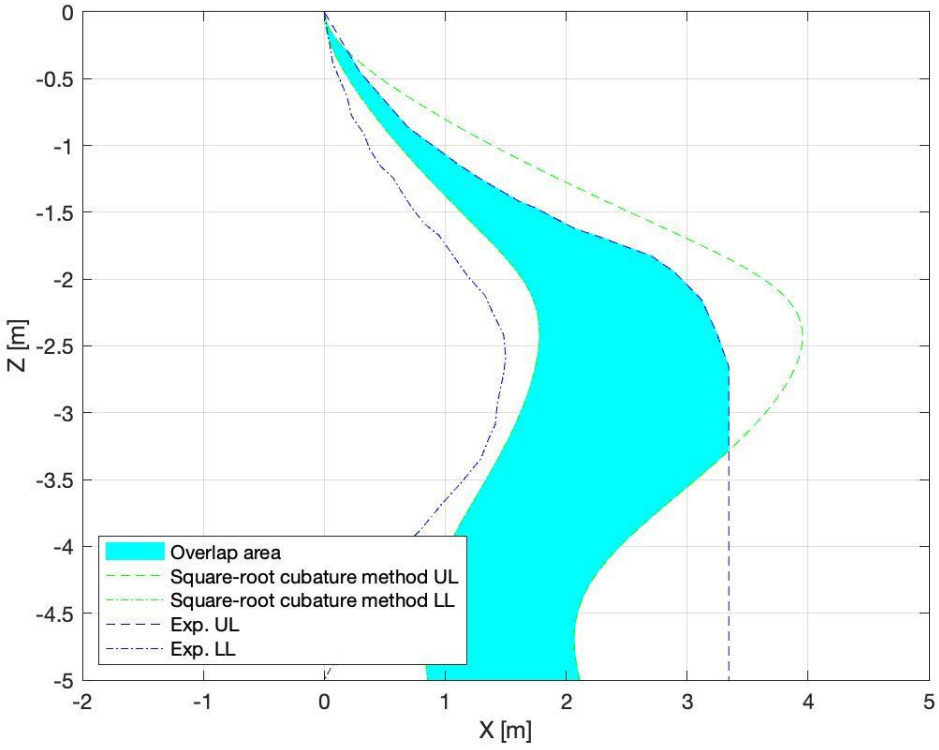
Z [m]
X [m]
Overlap area
Square-root cubature method UL
Square-root cubature method LL
Exp. UL
Exp. LL

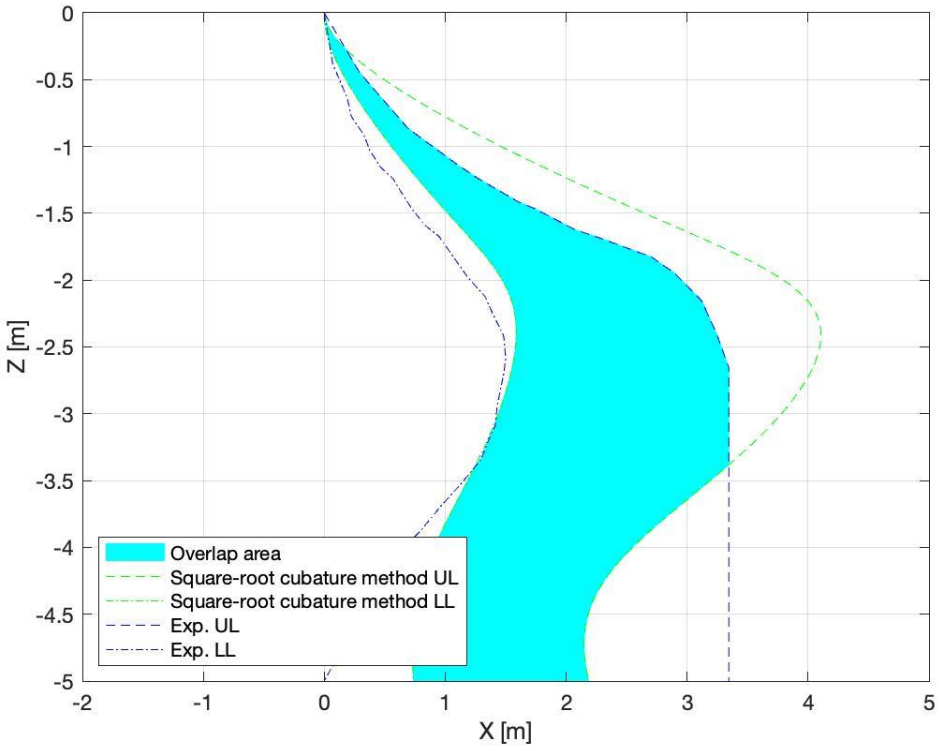
Z [m]
X [m]
Overlap area
Square-root cubature method UL
Square-root cubature method LL
Exp. UL
Exp. LL

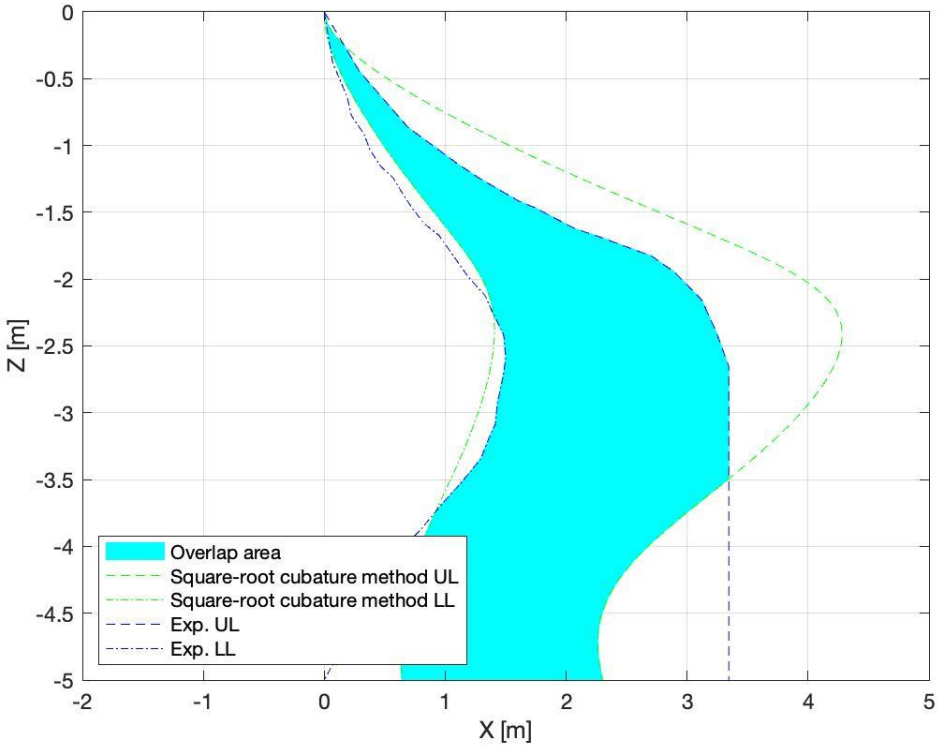
Z [m]
X [m]
Overlap area
Square-root cubature method UL
Square-root cubature method LL
Exp. UL
Exp. LL

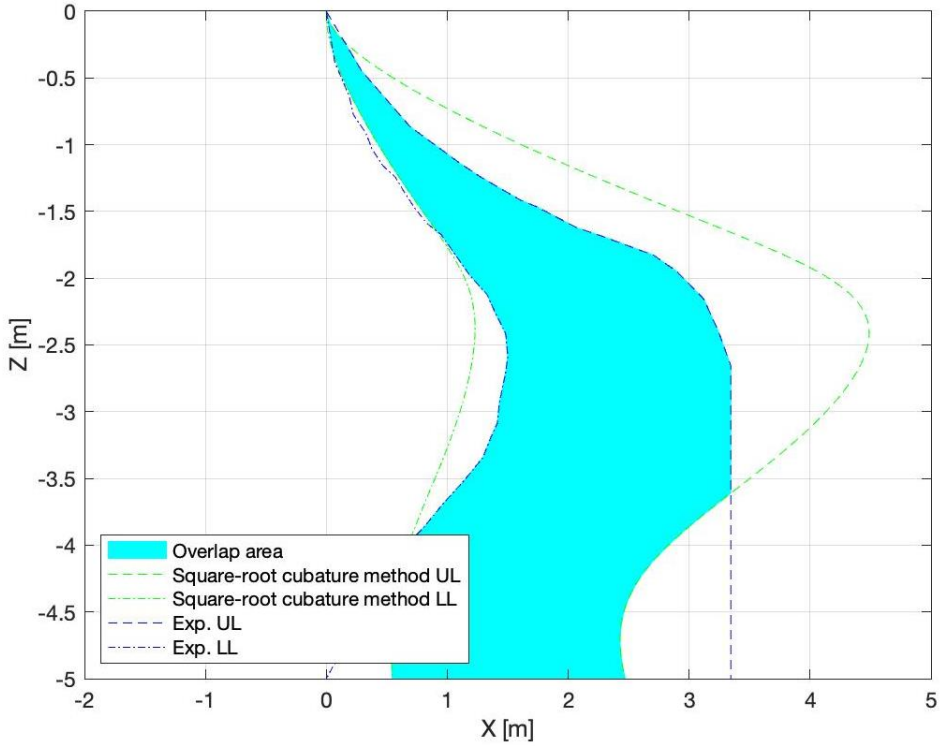

Figure A.2 Overlap area between square-root Cubature method and experimental envelope with the drop angle 30° in 3D (α =0.1-0.9)

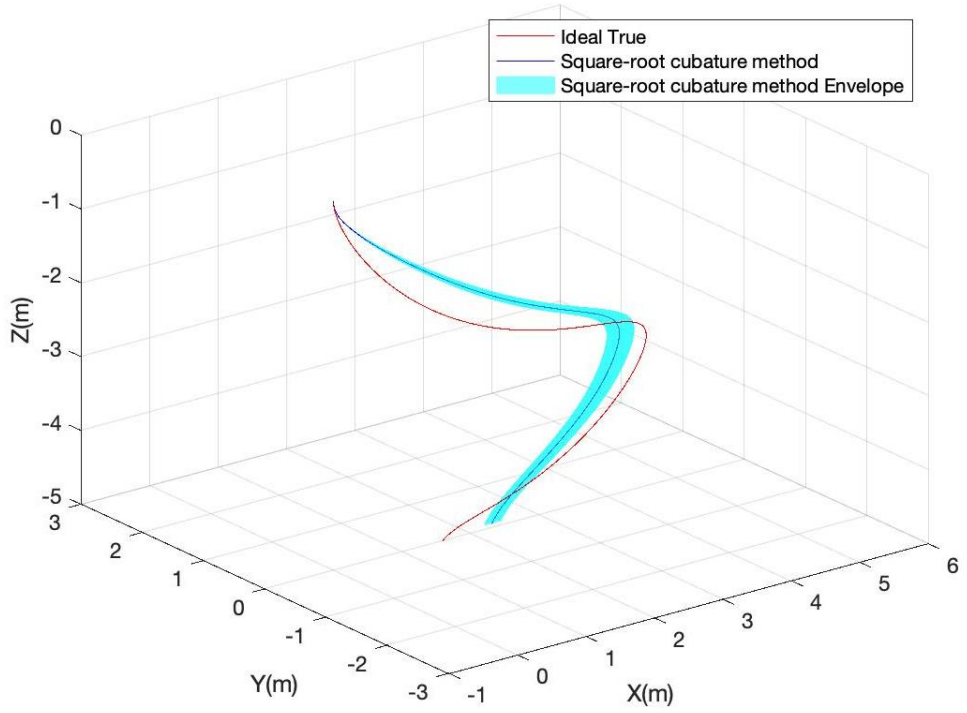

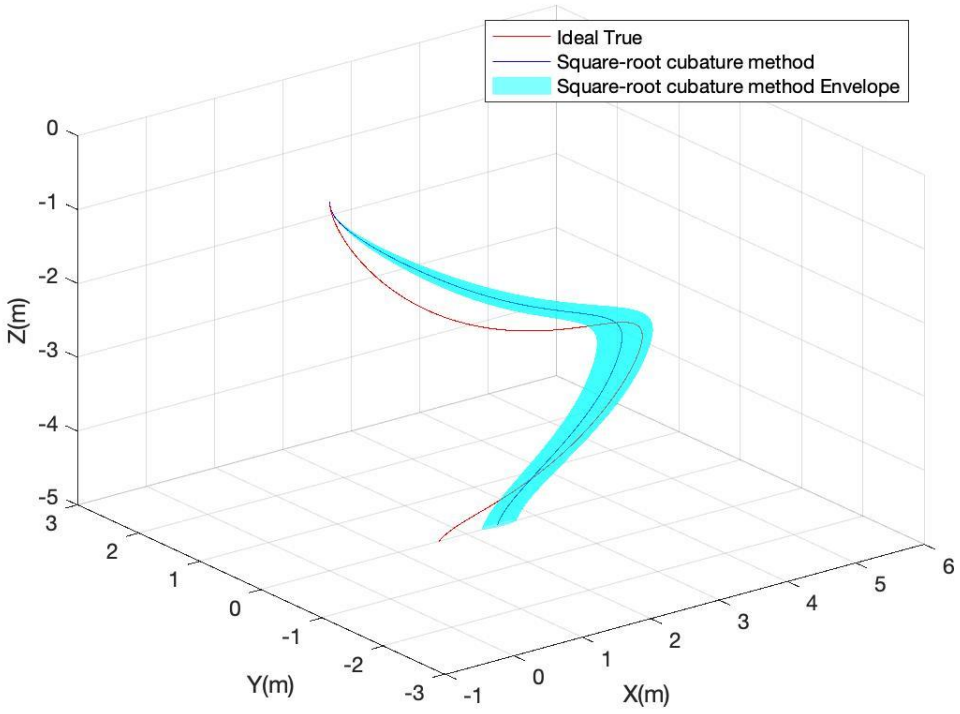
Ideal True
Square-root cubature method
Square-root cubature method Envelope
Z(m)
0
-1
-2
-3
-4
-5
Y(m)
3
2
1
0
-1
-2
-3
X(m)
-1
0
1
2
3
4
5
6

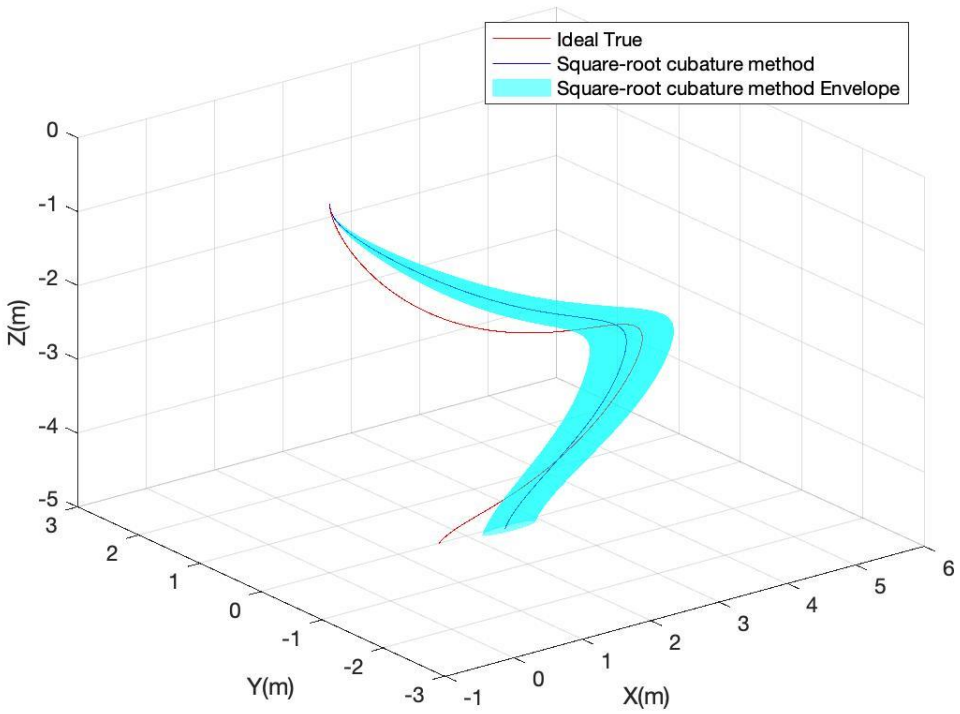
Ideal True
Square-root cubature method
Square-root cubature method Envelope
Z(m)
0
-1
-2
-3
-4
-5
Y(m)
3
2
1
0
-1
-2
-3
X(m)
-1
0
1
2
3
4
5
6

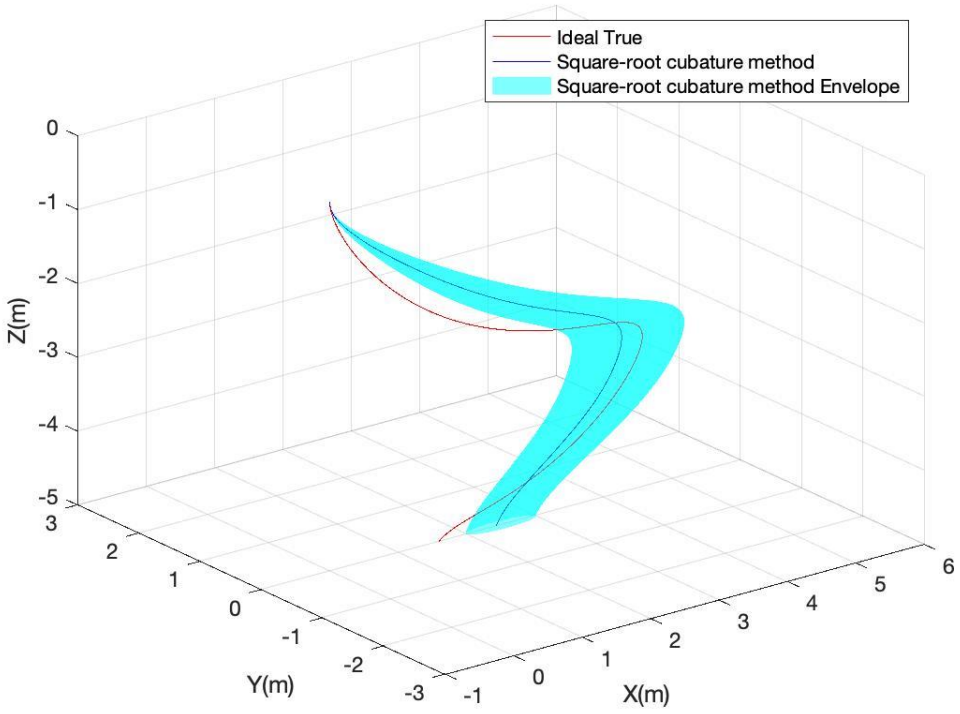
Ideal True
Square-root cubature method
Square-root cubature method Envelope
Z(m)
0
-1
-2
-3
-4
-5
Y(m)
3
2
1
0
-1
-2
-3
X(m)
-1
0
1
2
3
4
5
6

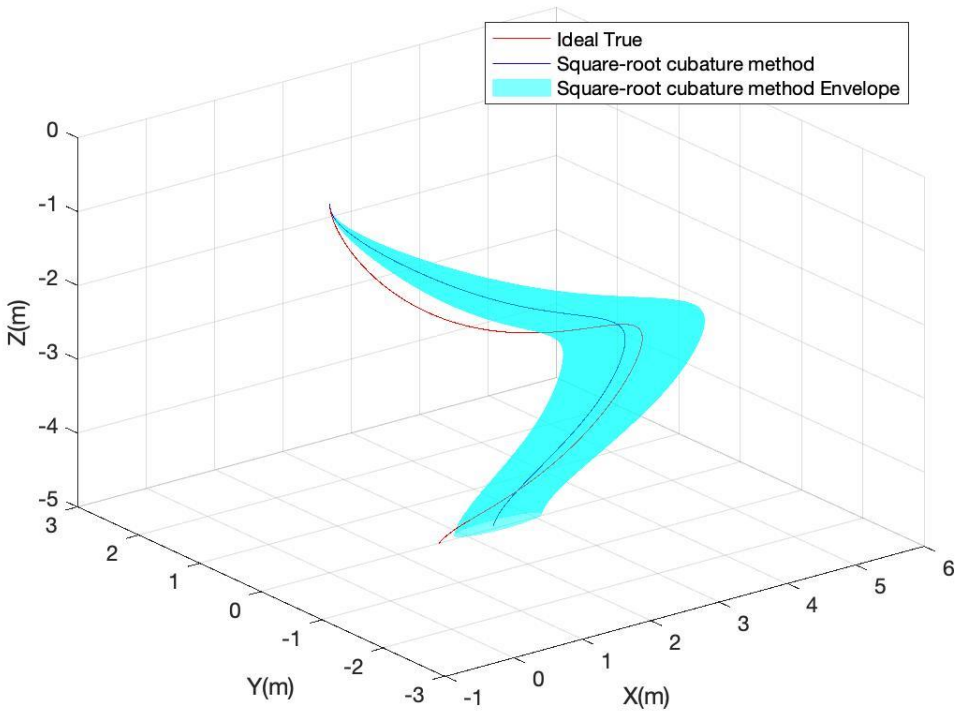
Ideal True
Square-root cubature method
Square-root cubature method Envelope
Z(m)
0
-1
-2
-3
-4
-5
Y(m)
3
2
1
0
-1
-2
-3
X(m)
-1
0
1
2
3
4
5
6

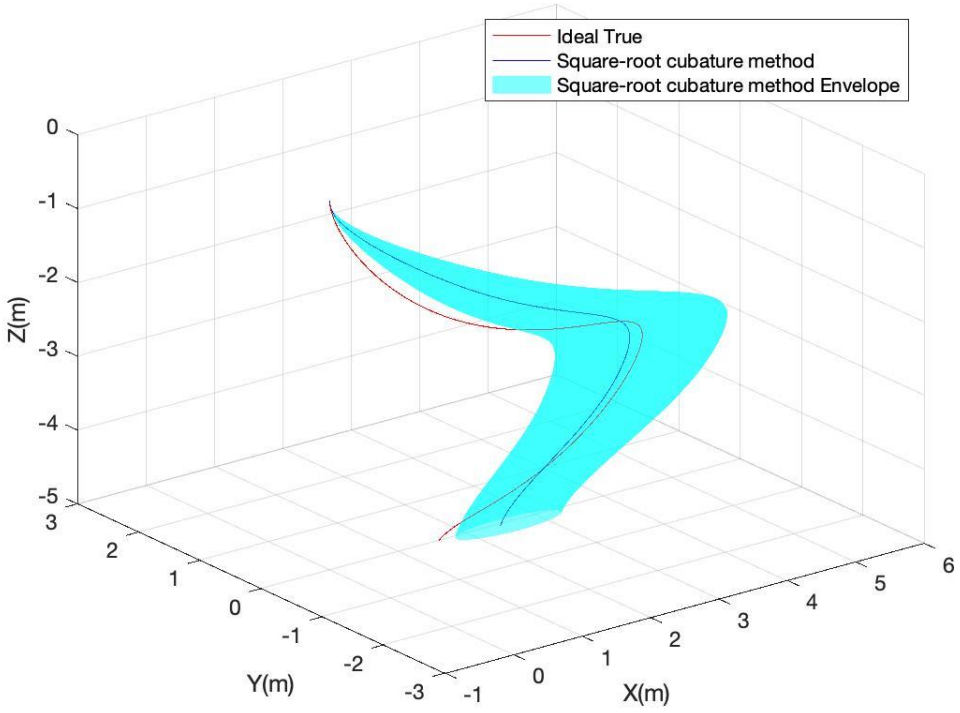
Ideal True
Square-root cubature method
Square-root cubature method Envelope
Z(m)
0
-1
-2
-3
-4
-5
Y(m)
3
2
1
0
-1
-2
-3
X(m)
-1
0
1
2
3
4
5
6

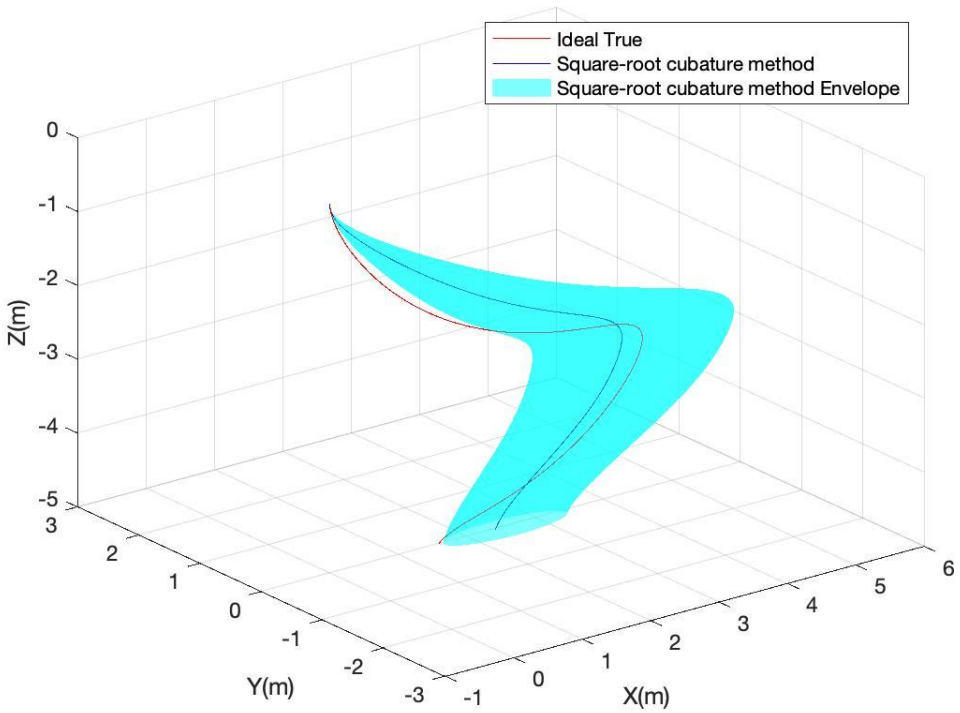
Ideal True
Square-root cubature method
Square-root cubature method Envelope
Z(m)
0
-1
-2
-3
-4
-5
Y(m)
3
2
1
0
-1
-2
-3
X(m)
-1
0
1
2
3
4
5
6

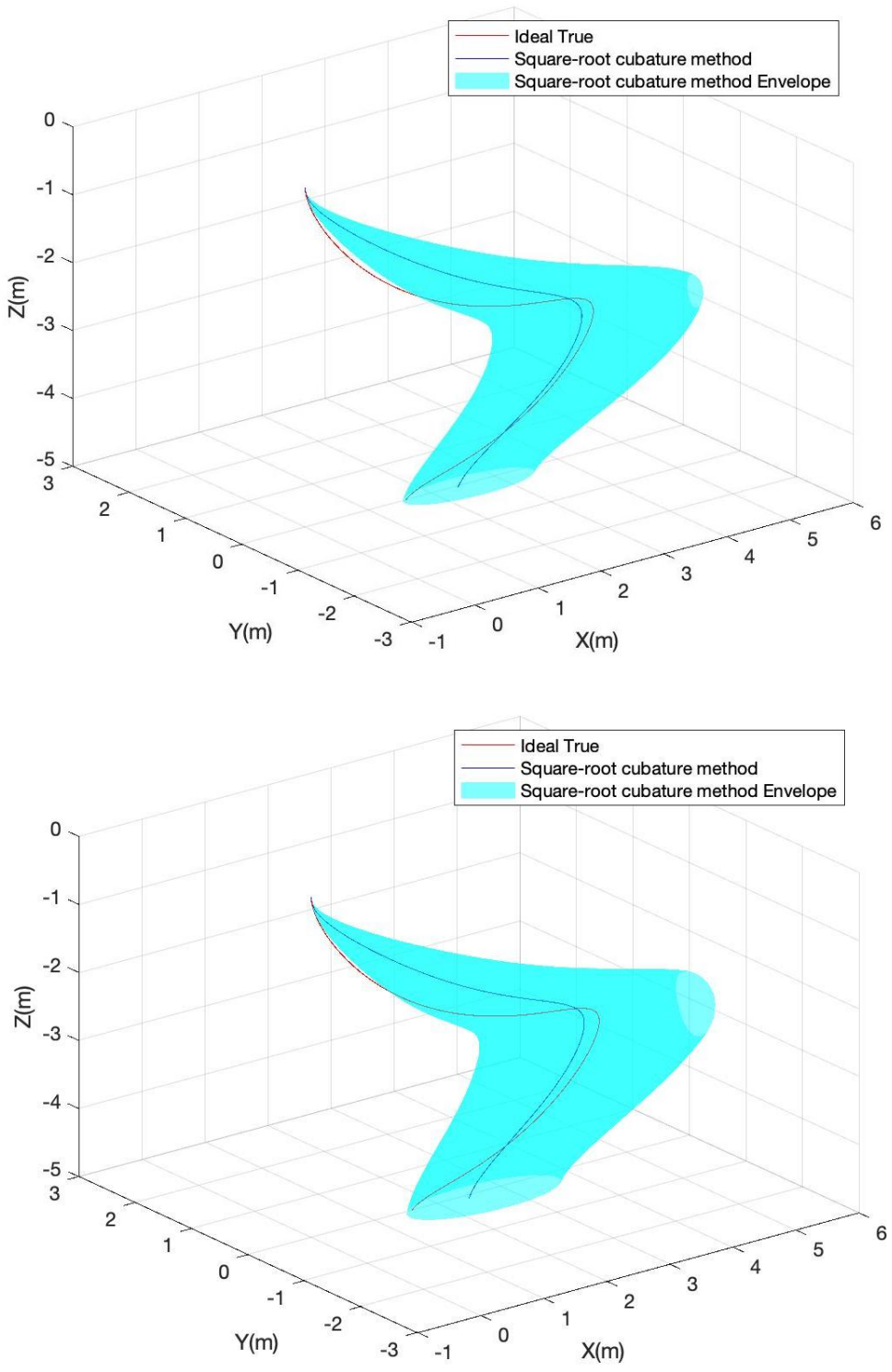

Figure A.3 Trajectory prediction at the drop angle 45° using square-root Cubature method in 3D (α =0.1-0.9)

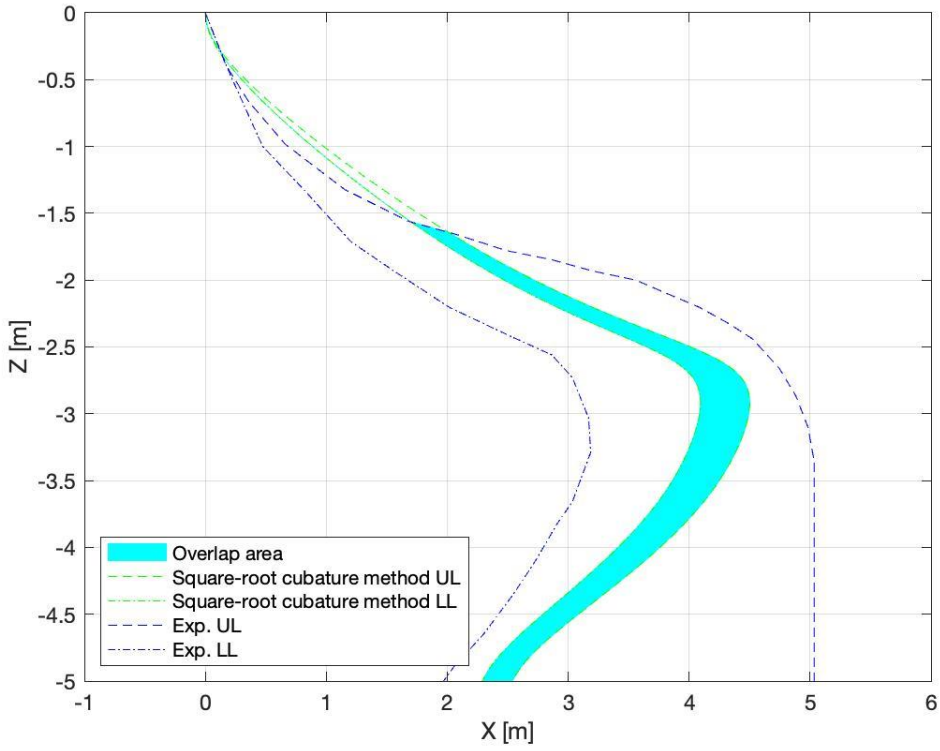
Z [m]
X [m]
Overlap area
Square-root cubature method UL
Square-root cubature method LL
Exp. UL
Exp. LL

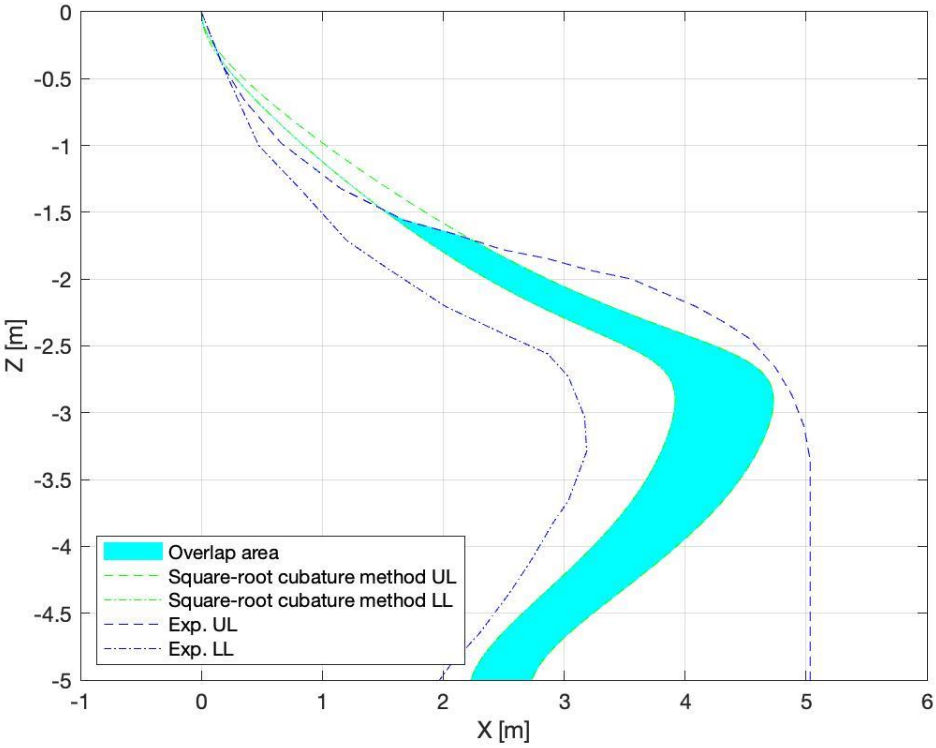
Z [m]
X [m]
Overlap area
Square-root cubature method UL
Square-root cubature method LL
Exp. UL
Exp. LL

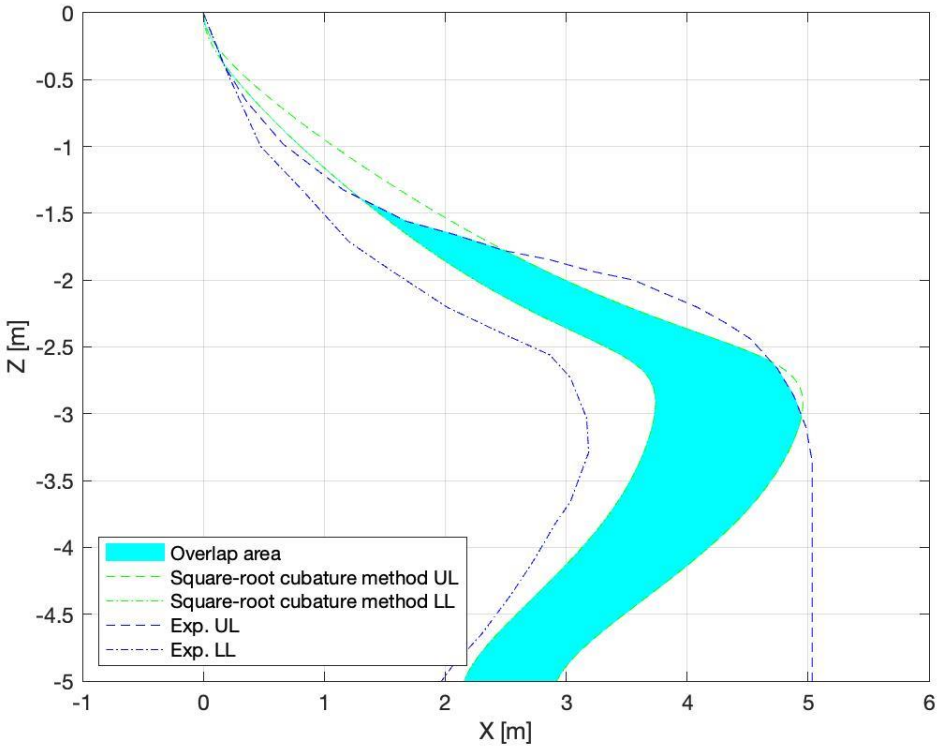
Z [m]
X [m]
Overlap area
Square-root cubature method UL
Square-root cubature method LL
Exp. UL
Exp. LL

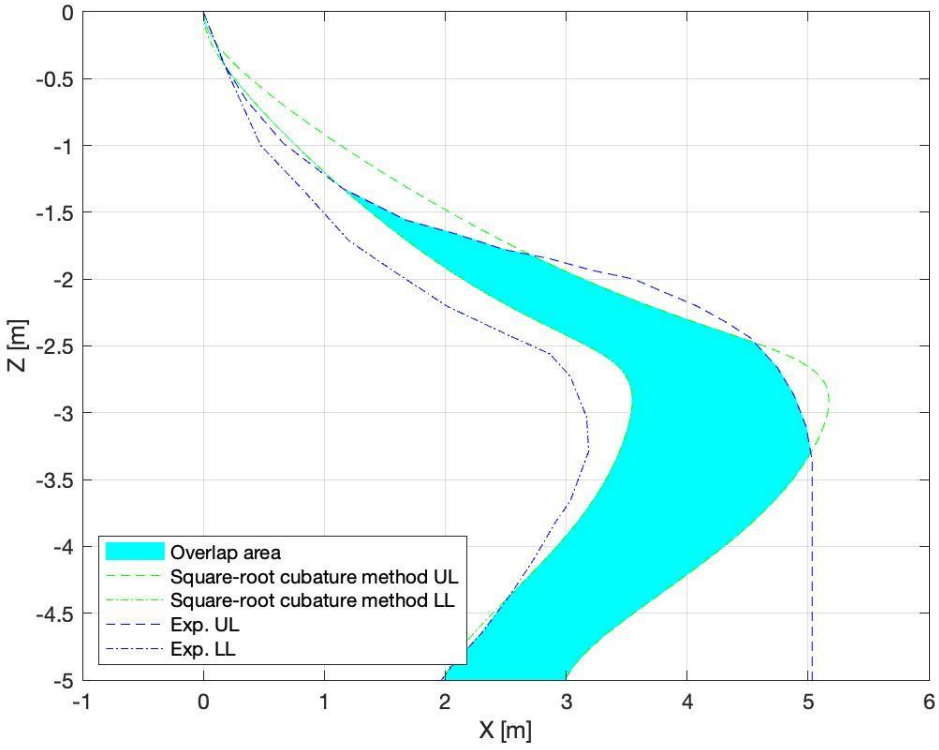
Z [m]
X [m]
Overlap area
Square-root cubature method UL
Square-root cubature method LL
Exp. UL
Exp. LL

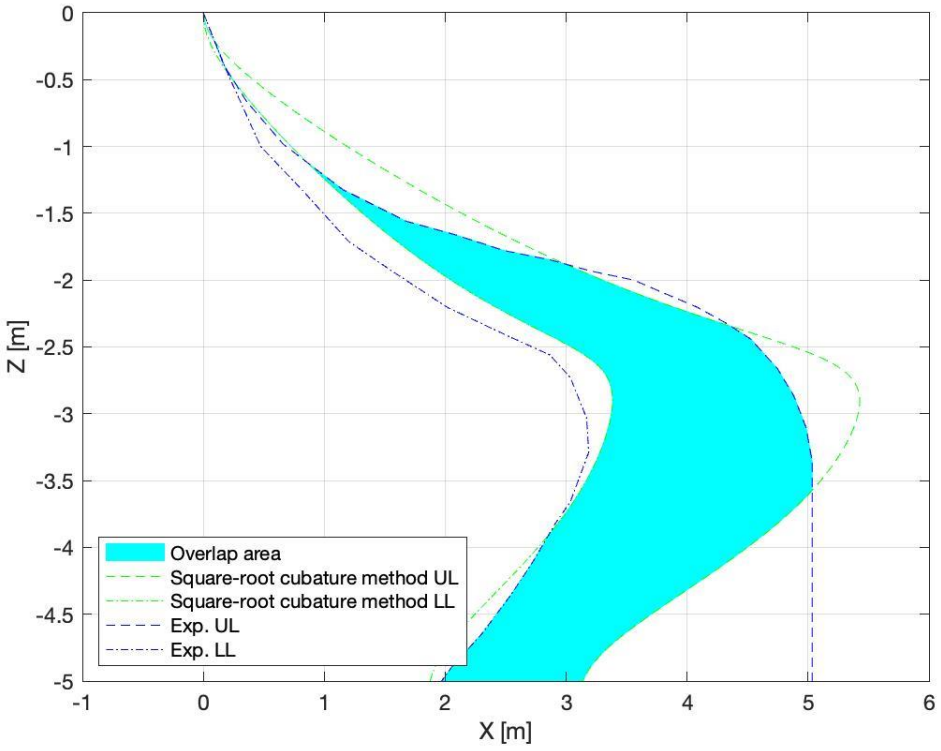
Z [m]
X [m]
Overlap area
Square-root cubature method UL
Square-root cubature method LL
Exp. UL
Exp. LL

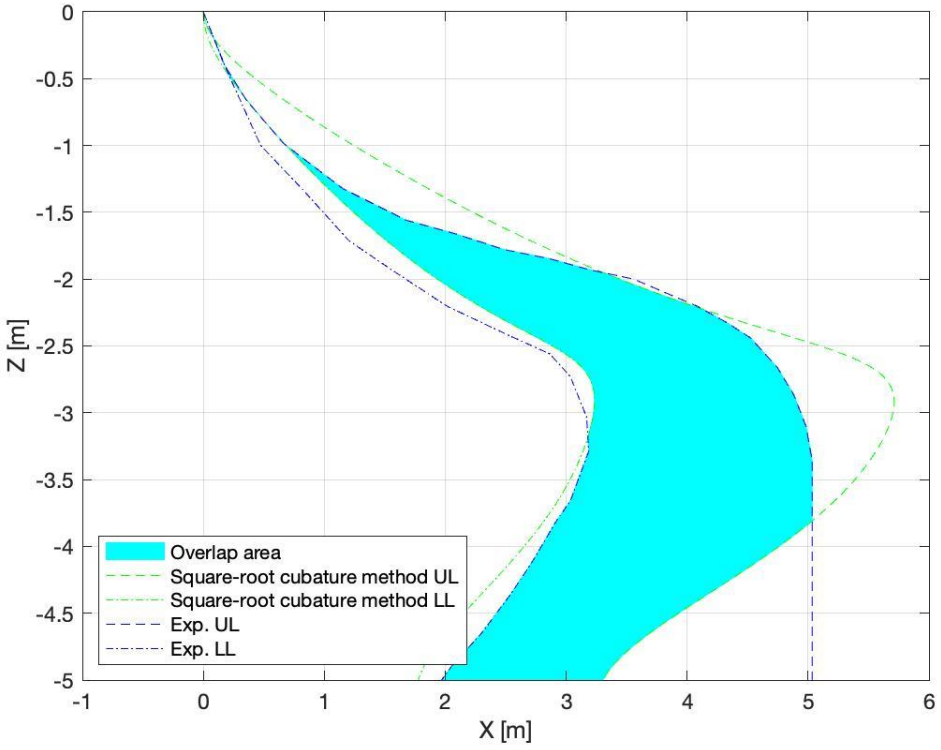
Z [m]
X [m]
Overlap area
Square-root cubature method UL
Square-root cubature method LL
Exp. UL
Exp. LL

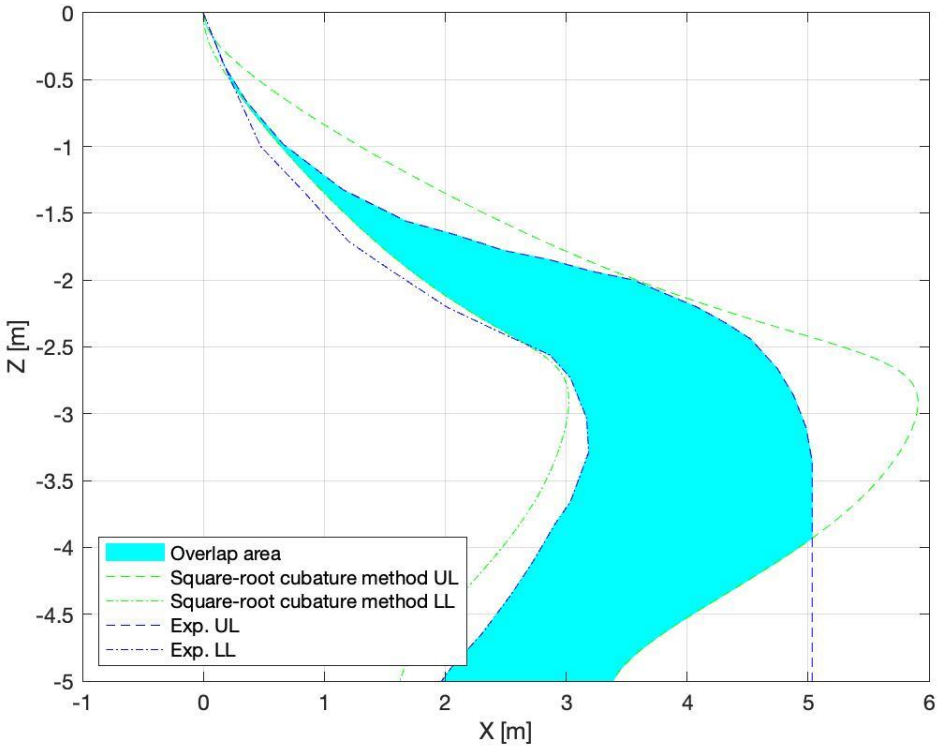
Z [m]
X [m]
Overlap area
Square-root cubature method UL
Square-root cubature method LL
Exp. UL
Exp. LL

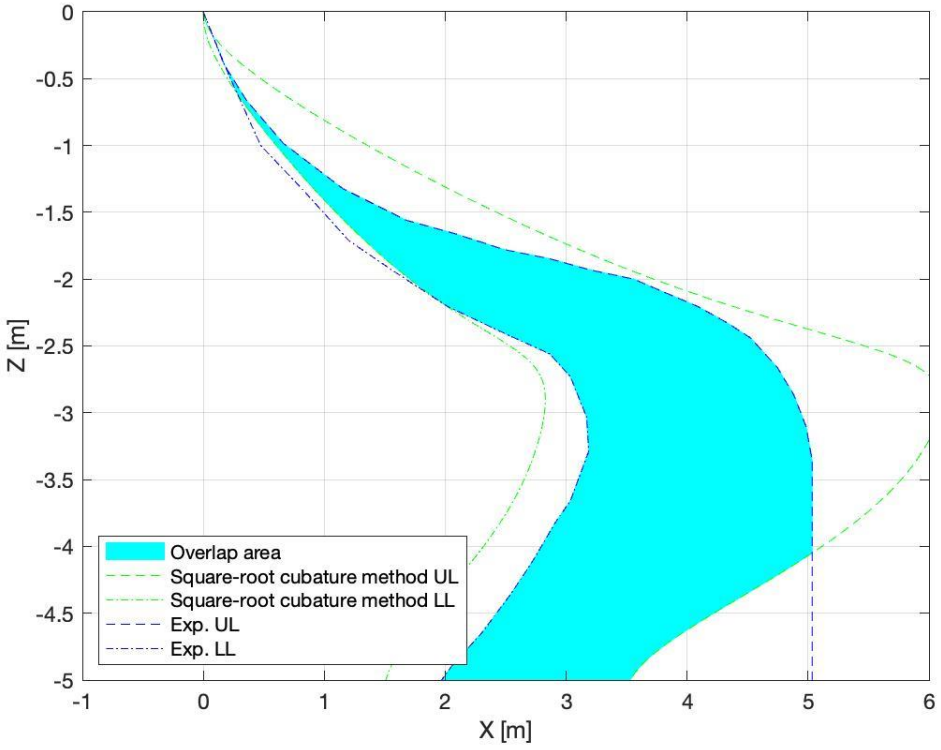
Z [m]
X [m]
Overlap area
Square-root cubature method UL
Square-root cubature method LL
Exp. UL
Exp. LL

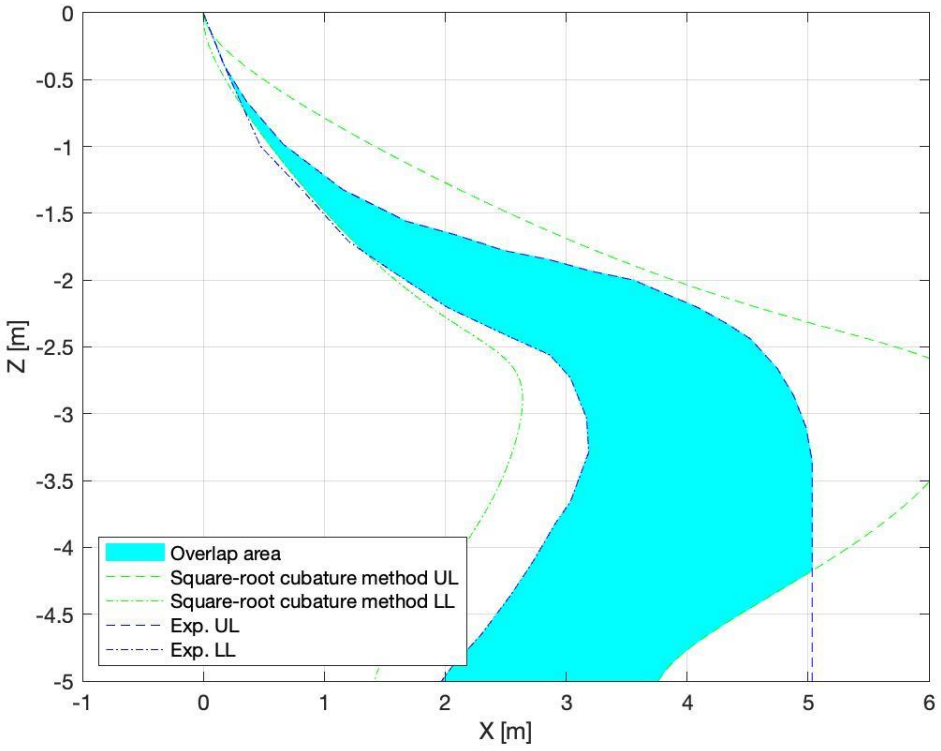

Figure A.4 Overlap area between square-root Cubature method and experimental envelope with the drop angle 45° in 3D (α =0.1-0.9)

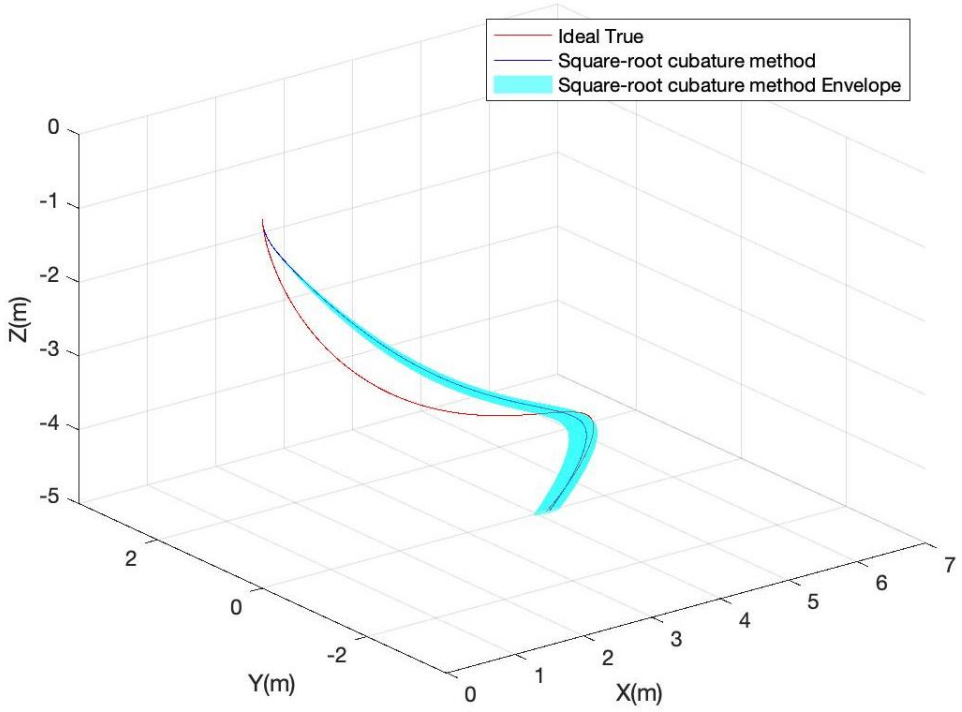

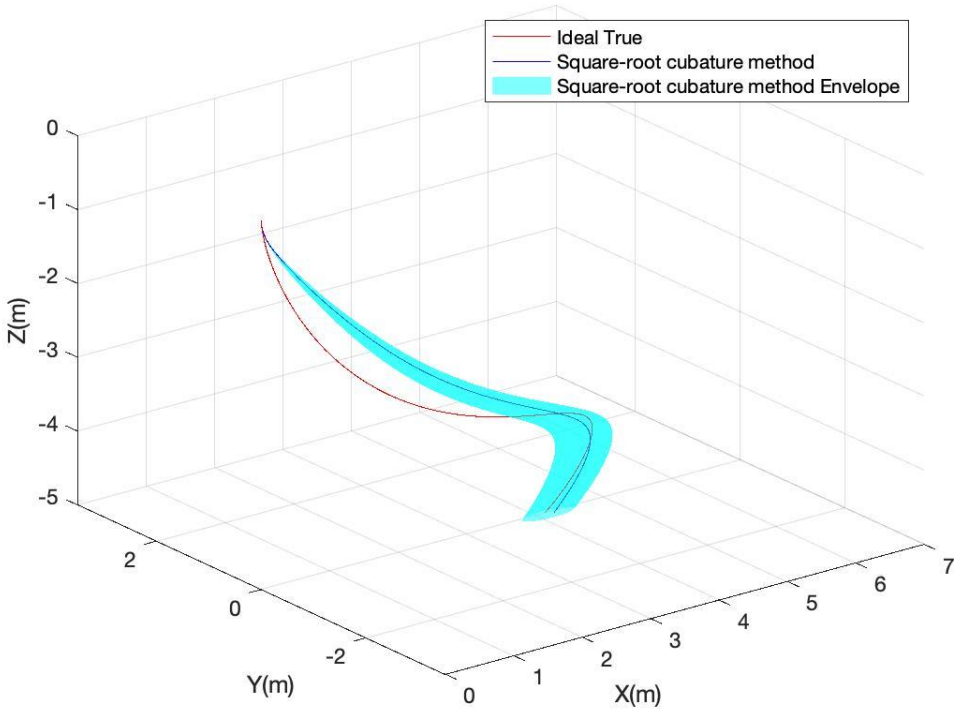
Ideal True
Square-root cubature method
Square-root cubature method Envelope
Z(m)
0
-1
-2
-3
-4
-5
Y(m)
2
0
-2
X(m)
0
1
2
3
4
5
6
7

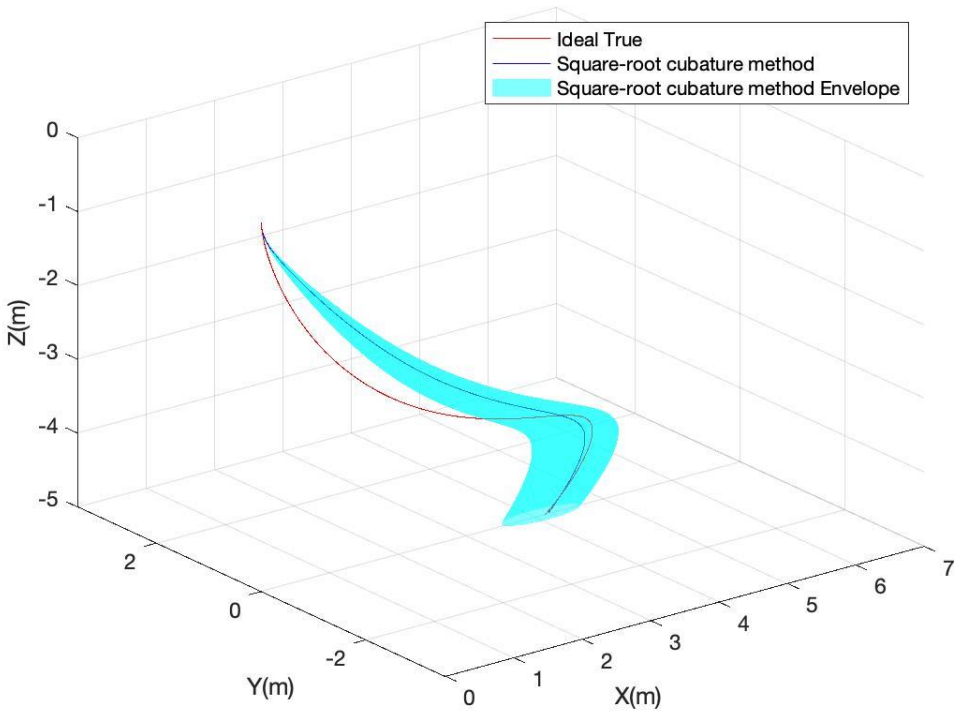
Ideal True
Square-root cubature method
Square-root cubature method Envelope
Z(m)
0
-1
-2
-3
-4
-5
Y(m)
2
0
-2
X(m)
0
1
2
3
4
5
6
7

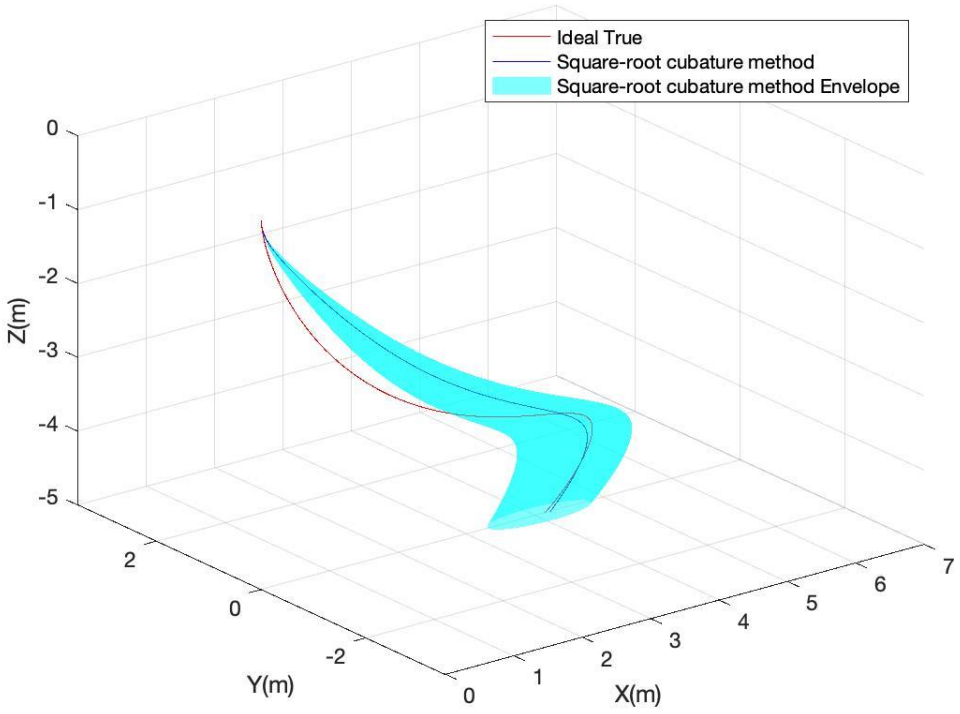
Ideal True
Square-root cubature method
Square-root cubature method Envelope
Z(m)
0
-1
-2
-3
-4
-5
Y(m)
2
0
-2
X(m)
0
1
2
3
4
5
6
7

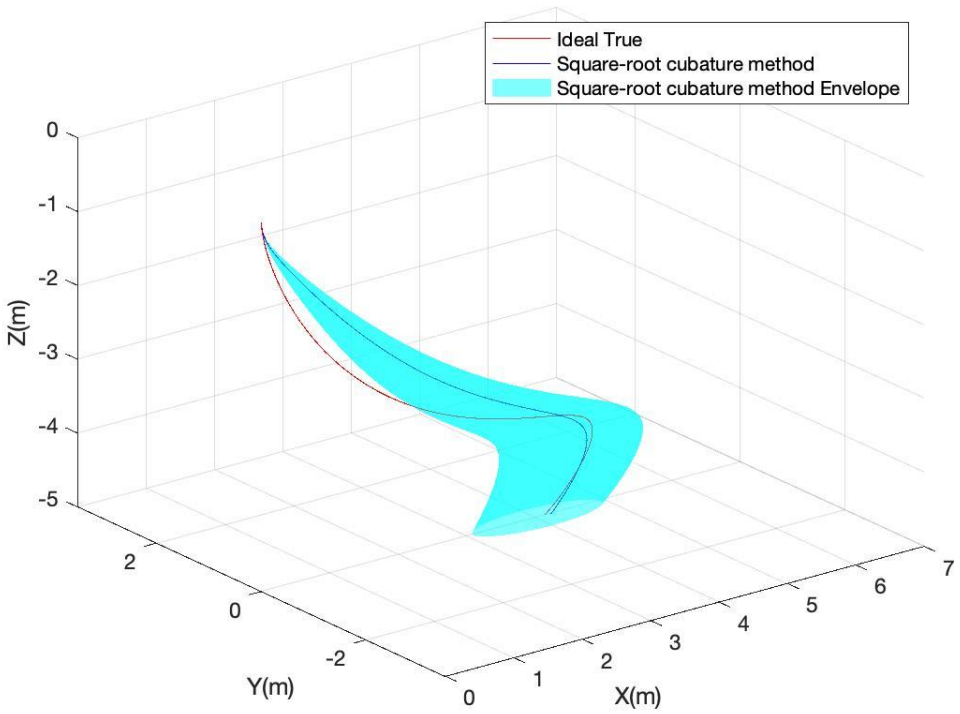
Ideal True
Square-root cubature method
Square-root cubature method Envelope
Z(m)
0
-1
-2
-3
-4
-5
Y(m)
2
0
-2
X(m)
0
1
2
3
4
5
6
7

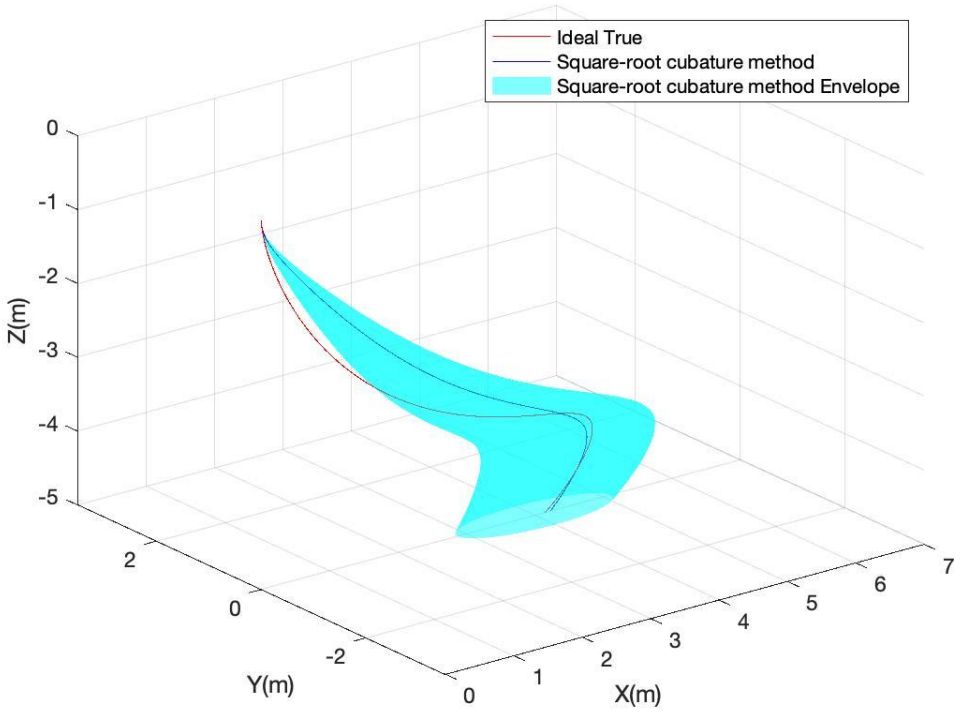
Ideal True
Square-root cubature method
Square-root cubature method Envelope
Z(m)
0
-1
-2
-3
-4
-5
Y(m)
2
0
-2
X(m)
0
1
2
3
4
5
6
7

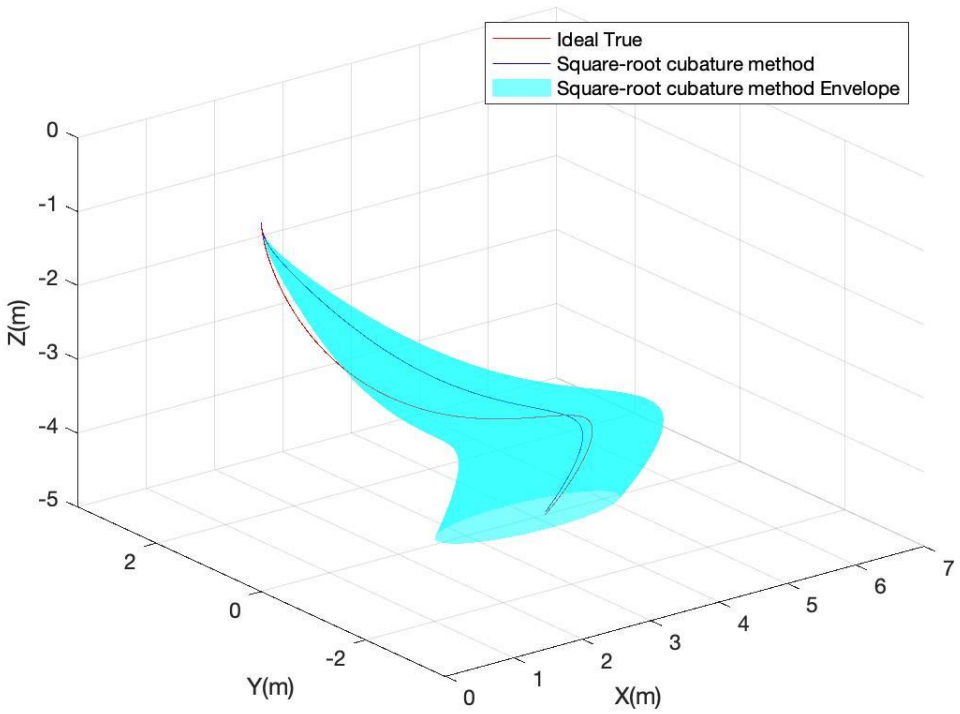
Ideal True
Square-root cubature method
Square-root cubature method Envelope
Z(m)
0
-1
-2
-3
-4
-5
Y(m)
2
0
-2
X(m)
0
1
2
3
4
5
6
7

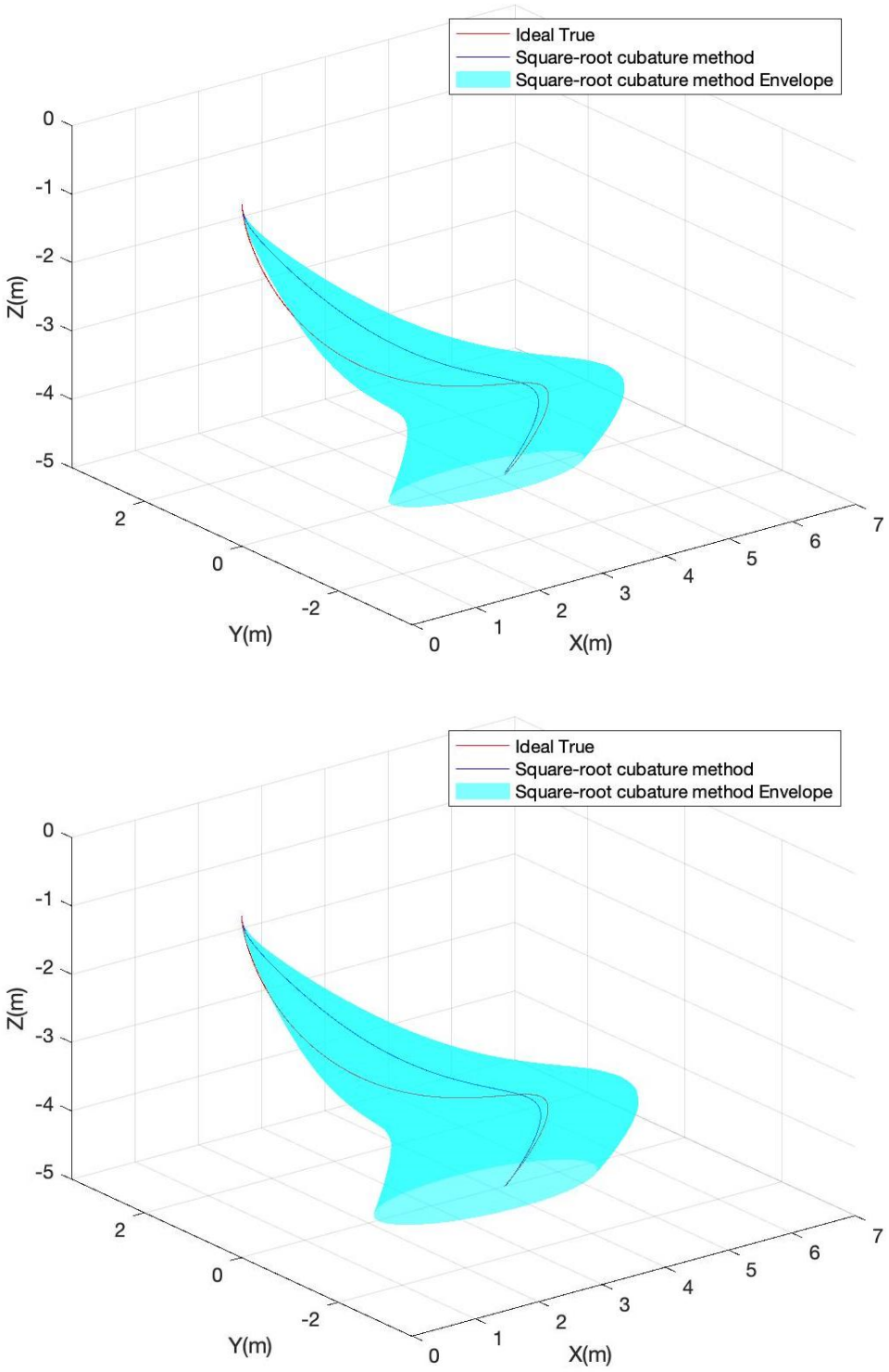

Figure A.5 Trajectory prediction at the drop angle $60°$ using square-root Cubature method in 3D (α =0.1-0.9)

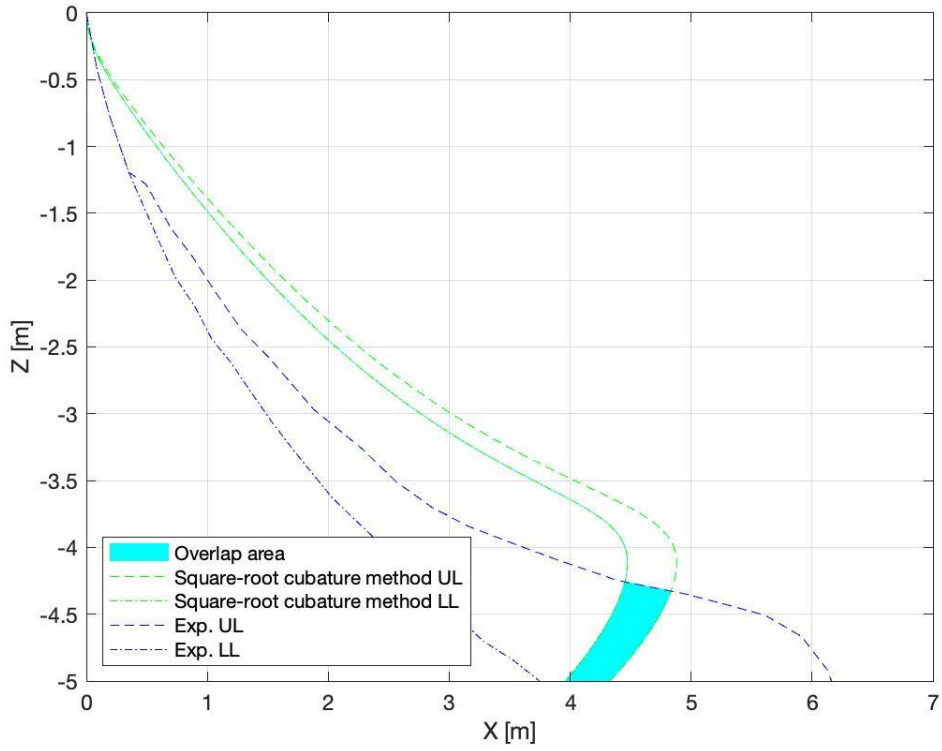
Z [m]
X [m]
Overlap area
Square-root cubature method UL
Square-root cubature method LL
Exp. UL
Exp. LL

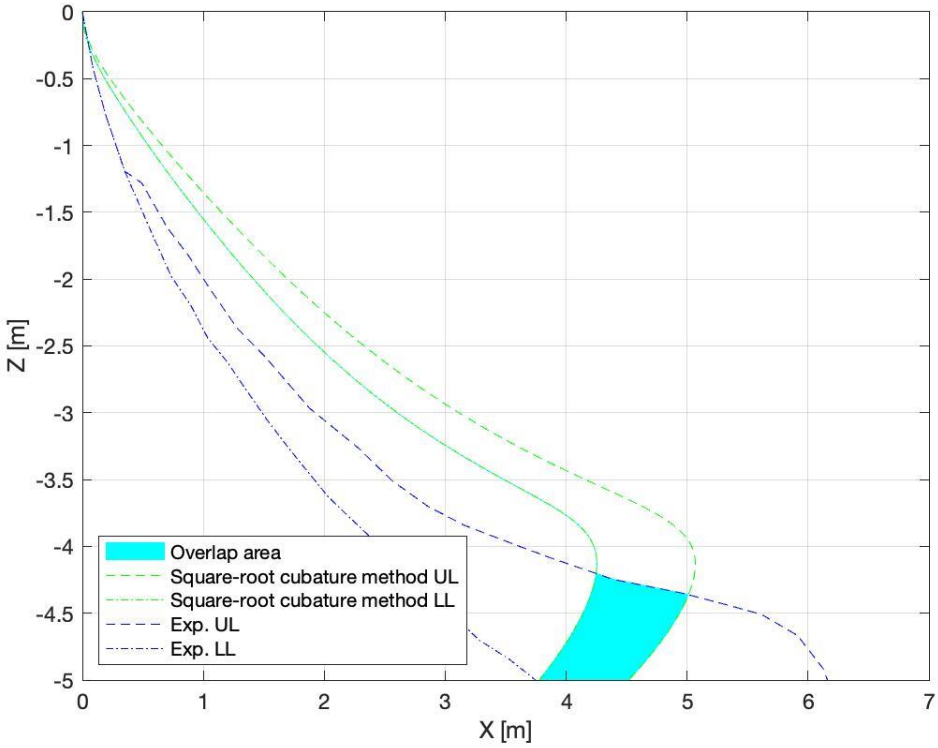
Z [m]
X [m]
Overlap area
Square-root cubature method UL
Square-root cubature method LL
Exp. UL
Exp. LL

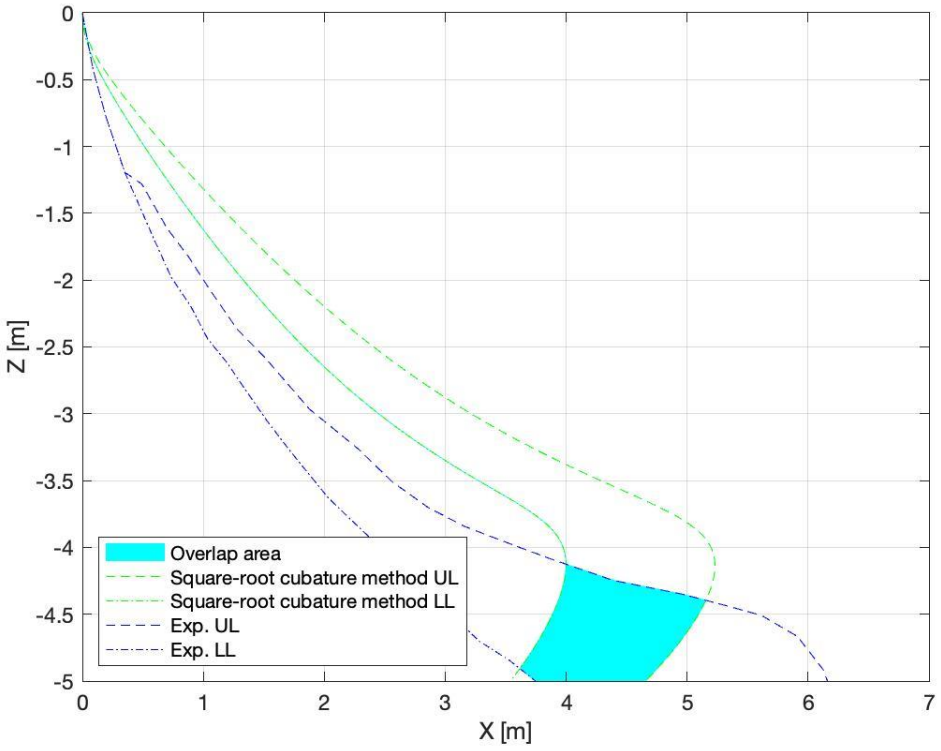
Z [m]
X [m]
Overlap area
Square-root cubature method UL
Square-root cubature method LL
Exp. UL
Exp. LL

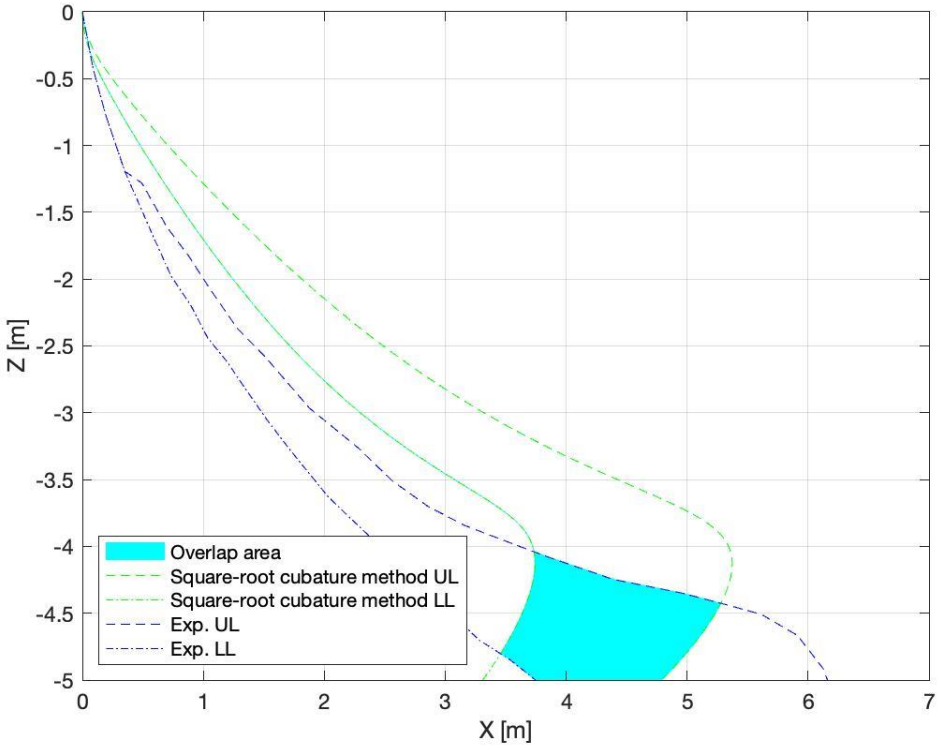
Z [m]
X [m]
Overlap area
Square-root cubature method UL
Square-root cubature method LL
Exp. UL
Exp. LL

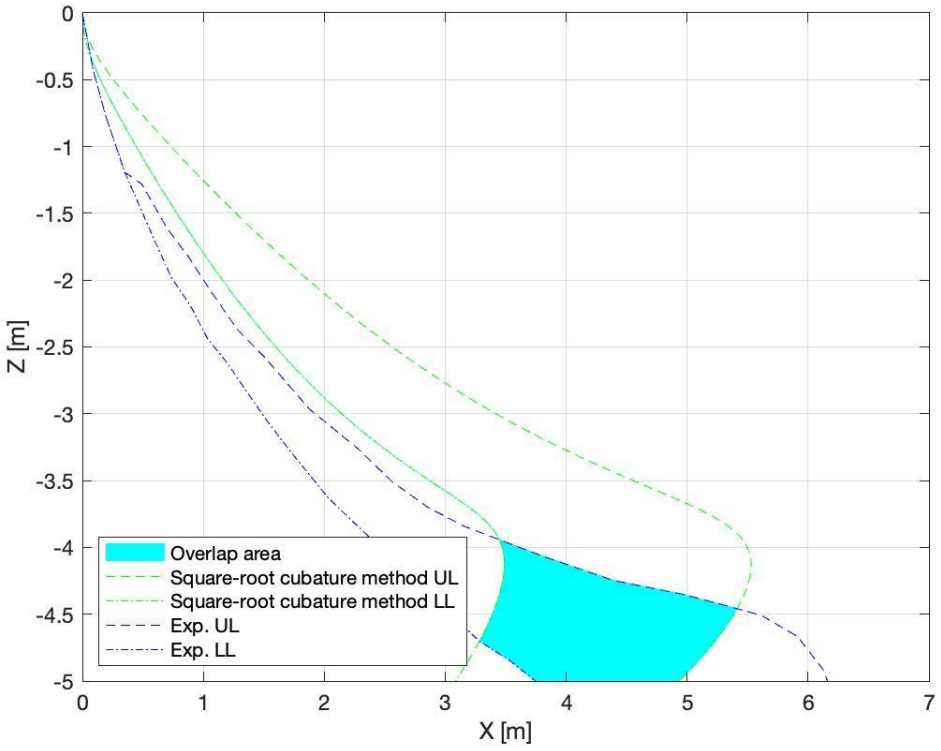
Z [m]
X [m]
Overlap area
Square-root cubature method UL
Square-root cubature method LL
Exp. UL
Exp. LL

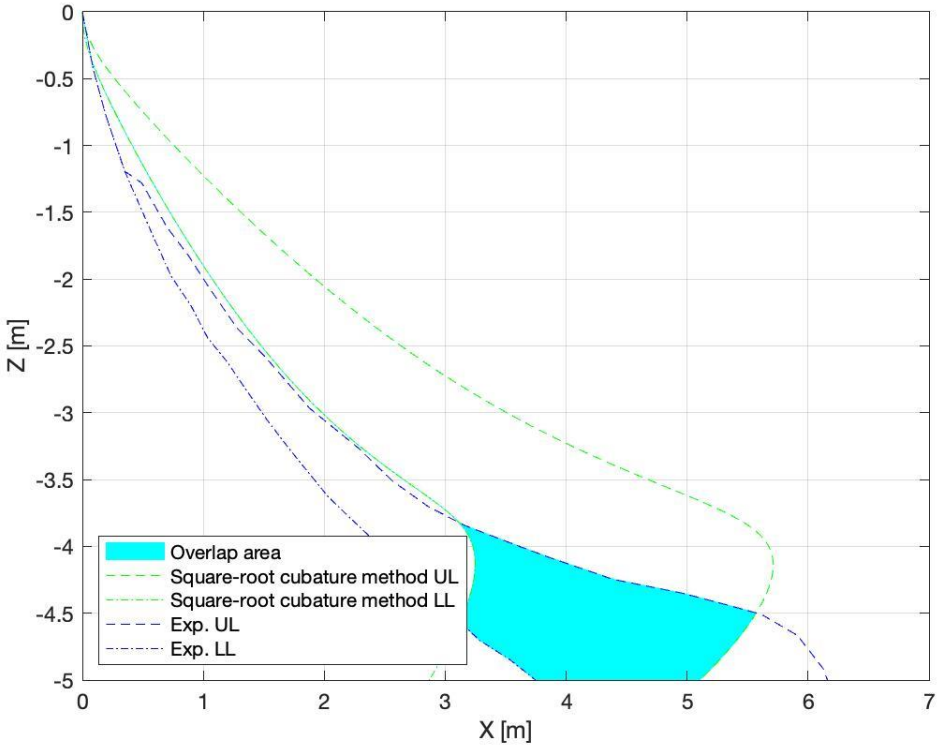
Z [m]
X [m]
Overlap area
Square-root cubature method UL
Square-root cubature method LL
Exp. UL
Exp. LL

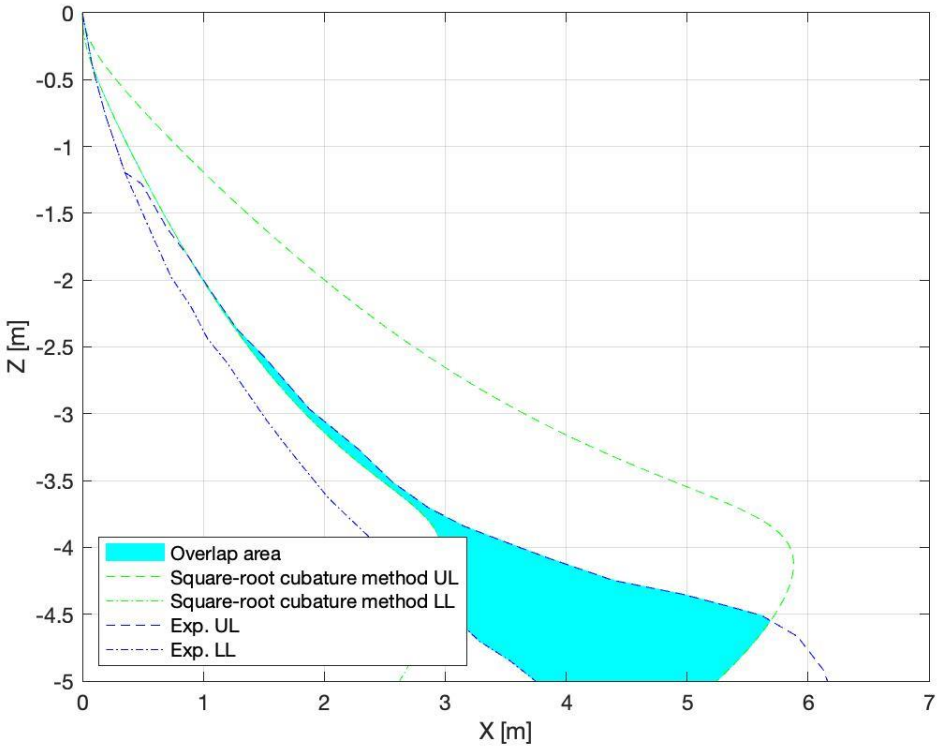
Z [m]
X [m]
Overlap area
Square-root cubature method UL
Square-root cubature method LL
Exp. UL
Exp. LL

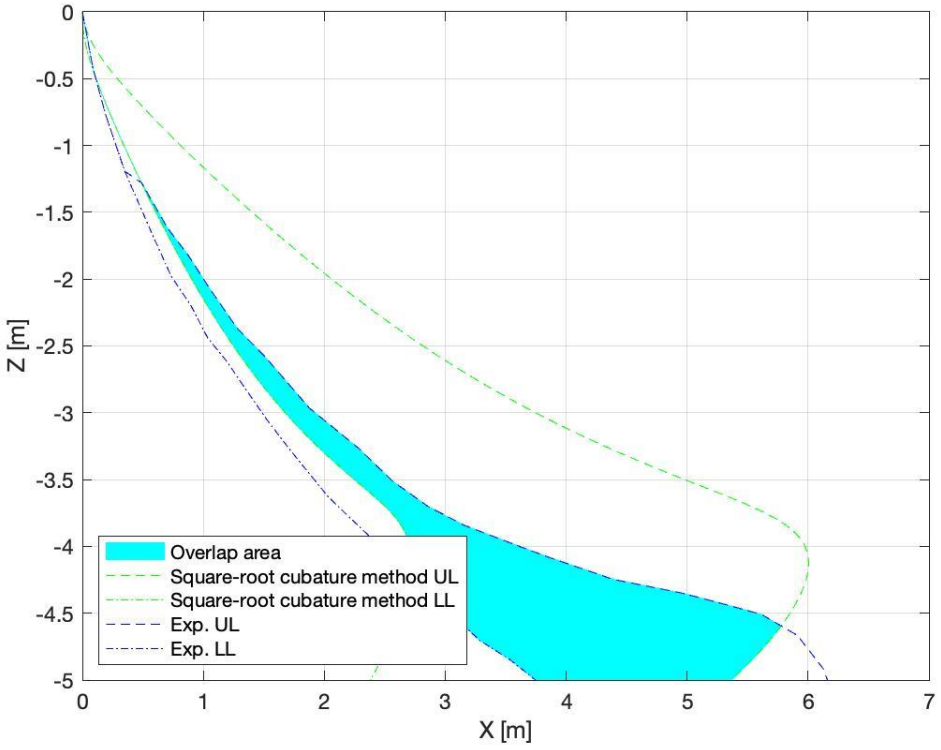
Z [m]
X [m]
Overlap area
Square-root cubature method UL
Square-root cubature method LL
Exp. UL
Exp. LL

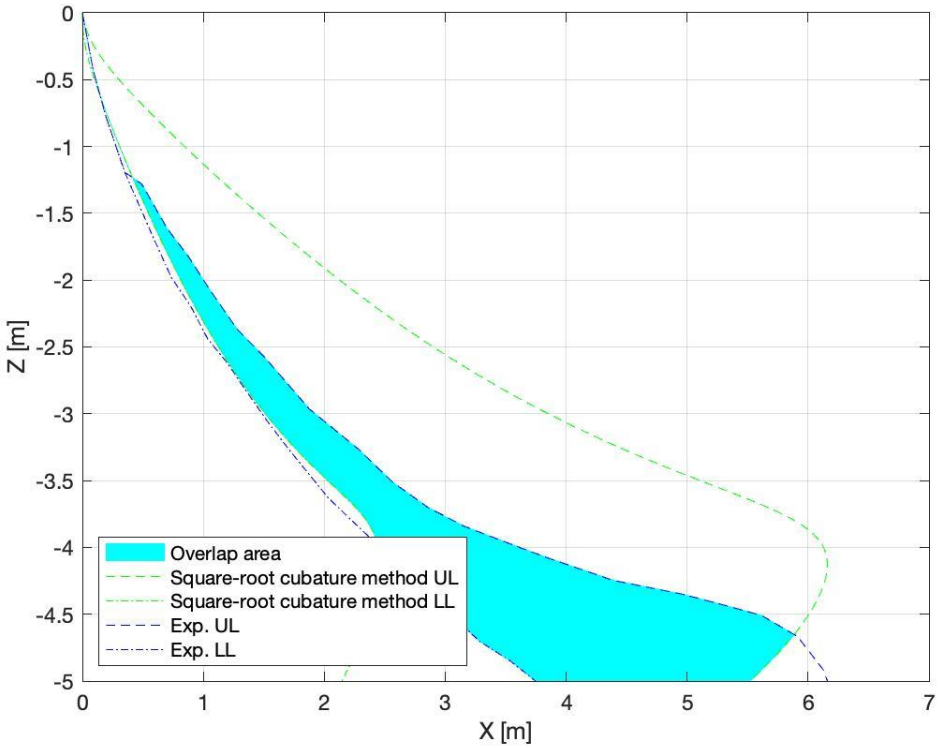

Figure A.6 Overlap area between square-root Cubature method and experimental envelope with the drop angle 60° in 3D (α =0.1-0.9)

VITA

Yi Li was born in Guangdong, China. He earned his B.S. degree in Civil Engineering from Qingdao Technological University in 2015 and his M.S. degree in Naval Architecture and Marine Engineering from University of New Orleans in 2020. Currently, he is a Ph.D. candidate at the Boysie Bollinger School of Naval Architecture and Marine Engineering, University of New Orleans.